Title
Coiled Tube Gas Heater Effectiveness Modeling, Simulation, and Experiments for Nuclear Power Conversion Cycles

Author
Greenop, Andrew

Publication Date
2018

Peer reviewed|Thesis/dissertation

Coiled Tube Gas Heater Effectiveness Modeling, Simulation, and Experiments for Nuclear Power Conversion Cycles

By

Andrew Greenop

A dissertation submitted in partial satisfaction of the

requirements for the degree of

Doctor of Philosophy

in

Engineering - Nuclear Engineering

and the Designated Emphasis

in

Energy Science and Technology

in the

Graduate Division

of the

University of California, Berkeley

Committee in charge:

Professor Per F. Peterson, Co-Chair
Professor Simo A. Mäkiharju, Co-Chair
Professor Massimiliano Fratoni
Professor Van P. Carey

Spring 2018

Coiled Tube Gas Heater Effectiveness Modeling, Simulation, and Experiments for Nuclear Power Conversion Cycles

by

Andrew Greenop

Abstract

Coiled Tube Gas Heater Effectiveness Modeling, Simulation, and Experiments for Nuclear Power Conversion Cycles

by

Andrew Greenop

Doctor of Philosophy in Nuclear Engineering

Designated Emphasis in Energy Science and Technology

University of California Berkeley

Professor Per F. Peterson, Co-Chair

Professor Simo A. Mäkiharju, Co-Chair

With the growing demand for clean, carbon free electricity around the globe due to industrialization and increasing populations, nuclear reactors will become a necessity to supplement power from intermittent renewable sources. Advanced reactor designs such as the Fluoride Salt-cooled High Temperature Reactor, or FHR, are especially desirable due to their small, modular design, their passive safety systems, and their smaller capital costs. The reactor's small size, high temperatures, and single-phase molten salt coolant meant that conventional heat exchanger designs could not be used as the primary form of heat removal. This lead to the development of the Coiled Tube Gas Heater, or CTGH, so that the reactor could be coupled with an air Brayton reheat cycle. The CTGH is a shell-and-tube heat exchanger that uses an annular tube geometry to reduce the overall volume of the heat exchanger. In the FHR design, the air flows up the center of the annular bundle and flows out radially through the coiled tubes. The molten salt coolant is distributed vertically to multiple tubes within multiple sub-bundles in the CTGH. Starting at the outer radius of the bundle, the salt tubes coil around the bundle multiple times before reaching the inner manifolds and flowing out the bottom of the heat exchanger. This creates a heat exchanger with high effectiveness due to a large heat transfer surface area density and with a design that is essentially a counterflow heat exchanger. By using seamless tubes that are in compression rather than tension, the design minimizes the points of stress concentration and the risk of tubes bursting. Due to its high effectiveness, relatively low pressure drops, compact design, structural integrity, and resistance to damage from thermal shocks, the CTGH is an optimal choice for the primary heat exchanger in the FHR design.

In order to design the CTGH specifically for the FHR, it was necessary to simulate the conditions in the FHR. Conventional modeling codes would take too long to model the complex geometry of the CTGH to be an effective design tool, so this dissertation developed an effectiveness modeling code specifically for CTGHs called Transverse Heat Exchange Effectiveness Model, or THEEM. THEEM is an unconventional finite volume method code that uses empirical heat transfer and pressure drop correlations instead of governing equations for its calculations. It was used to model the temperature and pressure distributions across the CTGH bundle and, consequently, to calculate the effectiveness, fluid outlet temperatures, and fluid pressure drops across the bundle. This program was then used to model the CTGH for the FHR.

It found that this design, compact enough to fit on a rail car, would transfer the desired heat between the salt and the air, and it would have relatively low pressure drops for the salt and air.

In order to use THEEM as a design tool, it was necessary to validate the code experimentally. Two different experiments that both used water and air as heat transfer fluids were performed for this purpose. The first experiment primarily served as a proof of concept for fabrication of a CTGH tube bundle, but due to poor construction, it did not provide useful experimental data. The second experiment was constructed specifically for comparison with the THEEM code. Its measurements provided useful data to validate THEEM for larger CTGH designs. The second experimental setup also provided opportunities for other experiments. First, airflow measurements were taken around the bundle in order to measure the airflow distribution around the bundle, which can be used to model flow distribution in CTGH bundles. Next, using the Wilson plot method, the setup was used to derive empirical Nusselt number correlations for both the tube-side and shell-side of the heat exchanger. These can be used in system modeling codes to calculate the heat transfer in the CTGH for different reactors. Finally, the setup was used to perform binary impulse measurements for the CTGH. This measured the response of the heat exchanger to an immediate loss of heating power. With further additions to the setup, these tests could be modified to simulate the CTGH's response to various reactor accidents and transients in both the FHR and other reactors.

Once THEEM had gone through initial experimental validation, it could be expanded as a design tool for other applications besides the FHR. First, a parametric study was performed to measure the effect of changing each aspect of the CTGH geometry on the outlet parameters of the bundle. These results were then used to develop an optimization tool that could design CTGHs for various applications outside of the FHR. This optimization tool used a Monte Carlo method algorithm as well as physical constraints set by the user to design the optimal CTGH for a given application. This tool was then used to design CTGHs for different applications coupling a single-phase coolant with a Brayton cycle. These examples included a CTGH coupling a sodium fast reactor with a supercritical carbon dioxide Brayton cycle, a CTGH coupling a different molten salt reactor with an air cooling system, and CTGHs used in different electrically-heated salt loops that thermally modeled nuclear reactors. This showed that the CTGH could be used in multiple nuclear applications and that THEEM would be an effective design tool for those CTGHs.

The work performed in this dissertation will be essential to deploying large scale CTGHs for the FHR and other reactors. The THEEM code and the results of the experiments in this dissertation can be used for performing a structural analysis of the heat exchanger, studying flow-induced vibration through the tube bundle, studying the effects of tube fouling over the lifetime of the heat exchanger, and performing a cost analysis on fabrication of the heat exchanger. With these future studies and the work presented in this dissertation, the CTGH design will become a more efficient and cost-effective heat exchanger for the FHR and other nuclear Brayton cycles.

Acknowledgements

It's hard to believe the time has finally come. I have one last section separating me and my doctorate. There were so many times throughout grad school that it seemed impossible to reach this point. Looking back at my tenure here at Berkeley, I can honestly say I experienced some of the best and some of the worst moments of my life. A few of them were a direct results of grad school while others were caused by outside events. Either way, I can say moving out to California for grad school shaped me into what I would like to think is a better person and prepared me for an exciting journey as I start my career. The nervous and slightly shy person who came to California 4 years with no clue what he was doing would probably not recognize the person I am today. Of course, no person is an island, so I would like to acknowledge the people who helped and influenced me along the way.

First, I would like to acknowledge and thank the professors at my undergrad alma mater, Christian Brothers University, for what they did for me before grad school. Dr. Paul Shiue, Dr. Jose Davila, Dr. James Aflaki and Dr. Eric Welch, I spent long hours working for your classes and may have complained about it a lot at the time. However, you taught me how to be a better engineer, and I appreciate all of the guidance and advice each of you gave me throughout my undergrad career about grad school and life in general after undergrad. I also want to thank Dr. Tracie Burke for always being someone I could talk to and for giving me the push I needed to get through some tough times and to apply to grad school. And though he passed away shortly after I started grad school, I am eternally grateful to Dr. Joseph Shuster whose talk about the future of energy in the US inspired me to go into nuclear engineering.

Once I arrived at Berkeley, I met a brilliant and passionate faculty who greatly influenced me throughout grad school. I want to acknowledge all of the work and effort from the faculty in the UC Berkeley Nuclear Engineering department. I especially want to thank Professor Per Peterson, who funded me throughout my time at UC Berkeley and was one of the driving motivations behind the research in this dissertation. The lessons I learned from him as an advisor and mentor will influence me throughout my life. I am sure these experiences will make me a better mentor and leader in the future. I also want to thank Professor Max Fratoni who motivated me more than he intended. As a teacher, he did an amazing job teaching me about reactor design, and he has been a great asset to our department. Since the beginning of grad school, he taught me that no matter the challenge, criticism, or negativity, you can always turn that into motivation and achievement. Also, the best way to deal with negative people like that is to prove them wrong. I want to thank Professor Peter Hosemann for his influence on me and our department. Even though he was tough, I found him to be fair and to want to teach you how to be a better researcher and student. I also want to thank Professor Simo Mäkiharju for being my co-chair. I wish I could have worked more with him, but I appreciate him helping me and taking on the extra responsibility of being my co-chair. Finally, I want to thank Professor Van Carey for his wonderful class on two-phase heat transfer and for agreeing to be on my committee.

I also want to acknowledge the staff members at UC Berkeley that have helped me throughout my research and time in grad school. The Etcheverry Machine Shop staff helped me countless times on building my experiments in this lab. Thank you, Scott McCormick, Brien Angelo, Jacob Gallego, Jeff Higginbotham, Dennis Lee, and Jesse Lopez. I could not have

finished my work without your help. I also wanted to thank both Jeff Bickel and AJ Gubser for being patient with all of my questions and helping me in 1140. Dr. Alan Bolind especially was helpful around 1140. I really appreciate all of the extra time he took helping me with some of the details of building an experiment in 1140. I also am glad I was able to serve as a GSI under him. Thanks, Alan, for being such a great teacher and helping me improve my own understanding of Thermodynamics. Finally, I want to acknowledge Noriko Katagiri. She helped me navigate through ERSO and always went above and beyond when it came to answering questions about funding, purchasing parts for the experiment, and processing reimbursements.

I also want to thank all of the other students, both grad and undergrad. I appreciate all of the friendship and support from the other grad students in the department, but I want to especially thank everyone in the TH group. Thank you to the older grad students for helping me when I first started: Nicolas Zweibaum and Lakshana Huddar. I want to especially thank Charalampos 'Harry' Andreades who was a great source of advice and guidance as both an older grad student and then postdoc. Also, I want to thank the other TH grad students who made my final years in the TH lab a great experience: Xin Wang, James Kendrick, Shane Gallagher, Ishak Johnson, Chris Poresky, Dane de Wet, Limin Liu, Brian He, and April Novak. I also want to thank Emily Frame for being an awesome roommate for a large part of my time in Berkeley. Next, I wanted to thank the undergrads who helped along the way. Connie Lee did excellent work on the tube-to-tube sheet joints and it was a pleasure to work with her. I am also eternally grateful to Jae Keun Choi and Bryant Phan who helped me design, fabricate, and run experiments on CASET. If it had not been for them, I would not have been able to finish my work.

The final group of people I wanted to thank are my family and friends from Memphis. Thank you to Faith Pollan, Will Zachary, Luke Eck, Nathan Short, Michael Hankins, and many others for being there for me when I was stressed and for remaining great friends even after I left Memphis. Thank you to my cousins, Carl, Zoe, Aowyn, Atticus, and Abe Soane for opening your home to me while I lived in the Bay Area. You really made me feel like a part of the family while I lived out here. I also wanted to thank my grandparents, Pat and Nigel Sadd, for supporting me however they could from the other side of the country. I also want to thank my mother, Susan Greenop, for giving me the love and support both before I moved to California and while I was out here. I know it was a struggle for you, especially in this final year. I am so glad you were able to see me finish this program and earn a PhD. Finally, I want to thank Sarah Warren for being a loving girlfriend, for listening to me complain and stress about everything, and for just being there for me in this final year of my program. You made it possible for me to finish strong and confidently.

Table of Contents

List of Figures

List of Tables

Acronyms and Abbreviations

AMTD - Arithmetic Mean Temperature Difference
ASME - American Society of Mechanical Engineer
BPVC - Boiler and Pressure Vessel Code
CASET - Coiled-tube Air-heater Separate Effects Test
CIET - Compact Integrals Effects Test
CTAH – Coiled Tube Air Heater
CTGH – Coiled Tube Gas Heater
FHR – Fluoride Salt-cooled High Temperature Reactor
GIF - Generation IV International Forum
HP CTAH – High-Pressure CTAH
HRSG - Heat Recovery Steam Generator
IAEA - International Atomic Energy Agency
LMTD – Log Mean Temperature Difference
LOFC – Loss of Forced Circulation
LOOP - Loss of Offsite Power
LP CTAH – Low-Pressure CTAH
LWR – Light Water Reactor
Mk1 PB-FHR - Mark1 Pebble Bed Fluoride Salt-cooled High Temperature Reactor
MSR – Molten Salt Reactor
MSRE - Molten-Salt Reactor Experiment
ORNL - Oak Ridge National Lab
PCHE - Printed Circuit Heat Exchanger
RACC - Reheat-Air Brayton Combined Cycle
S-CO2 – Supercritical Carbon Dioxide
SFR – Sodium Fast Reactor
SINAP - Shanghai Institute of Applied Physics
SMR – Small Modular Reactor
STHE - Shell-and-Tube Heat Exchanger
THEEM – Transverse Heat Exchange Effectiveness Model
TMSR - Thorium-based Molten Salt Reactor
TRISO - Tristructural-Isotropic
VFD – Variable Frequency Drive
WHO – World Health Organization

Chapter 1.
Introduction

Over the past few decades, as technology and the quality of life have improved in various countries, global energy demand has increased. From 1973 to 2015, the world total energy consumption more than doubled from approximately 54,000 TWh in 1973 to approximately 109,000 TWh in 2015, or an average annual increase of 2.43% [1]. The International Energy Agency predicts that the future rate of energy consumption will rise more slowly than in the past. However, it is still expected that, due to rising population and the industrialization of various countries, the annual world total energy consumption will increase by approximately 30% between 2017 and 2040, or 1.30% annually. This total increase in demand is equivalent to the current energy demand of China and India combined [2]. In order to meet this growing demand in the past, many countries have relied on increasing energy production using fossil fuels, especially coal and more recently natural gas. Unfortunately, increased use of fossil fuels has led to higher levels of air pollution and greenhouse gases. Increased air pollution has led to higher rates of illness and premature death; the World Health Organization (WHO) estimates 7 million people die annually due to air pollution [3]. Increased greenhouse gases have led to global warming, which can cause catastrophic environmental damage in the future. One of the more popular solutions is to replace fossil fuel power plants with renewable energy sources, such as wind or solar power. These sources produce clean and carbon-free electricity, but unlike fossil fuels plants, they are intermittent energy sources. These sources are necessary to providing clean electricity as energy demand grows, but, due to limited energy storage technology, they need to be used with clean carbon-free baseload energy sources as well. Hydro and geothermal power are carbon-free energy sources that can be used as baseload sources, but they are limited geographically. However, nuclear power plants can be built anywhere and provide baseload power without emitting carbon or air pollution. In order to meet the growing demand for clean, carbon-free electricity in the future, nuclear energy needs to be a major component of global energy production.

The majority of currently operating commercial reactors are light water reactors (LWRs). Since they use water as a coolant and moderator, they operate at higher pressures, usually between 75 -150 bar depending on the design, to keep the water as a liquid. Even though these designs incorporate multiple safety systems so that accidents are rare, many still required operator intervention to prevent most accidents. Many of these LWR designs are also relatively large. As of 2018, the United States has 99 LWRs with a total generating capacity of 99.062 GWe, or an average reactor capacity of just over 1 GWe [4]. These large reactors are expensive, major construction projects that often are only practical near large population centers. In order to become more feasible in areas with lower demand for electricity and to reduce capital costs, many newer reactors are designed with much smaller generating capacities. In 2001, the world's leading nuclear nations came together to form the Generation IV International Forum (GIF) to develop the next generation of nuclear technology. The focus of the GIF was to create the framework to develop more advanced reactors to supplant current LWR technology. One goal of the forum was to look for designs that were inherently safe, meaning that the safety systems

would engage without operator intervention. Since many of the designs did not use water as a coolant, these reactors could operate at pressures closer to atmospheric, often providing a safer design. Also, in order to meet the electricity demands for smaller populations and to reduce costs, many of these reactors were designed as small modular reactors (SMRs). SMRs operate at much lower generating capacities and are built in a manufacturing plant instead of being constructed entirely on-site. This means that the economies of scale may reduce the overall costs of building these advanced reactors. The GIF chose the following six technologies to be deployed as Generation IV reactors: Gas-cooled Fast Reactor, Lead-cooled Fast Reactor, Molten Salt Reactor (MSR), Sodium-cooled Fast Reactor, Supercritical Water-cooled Reactor, and Very High-temperature Gas Reactor [5]. This dissertation will specifically focus on the components for a type of MSR called the Fluoride Salt-cooled High Temperature Reactor, or FHR.

1.1 Background on FHR

The FHR is a 236-MWt/100-MWe SMR design that uses molten salt as its coolant. It is based on the original Molten-Salt Reactor Experiment (MSRE) perform at Oak Ridge National Lab (ORNL) that operated from 1965 to 1969 [6], [7]. Like the MSRE, the FHR uses LiF-BeF_2, or flibe salt, as a coolant due to its favorable neutronic properties. Due to the high boiling temperature of molten salts like flibe (~1400°C), MSRs can operate near atmospheric pressure while still keeping the coolant liquid. In the FHR, the coolant temperature is normally between 600°C and 700°C, so it remains single-phase through the reactor and maintains a large thermal safety margin for coolant boiling. One of the major differences between the FHR and other MSRs, like the MSRE, is that the FHR uses solid fuel instead of liquid fuel mixed with the coolant salt. In particular, the Mark1 Pebble Bed FHR, or Mk1 PB-FHR, has an annular pebble bed core containing 3.0 cm diameter fuel pebbles. These pebbles are made of graphite with an annular fuel zone of small coated fuel particles called tristructural-isotropic (TRISO) particles embedded in the graphite. A diagram of the fuel pebble and the TRISO particles are shown in Figure 1-1. Two advantages to using TRISO particles embedded in graphite are that they can be used at much higher temperatures than are expected in the FHR before sustaining damage and that they have a high retention of fission products due to the multiple coatings around the fuel particle [8], [9].

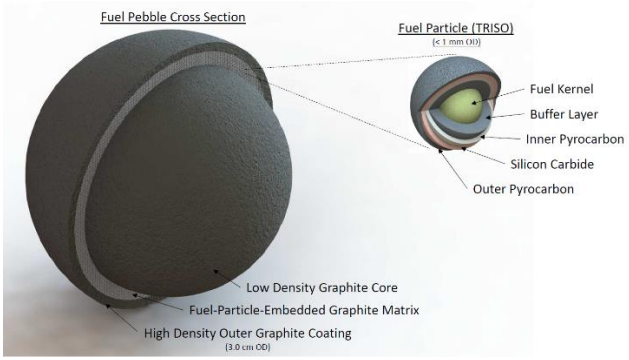

Figure 1-1. Diagram of Fuel Pebble and TRISO Particle [9]

Since the TRISO particles and graphite pebbles have a high fission product retention rate, there is little contamination in the flibe during normal operations. Any fission products that are released from the fuel will either form stable fluorides, like CsF, and remain in the salt, will precipitate on strategically placed metal surfaces where they are immobilized, or, in the case of gaseous fission products, will be released to the FHR cover-gas system and remain within the reactor. Since many other MSR designs need to prevent the release of fission products from the fuel-salt to the environment, their primary loop is usually cooled by a secondary and, sometimes, a tertiary salt loop. These loops act as fission product barriers so that the Rankine or Brayton cycle that is coupled with the reactor is not contaminated with fission products. However, adding extra loops can reduce the overall efficiency of the system. Due to its fuel design, the FHR does not require a secondary loop; the primary loop can be coupled directly with a Brayton or Rankine cycle.

Early prototypes of the FHR designs considered coupling the reactor with a steam Rankine cycle or a supercritical CO_2 Brayton cycle. However, the Mk1 FHR design called for air as the power conversion fluid. Even though the reheat-air Brayton combined cycle (RACC) has a lower base-load efficiency than both the steam Rankine cycle and the supercritical CO_2 Brayton cycle, it has other advantages. Gas turbines are generally much smaller than steam turbines, and the technology for open-air turbines is more readily available than supercritical CO_2 turbines. The RACC also has the capacity to generate large amounts of peaking power using natural gas cofiring. In the RACC, filtered air at approximately 15°C and atmospheric pressure is compressed to a ratio of 18.5 so that the air leaving the compressor is at 418.6°C and 18.76 bar. The air passes through a salt-to-air heater where it is heated to 670.0°C. The air is then expanded in a turbine to approximately the same temperature as the compressor outlet temperature with a lower pressure of 4.99 bar. The air is then reheated back to 670.0°C in a second salt-to-air heater. At this point, the air is above the auto-ignition temperature of natural gas. If there is a demand for peaking power, natural gas can be injected at this point to raise the air temperature. The air is then expanded in a second turbine to nearly atmospheric pressure before it enters the heat recovery steam generator (HRSG). The HRSG then further cools the air by using the heat to generate steam before venting the cooled air back into the environment [10], [11]. A diagram of the RACC is shown in Figure 1-2, and a diagram of the RACC coupled with the Mk1 PB-FHR is shown in Figure 1-3.

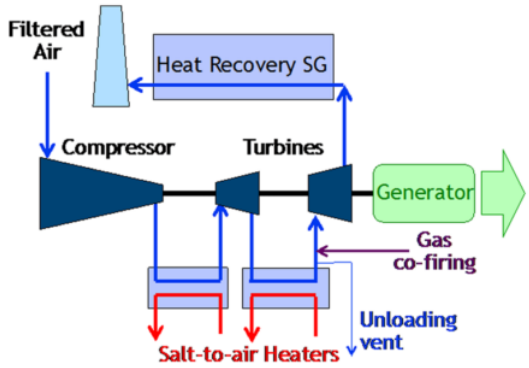

Figure 1-2. Schematic of RACC Power Conversion System [10], [11]

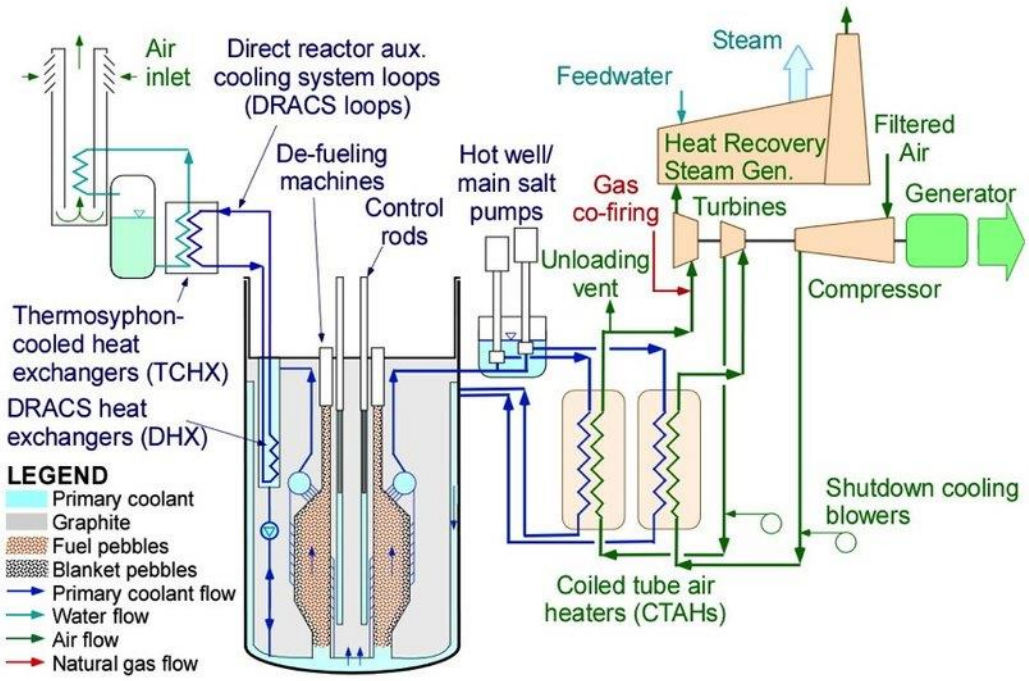

Figure 1-3. Diagram of Mk1 PB-FHR Coupled with RACC Power Conversion System[1]

The Mk1 PB-FHR with the RACC can efficiently produce both base-load and peak power to the electric grid. However, these two systems need to be coupled together by a compact heat exchanger that can efficiently transfer heat from the salt to the air while minimizing air pressure loss and, subsequently, air circulation power loss. The next section examines potential heater designs that could couple the FHR and the RACC and their various advantages and disadvantages.

1.2 Candidate Heat Exchanger Designs for the FHR

One of the core design philosophies behind the Mk1 PB-FHR design is that it is an SMR. The International Atomic Energy Agency (IAEA) defines an SMR as an advanced reactor that generates 300 MWe or less per module, has advanced engineered features, are deployable either as a single or multi-module plant, and are manufactured in a factory and shipped to a site where it is fully constructed [12]. Since each component will be built off-site at a factory, they must be small enough to be shipped to the site. For the FHR, each component, including the primary heat exchanger, must be rail transportable, which limits the maximum width of components to 3.5 meters for standard shipping rates or 4 meters for oversized loads shipping rates. So, the primary heat exchanger needs to have a compact design. Also, given that the FHR/RACC design requires that each heat exchanger transfers heat at a rate of 116 MW, the design requires a high effectiveness. Kays and London [13] suggest that compactness itself generally leads to high

[1] This diagram was created after the coiled tube air heater (CTAH) design was selected as the primary heat exchanger for the Mk1 PB-FHR.

performance and effectiveness. A compact heat exchanger has small flow passages which tend to give a high heat transfer coefficient. Conversely, these small flow passages often lead to high friction pressure loss for one or both of the fluids in the heat exchanger, so minimizing friction loss should be a priority in the design. In order to reduce friction loss, especially for low-density fluids, such as gases, heat exchangers are designed to have low mass velocities. Since this results in lower heat transfer rate per unit of surface area, the designs require a large amount of surface area to offset the low mass velocities. Therefore, having a compact heat exchanger means that the design has an overall small volume with a large heat transfer surface area, especially for the gas. Shah and Sekulic [14] specifically defines a gas-to-liquid heat exchanger as compact if the heat transfer surface density is greater than 700 m^2/m^3. Minimizing the air pressure drop is significant in order to minimize the circulation power loss and increase the efficiency of the entire system. It is also important to minimize the salt pressure drop in order to not oversize the pump. So, the salt-side can have a larger pressure drop than the air-side of the heater, but it cannot be greater than 3-4 bar, which allows for a reasonably sized salt pump. Then, the heat exchanger should be able to handle the high temperature environment and the high-pressure difference between the air and the flibe salt. Since the FHR reactor is designed to operate for at least 60 years, the heat exchanger design ideally should be able to operate safely in these conditions as well as handle any transients over the lifetime of the reactor. With these criteria in mind, this section examines the advantages and disadvantages of different heat exchanger designs that could couple the FHR primary flibe salt loop and the RACC.

1.2.1 U-Tube Shell-and-Tube Heat Exchanger

The first candidate for the FHR primary heat exchanger is the U-Tube Shell-and-Tube Heat Exchanger (STHE). The U-Tube STHE is one of the most common heat exchangers used in high-pressure industrial process heat transfer applications and is used extensively in nuclear reactor design. For example, many LWR designs utilize the U-tube design to generate steam for their steam Rankine cycles. It has also been used for heat transfer between molten salts. For the MSRE, the primary heat exchanger between the fuel salt and the coolant salt was a U-tube STHE [6], as shown in Figure 1-4.

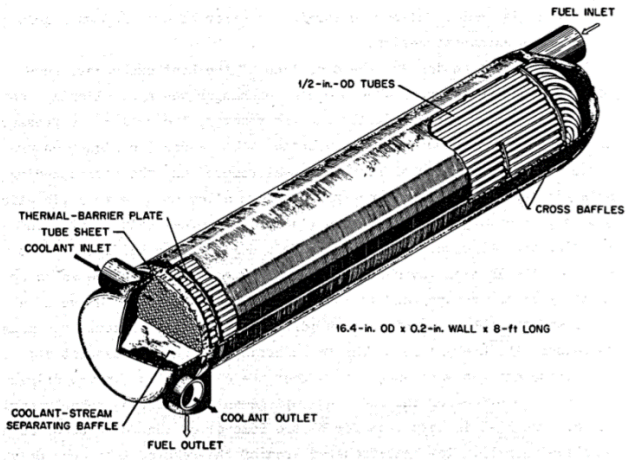

Figure 1-4. MSRE U-Tube Shell-and-Tube Heat Exchanger [6]

The U-tube STHE design consists of a bundle of tubes within a cylindrical shell with the ends of each tube connected to plenums via tube sheets. The flibe salt enters the tubes through the inlet plenum and exits the heat exchanger through the outlet plenum. In order to reduce the size of the heat exchanger, the tubes are bent in the shape of a U. For the shell-side, the air enters the shell where the tube bundle bends and flows over the tube, transferring heat via conduction through the tube walls. Baffle plates attached to the tubes are strategically placed in the shell to both maintain tube spacing throughout the bundle and to direct the air in order to maximize heat transfer. Ariu [15] looked at using the STHE as a molten salt heat exchanger and lists both the advantages and disadvantages of this design. The primary advantages of the U-tube STHE include:

- Heat exchanger fabricators have experience manufacturing them.
- They can easily operate at large pressure differences between the fluids.
- It is relatively easy to enhance heat transfer properties by changing the tube bundle geometry.

The primary disadvantages of the U-tube STHE include:

- The design has a low heat transfer surface area density (~100-300 m^2/m^3) compared to compact heat exchanger designs (>700 m^2/m^3) [14].
- The design generally has low effectiveness within the given volume constraints.

Even though this design can easily operate at the high temperature and high-pressure environment needed for the RACC, the low heat transfer surface area density means that the heat exchanger needs a larger overall volume in order to obtain the desired heat transfer. This is not a problem in many LWR designs since the heat exchangers are fabricated on-site; however, for an SMR, it appears likely that this heat exchanger would be too large and not rail transportable. For this reason, the U-tube STHE design does not meet the criteria for the Mk1 PB-FHR and RACC heat exchanger.

1.2.2 Printed Circuit Heat Exchanger

A relatively new type of compact heat exchanger design for high temperature and high-pressure applications is the Printed Circuit Heat Exchanger (PCHE). The PCHE is a counterflow plate-fin heat exchanger that consists of alternating plates and finned chambers to transfer heat between the two fluids developed by the company Heatric. This heat exchanger design has been used for many years in the upstream hydrocarbon processing, petrochemical, and refining industries. In the FHR, the flibe salt would flow through the chambers of one plate and the air would flow through the chambers in the plates surrounding that plate in the opposite direction, creating alternating layers of flibe and air. PCHEs are different from other plate-fin heat exchangers in that they use a diffusion bonding process to join the layers together. By using diffusion bonding, there is no braze or filler material at the joints; the entire heat exchanger has the strength of the parent material, forming a stronger and more robust design [16]. A diagram of a PCHE cross-section example is shown in Figure 1-5.

The PCHE initially seems like an excellent design choice for use in the FHR. The plate design means that the design has a high heat transfer surface area density (~650 to 1300 m^2/m^3) and, consequently, a high effectiveness [14]. This means that the PCHE is compact enough to be

rail transportable. Due to the robust design, the PCHE can operate at the high temperatures and high-pressure differentials expected in the FHR. Finally, the frictional pressure drops are relatively small across the heat exchanger. However, Urquiza [17] has found some mechanical issues with the PCHE at conditions similar to what is expected in the FHR. Thicker sections of the heat exchanger that are not in contact with either fluid can only transfer heat via conduction, leading to higher thermal inertia in these sections of the PCHE. The difference in thermal inertia can lead to large temperature gradients across the heat exchanger and, consequently, high stress concentrations in these sections. Depending on the PCHE material, these stresses can rise above the yield stress, which can shorten the lifetime of the heat exchanger or lead to immediate failure. In a reactor setting, transients such as pump or turbine trips, reactor start-ups, and reactor shutdowns will occur regularly, so the heat exchanger needs to be able to operate under these conditions. One solution is to fabricate the heat exchanger out of a material with a higher yield stress. There has been research exploring the possibility of fabricating the heat exchanger out of a composite ceramic, such as carbon and silicon carbide composite materials [18]. This material would offer creep resistance, but it still appears to be vulnerable to thermo-mechanical transients. Further research could show that this material or another material could be designed to handle the expected transients for the FHR, but for now, this design does not seem like a viable option. Unfortunately, since the PCHE design currently cannot handle the expected thermal shocks expected over the lifetime of the FHR, it was not selected as the primary heat exchanger for Mk1 PB-FHR and RACC.

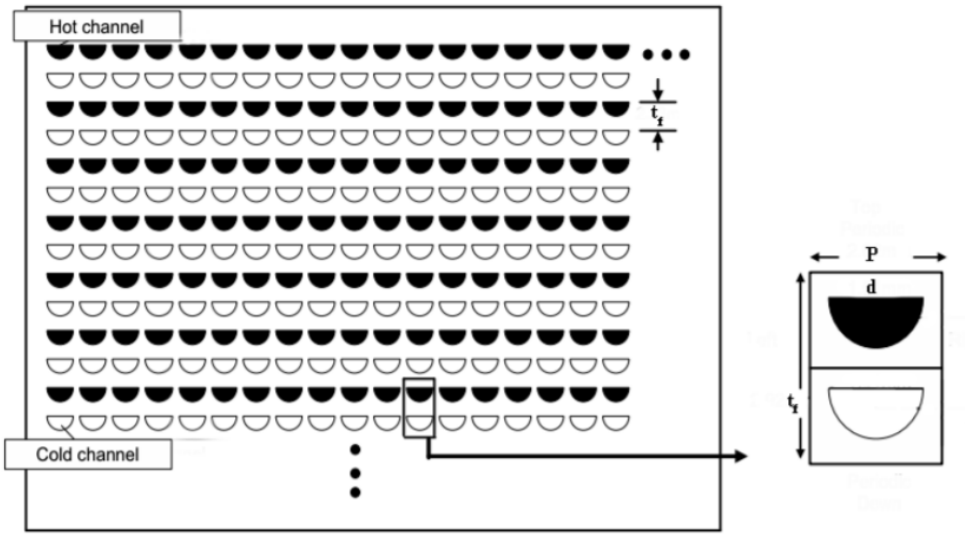

Figure 1-5. Diagram of Printed Circuit Heat Exchanger Cross-section [15]

1.2.3 Coiled Tube Heat Exchanger

Another relatively new compact heat exchanger design that was considered was the coiled tube heat exchanger design[2]. This design was first proposed by Gilli et al. in their 1970

[2] This design is similar to the helical coil heat exchanger. The coiled tube heat exchanger is essentially a flat helical coil heat exchanger, so the terms are often interchangeable. Since both designs can use similar methods of analysis, this section uses examples of both coiled tube and helical coil heat exchangers.

"Radial-flow heat exchanger" patent [19]. A diagram of their design is shown in Figure 1-6. The coiled tube heat exchanger is a type of shell-and-tube heat exchanger where one fluid flows outward radially over the tubes, and the other fluid flows inside the coiled tubes. There are two significant advantages to this geometry. First, it creates a more compact geometry than conventional shell-and-tube heat exchanger designs, ensuring a high heat transfer surface area density. For comparison, Table 1-1 compares the typical range of surface area density for each of the heat exchanger designs described in the section. Second, using coiled tubes instead of straight tubes also enhances heat transfer, especially in the laminar flow regime. When fluid flows through a coiled tube, centrifugal forces cause secondary fluid flow within the tube, creating greater mixing and enhancing heat transfer to the fluid outside of the tube [20]. Figure 1-7 shows a cross-section of this secondary flow in the tube. Both the enhanced heat transfer and the high surface area density give this design a high effectiveness. Depending on the tube size and number of tubes, the frictional pressure losses are also relatively small.

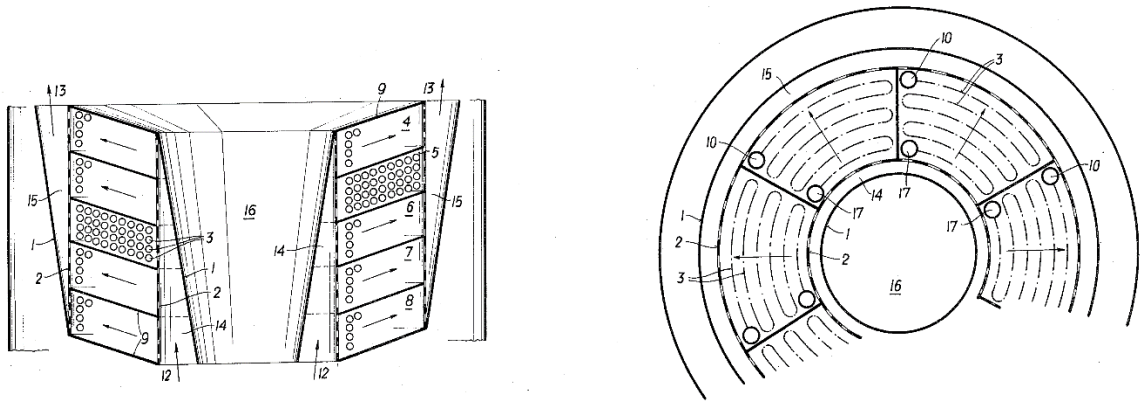

Figure 1-6. Plan (Left) and Elevation (Right) Views of Coiled Tube Heat Exchanger, from Gilli et al. patent [19]

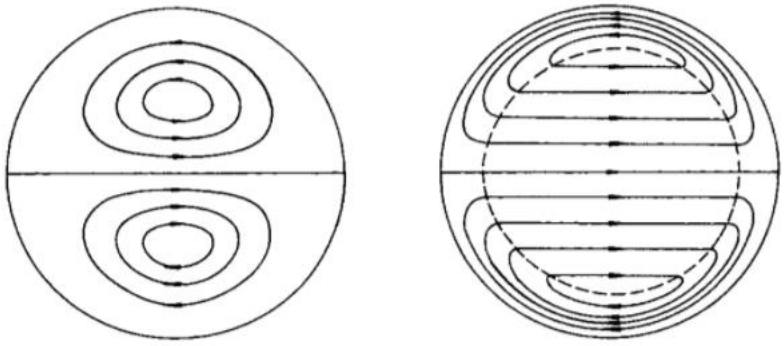

Figure 1-7. Secondary Flow Diagram of Tube Cross Section with Small Tube Curvature (Left) and Large Tube Curvature (Right) [20]

Table 1-1. Typical Surface Area Density of Various Heat Exchanger Designs

Compact Heat Exchanger	U-Tube Shell-and-Tube Heat Exchanger	Printed Circuit Heat Exchanger	Coiled Tube Heat Exchanger[3]
< 700 m^2/m^3	100-300 m^2/m^3	650 to 1300 m^2/m^3	~600-700 m^2/m^3

Like the PCHE, the coiled tube heat exchanger seems like an excellent design choice for use in the FHR based on the compactness, high effectiveness, and minimal pressure loss. Due to these advantages, the design has been used in industrial applications such as heat recovery systems, refrigeration, and process plants. Another application is aerospace engineering. For example, the pre-cooler in the SABRE rocket engine developed by the UK company Reaction Engines uses a coiled tube heat exchanger that operates at temperatures from over 1,000°C to -150°C [21]. A similar design has also been used for nuclear power applications. The US reactor design company, NuScale Power, uses a helical coil heat exchanger to generate steam in their SMR design [22]. So, there is added advantage of experience in manufacturing this type of heat exchanger for nuclear applications. Finally, unlike the PCHE, the coiled tube heat exchanger is more likely to be able to handle the thermal transients expected in the FHR. By using relatively small tubes, there is little heat transfer in the form of conduction; most of the heat transfer occurs as convection. The thermal inertia of the heat exchanger is relatively constant throughout the heat exchanger, so there are no large temperature gradients and consequently minimal stress concentrations. Since the tubes are seamless, the only part of the heat exchanger where stress concentrations and creep deformation over time could be an issue is where the tubes join manifolds. There is promising research into the best method to join the tubes to the manifolds, so it is likely that this will not be a major issue [23], [24]. With all of these reasons in mind, the coiled tube heat exchanger was chosen as the primary heat exchanger for Mk1 PB-FHR and RACC. This eventually led to the development of the Coiled Tube Gas Heater (CTGH) and, specifically for the FHR, the Coiled Tube Air Heater (CTAH).

1.3 Mk1 PB-FHR Coiled Tube Air Heater Design

The Mk1 PB-FHR CTAH is designed to have the low-pressure flibe salt inside of the tubes and the high-pressure air on the shell-side. This configuration put the tubes in compression instead of tension, reducing the risk of tubes bursting. As mentioned before, the tubes have a spiral geometry in the shape of an annulus in order to minimize the total volume of the heat exchanger while maximizing the heat transfer surface area between the flibe and air. A CAD model of the full CTAH, which has the flow direction of the flibe and air, is shown in Figure 1-8. The flibe enters the heater at the top of the pressure vessel and is distributed between large manifold pipes located around the outer edges of the tube bundle. The coolant flows down these manifold pipes as it is distributed between multiple sub-bundles stacked on each other. In each of the sub-bundles, the liquid flows inward to the corresponding inner manifold pipe mounted around the inside edge of the tube bundle annulus before flowing down out of the CTAH.

[3] There is little data on coiled tube heat exchanger surface density since many designs are considered intellectual property of the company that developed them. The numbers in this table are based on the CTGH designs discussed later in this thesis.

Figure 1-9 shows a CAD model of a sub-bundle for the Mk1 CTAH shown in Figure 1-8. For the tube side, the hot flibe starts at the manifold on the outer radius of the bundle and flows inward. The coolant flows through tubes that loop around the bundle multiple times before reaching the corresponding manifold at the inner radius. For the shell side, the cold[4] air enters through the bottom of the CTAH and flows upward through the center of the sub-bundles. Then, it flows radially outward through the spiral tube bundles that are arranged in a staggered pattern to more efficiently cool the flibe. The air continues to flow upward through the gap between the tube bundle and the vessel wall before exiting out the top of the pressure vessel. Using this arrangement, the CTAH acts essentially as a counterflow heat exchanger. The hot flibe inlet heats the hot air that is about to exit the CTAH bundle, and the cold flibe that is exiting the bundle heats the cold air entering it. This means that the temperature difference between the liquid and gas remains relatively small across the heat exchanger which replicates a counterflow heat exchanger and improves the overall heat transfer of the CTAH.

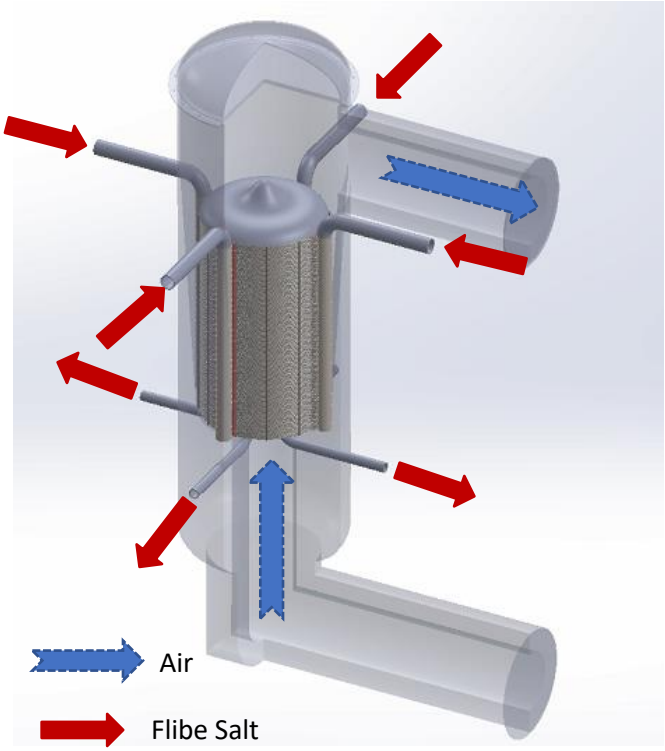

Figure 1-8. CAD Model of Mk1 PB-FHR CTAH

[4] The term "cold" is relative for this design. The cold air is 418.6°C and the cold flibe is 600°C.

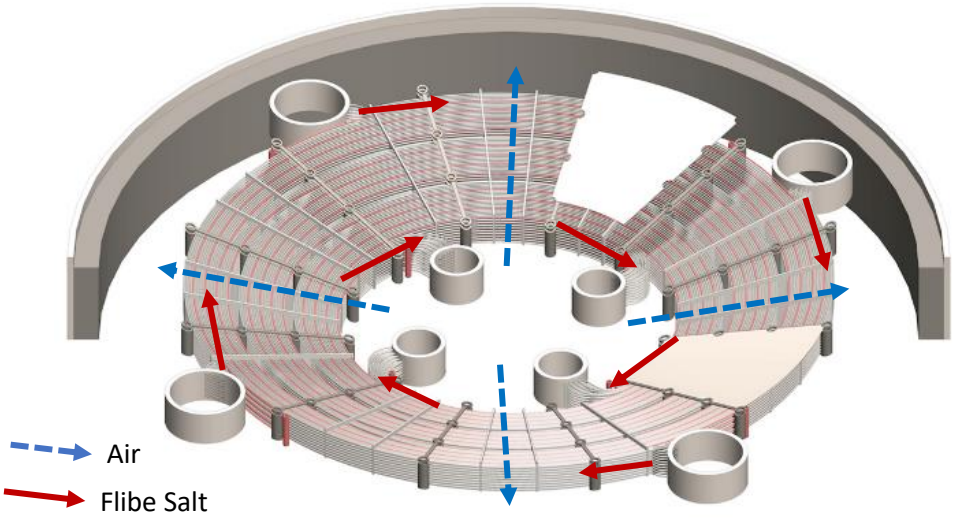

Figure 1-9. CAD Model of CTAH Sub-bundle

The CTAH incorporates some other components and characteristics to improve the overall design. In many shell and tube designs, flow-induced vibration is an issue that can lead to tube rubbing and eventual rupture. In order to reduce tube vibration, the CTAH incorporates anti-vibration rods and tube holders throughout the tube bundle. This is discussed further towards the end of Chapter 2. The tube holders not only reduce tube vibration; they also maintain the tube geometry and support the tube bundle. The tube holders support the tube bundle by using tie rods. The holes for these tie rods can be seen in Figure 1-9, which create gaps in the tube bundle. Another characteristic to improve the CTAH design is that each sub-bundle is separated by a spacer plate. These plates prevent vertical bypass flow within the bundle and guide the radial airflow. On the tube side, the flow is guided by the slope of the tubes. If there is a loss in pumping power, either due to an accident or a scheduled shutdown for maintenance, the sloped tubes would allow the flibe to drain out of the CTAH. Leaving the flibe in the tube bundle could lead to freezing and tube blockage. In order to deal with the issue of freezing, heaters rods are installed in the tube bundle. These rods are electrically heated to keep the flibe liquid when the reactor is shutdown. The heater rods replace tubes in the tube bundle, so they can reduce the heat transfer surface area density. Therefore, only the minimum number of heater rods needed to keep the flibe liquid during a shutdown should be used. With all of these design improvements, the CTAH becomes a more optimal design for the Mk1 PB-FHR coupled with the RACC and possibly other nuclear Brayton cycles.

1.4 Dissertation Motivation and Structure

The CTAH is an optimal design choice for coupling the FHR and RACC, but it is necessary to make more specific design choices, such as the size and spacing of the tubes, the number of sub-bundles, the layout of the tube bundle, etc. These design choices can affect the overall size of the heat exchanger, the effectiveness of the tube bundle, the air and salt pressure drop. When designing a reactor, it is a necessity to know the total heat transfer and pressure drop of a heat exchanger before building the reactor. The RACC and the FHR were designed

assuming that the primary heat exchanger could deliver a specific heat transfer. If the CTAH's heat transfer is too small, the power conversion would be less efficient and therefore less economical. It also means that the reactor would be undercooled and could increase the risk of accident scenarios due to overheating. If the CTAH transfers too much heat, this could overcool the reactor and lead to salt freezing. In order for the RACC to be as efficient and economical as possible, it is necessary to know the air pressure drop over the heat exchanger. The frictional pressure drop of the flibe in the CTAH is also important to know in order to properly size the salt pump for the reactor as the heat exchanger is a large source of head loss in the reactor's primary loop.

There are multiple ways to find the heat transfer and pressure drop for a design. One of the most straight forward approaches is to build a CTAH and test it experimentally. This approach is not economical as it can be costly to fabricate various CTAH designs. It also would be necessary to recreate the temperatures and pressures that the heat exchanger would operate at in order to test it experimentally. A simpler approach is to use empirical correlations to predict the heat transfer and pressure drops. The problem with this approach is that there are empirical correlations for simple geometry like flow in a curve tube and crossflow through a tube bundle, but there are no empirical correlations for the more complex geometry of the CTAH. It is therefore necessary to perform a computer simulation to take into account this complex geometry. One method would be to model this geometry using a CFD program or a Multiphysics simulation program, like COMSOL Multiphysics, to model the CTAH. Unfortunately, these programs were designed to model smaller or more simplistic geometries. For a heat exchanger as large as the CTAH, these programs can become computationally expensive, and the simulation can take many days to finish, assuming that the program is able to handle the simulation at all. In order to simulate the CTAH under the FHR and RACC conditions, it was necessary to develop a simulation program specific to the CTAH geometry. This program had many similarities with programs like COMSOL, but since its calculations were tailored to the CTAH geometry, it performed simulations much faster. It was also much easier and quicker to change the CTAH geometry since this simulation did not require modifying CAD models or rewriting long input files to simulate different CTAH geometries. The work performed in this dissertation led to the development of this program that can relatively quickly simulate the design, which will help with the development and licensing of the FHR. Before this program could be used, it was necessary to prove that it realistically models the CTAH. So, the program needed to be validated experimentally. After this validation, it was possible to examine other nuclear reactor applications for the CTAH, or more generally, the CTGH design. In order to do this, an optimization feature was added to the simulation program that would determine the optimal CTGH based on the nominal parameters for a particular nuclear Brayton cycle. This tool could speed up the heat exchanger design process for other nuclear applications.

This dissertation is split into five chapters. This first chapter gives background information on the FHR and the design of its primary heat exchanger, the CTAH. Chapter 2 focuses on the development of the program to simulate CTGHs for various nuclear applications. Then, the program is used to simulate the CTAH designed for the FHR to find its effectiveness, air pressure drop, flibe pressure drop, and overall size. Finally, the chapter looks at some additional program features that can be used to improve the tube bundle design that were

discussed earlier in Chapter 1. Chapter 3 focuses on experiments performed using the CTGH design. The primary experiments performed were for experimental validation of the program developed in Chapter 2, but there were additional experiments performed to study other characteristics about the CTGH design. Chapter 4 initially focuses on the development of the optimization tool that can develop CTGH designs for different applications. Then, the chapter looks at example applications of the optimization tool and shows the CTGH designs that were developed for these different applications. Chapter 5 is the final chapter that summarizes the results of this dissertation, gives some concluding remarks, and discusses possible future work.

Chapter 2.
Heat Exchanger Effectiveness Model

In order to perform a simulation analysis on the CTGH bundle, the Transverse Heat Exchange Effectiveness Model (THEEM) was developed. THEEM is a modified finite volume computer code developed in MATLAB to analytically predict the approximate effectiveness of the CTGH as well as the pressure drops across the tube bundle using both a 2-D and 3-D model. A 0-D model was developed as well for quick calculations and design optimization. In order to be applicable for a large range of applications, THEEM was developed to work with different geometries and heat transfer fluids. Finally, the code is flexible enough that future modifications can be made based on future experiments.

2.1 2-D Code Development

The code performs a finite volume simulation on a 2-D cross section of one of the sub-bundles. The simulation then calculates the effectiveness of the sub-bundle, the total heat transfer, the heat transfer distribution, and the temperature and pressure distribution of the liquid and gas/supercritical fluid across the sub-bundle. These calculations are performed under the assumption that the liquid and gas/supercritical fluid flowrates are evenly distributed between each sub-bundle and that the fluids do not undergo any temperature or pressure changes in the manifolds before entering the sub-bundles. For this reason, the 2-D model can be viewed as the calculating the average distributions and outlet parameters for the entire bundle.

2.1.1 Simulation Inputs

THEEM was designed to work with CTGHs with different bundle geometries and different heat transfer fluids with variable inlet conditions. For this reason, the user specifies the geometry and nominal operating parameters for the CTGH in an input file. An existing file can be used or a new file can be created using the GUI shown in Figure 2-1. This GUI was developed specifically for THEEM and can be used to create an input file for all versions of THEEM. However, THEEM will lock certain fields depending on the model. For example, the 2-D and 3-D models do not require the outlet gas and liquid temperatures, so those fields are locked and left blank in the GUI. For the 2-D model, THEEM requires the user to input the following heat transfer fluid properties for a CTGH application: (i) gas type[5], (ii) liquid type, (iii) bulk inlet gas temperature, (iv) bulk inlet liquid temperature, (v) mean inlet gas pressure, (vi) mean inlet liquid pressure, (vii) gas fluid mass flowrate, and (viii) liquid mass flow rate. It also requires the following geometrical data: (i) tube material, (ii) tube outer diameter (D_o), (iii) tube thickness, (iv) the longitudinal pitch-to-diameter ratio, or S_L, (v) the transverse pitch-to-diameter ratio, or S_T, (vi) the number of liquid manifolds ($N_{Manifolds}$), (vii) the number of times the tubes loop around the bundle (N_{loops}), (viii) the number of tubes per horizontal layer at each manifold (N_{rows}), (ix) the number of horizontal tube layers per sub-bundle (N_{layers}), (x) the total number of sub-bundles in the CTGH bundle (N_{sub}), (xi) the number of rows of tie rod gaps (N_{gap}), (xii) the width of those tie rod gaps (t_{gap}), (xiii) the number of columns of tube holders, (xiv) the

[5] Various gases, such as air or helium, or supercritical fluids, such as supercritical CO_2, can be used on the shell-side of the CTGH. However, for the sake of simplicity in this chapter, this shell-side fluid will be referred to simply as a gas.

mean inner radius of the tube bundle annulus ($R_{in,bund}$), (xv) the downward slope of the tubes for drainage, and (xvi) the number of tubes per layer that are replaced with a heating rod ($N_{heatrod}$)[6].

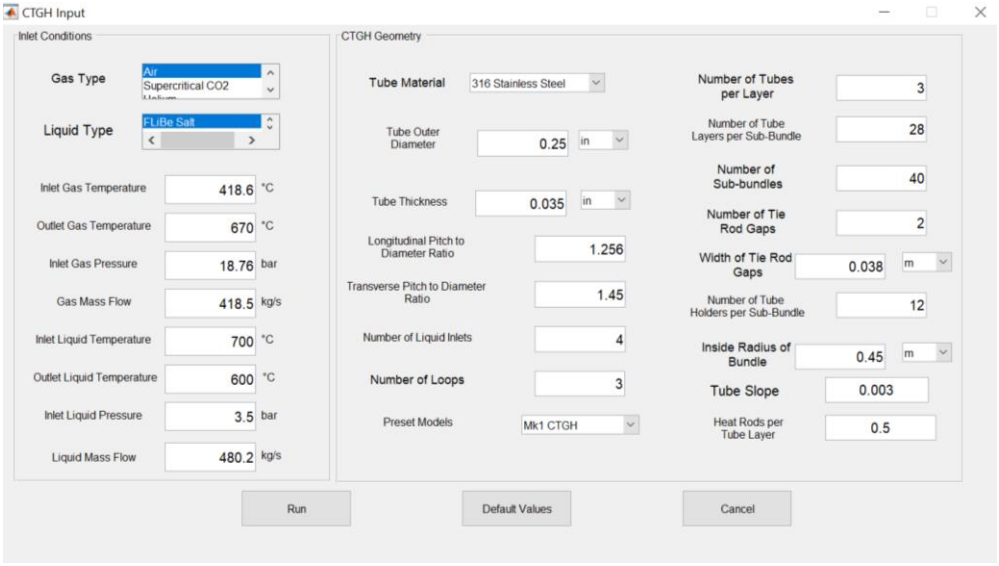

Figure 2-1. THEEM Input GUI

2.1.2 Bundle Geometry Calculations

Based on the CTGH geometrical parameters from the input file, THEEM can calculate the overall geometric parameters for the tube bundle, such as the bundle height and width. This is important to size the pressure vessel around the bundle. THEEM also finds the total number of tubes in the CTGH bundle, N_{tubes}, the number of radial/longitudinal tube rows, $N_{L,tot}$, the mean outer radius of the tube bundle, $R_{out,bund}$, and the total height of the tube bundle, H_{bund}.[7]

$$N_{tubes} = N_{sub} * N_{Manifolds} * N_{layers} * (N_{rows} - N_{heatrod}) \quad 2\text{-}1$$

$$N_{L,tot} = 2 * N_{Manifolds} * N_{loops} * N_{rows} \quad 2\text{-}2$$

$$R_{out,bund} = R_{in,bund} + (N_{L,tot} * S_L * D_o + N_{gap} * t_{gap}) \quad 2\text{-}3$$

$$H_{bund} = N_{bundles} * \left(D_o * S_T * \frac{N_{layers} + 1}{2} + t_{disk}\right) \quad 2\text{-}4$$

[6] It is likely that there will not be a heat rod in every row, so this number will likely be less than 1. For example, if this number is ½, this means that there is a 1 heater rod for every 2 layers.

[7] Equation 2-4 includes the variable t_{disk}, which is the thickness of the disks/plates separating sub-bundles. This thickness is obtained via a structural analysis of the bundle, which is outside the scope of THEEM.

2.1.3 Meshing Algorithm

An algorithm has been implemented to automatically generate a radial control-volume grid across the tube bundle geometry. One of the main differences between this grid algorithm and grid algorithms developed for other finite volume simulations is the size of the mesh. THEEM's methodology is based on empirical correlations for specific geometries instead of governing differential equations for fluid flow and heat transfer, such as the continuity equation, Navier-Stokes, and the Heat Equation. For the latter case, the generated mesh is relatively small in order to more accurately model the given geometry. However, for THEEM, the mesh needs to enclose a volume large enough that the empirical correlation can accurately model it. For example, the gas side correlations were developed for a bank of tubes in crossflow. Therefore, the mesh needs to be large enough to include a bank of tubes instead of creating multiple nodes across individual tubes.

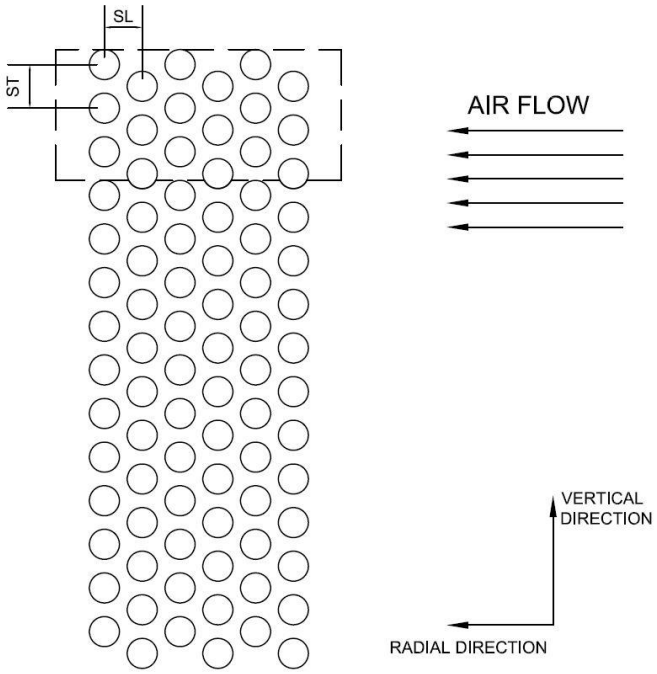

Figure 2-2. Tube Bundle Arrangement with Sample Control Volume

In order to simplify the calculations and minimize the computational time for THEEM, the grid algorithm was developed to create control volumes that include integer number of tubes. These volumes are approximately the same size and contain the same tube bank geometry. They are sized so that all of the tubes in each volume have liquid flowing in the same direction coming from the same injection manifold pipe. In order to form volumes like this, the algorithm uses the geometry of the tubes as they connect to each manifold. An example of how the tubes connect to the manifolds for the CTGH is shown in Figure 2-2. They will be sized so that all of the vertical tube rows are contained within one or two volumes radially. In this example, the volume encompasses all 6 vertical rows that connect to the manifold. For the height of the volumes, they will be sized so that the number of horizontal layers is divided as equally as possible between volumes while also keeping the height of the volume close to its width to maintain a cubic shape. For example, there are 28 tube layers in each sub-bundle as shown in Figure 2-2. The top four

volumes will contain 6 tube layers and the bottom will contain 4 tube layers. This gives the top four volumes close to a square shape. Finally, in the azimuthal direction, the mesh will form so that the volumes are relatively cubic in shape. Having the volume's azimuthal depth approximately equal to the radial width of the volume will guarantee three things. First, the volume is large enough to include a meaningful geometry to model with the empirical correlations. Second, it will be large enough to reduce the number of calculations and make the simulation less computationally expensive. Third, the volume will be small enough that the tube curvature will be negligible and the tube bank can be approximated as straight tubes in cross-flow for the shell-side calculations.

2.1.4 Volume Calculations

After THEEM generates the mesh over the cross-section, it then performs calculations over each volume. This section covers those calculations.

2.1.4.1 Heat Transfer Calculations

In order to find the heat transfer and outlet temperatures of the gas and liquid, Equation 2-5 through Equation 2-7 were used to model each control volume:

$$Q_{i,j} = \dot{m}_l C_{p_l} \left(T_{l_{\boldsymbol{i,j}}} - T_{l_{i,\mathrm{j}+1}} \right) \qquad 2\text{-}5$$

$$Q_{i,j} = \dot{m}_g C_{p_g} \left(T_{g_{i+1,j}} - T_{g_{i,j}} \right) \qquad 2\text{-}6^{8}$$

$$Q_{i,j} = UA_{i,j} * \left(\frac{T_{l_{i,j}} + T_{l_{\boldsymbol{i},j+1}}}{2} - \frac{T_{g_{\boldsymbol{i,j}}} + T_{g_{i+1,j}}}{2} \right) \qquad 2\text{-}7$$

$Q_{i,\mathrm{j}}$ is the heat transfer that occurs in the volume and $UA_{i,j}$ is the overall heat transfer coefficient based on the surface area of the tubes in the volume. These 3 equations have 3 unknowns:

(1) The outlet temperatures of the gas, $T_{g_{i+1,j}}$
(2) The outlet temperature of the liquid, $T_{l_{i,j+1}}$
(3) The heat transfer rate, $Q_{i,j}$.

The inlet temperatures are either the inlet temperatures for the bundle or the previous volume's outlet temperatures. The liquid and gas mass flow rates are based on the flow rate inputs. The heat capacities are temperature dependent properties of the fluids. The majority of the calculations are to find $UA_{i,j}$.

For each volume element, the overall heat transfer coefficient, UA, is calculated given the thermal resistance of the tube-side liquid, R_l, the tube wall, R_t, and the shell-side gas, R_g:

$$UA = \frac{1}{R_l + R_t + R_g} \qquad 2\text{-}8$$

[8] This equation assumes that the gas flow is purely radial. Future iterations of THEEM may solve for the 2-D or 3-D gas flow distribution. This will mean that the energy equation will have additional terms.

The thermal resistivities of the liquid, tube wall, and gas, respectively, are:

$$R_l = \frac{1}{h_l * N_t * (\pi * D_i * L)} \quad 2\text{-}9$$

$$R_t = ln\left(\frac{D_o}{D_i}\right) * \frac{1}{N_t * 2 * \pi * k_t * L} \quad 2\text{-}10$$

$$R_g = \frac{1}{h_g * N_t * (\pi * D_o * L)} \quad 2\text{-}11$$

For these equations, the tube length, L, and number of tubes, N_t, are based on the size of the volume cell determined by the meshing algorithm, and the tube inner and outer diameters, D_i and D_o, are obtained from THEEM's input. The convective heat transfer coefficients, h_l and h_g, are calculated using the definition of the Nusselt number. For example, the liquid Nusselt number is:

$$Nu_l = \frac{h_l * D_i}{k_l} \quad 2\text{-}12$$

Since these tubes are curved, THEEM needs to take into account the effect of the curvature of the tubes on heat transfer and pressure drop. So, it uses another dimensionless number: the Dean number, De. The Dean number is a modified version of the Reynolds number that accounts for tube curvature:

$$De = Re_l * \sqrt{\frac{D_i}{2 * R_{curv}}} \quad 2\text{-}13$$

R_{curv} represents the curvature of the pipe. When the Dean number is used, the Reynolds number criteria that determines the flow regime is also modified. The new flow regime criteria are[25], [26]:

$$Laminar\ Flow: Re \ \leq \ 2100 * (1 + 12\sqrt{\frac{D_i}{2 * R_{curv}}})$$

$$Transitional/Turbulent\ Flow: Re \ > \ 2100 * (1 + 12\sqrt{\frac{D_i}{2 * R_{curv}}})$$

By using the Dean number, the Nusselt correlation changes to account for the effect that the tube curvature has on the flow and heat transfer characteristics of the liquid. The tube

curvature causes a secondary flow within the tubes that enhances heat transfer, so correlations developed specifically for curved tubes must be used. Equation 2-14 gives the Nusselt correlation for a curved pipe with laminar flow [27]. This correlation was chosen because it is applicable to all Prandtl numbers and Dean numbers as long as the flow is laminar. The CTGH was initially designed to operate with laminar flow. However, in order for THEEM to work for a large range of applications of the CTGH, it uses Equation 2-15 to calculate the Nusselt number for a curved pipe with turbulent flow [28].

$$Nu_l = \left[\left(3.657 + \frac{4.343}{\left(1 + \frac{957}{Pr_l * De^2}\right)^2} \right)^3 + 1.158 * \left(\frac{De}{1 + \frac{0.477}{Pr_l}} \right)^{\frac{3}{2}} \right]^{\frac{1}{3}} \quad 2\text{-}14$$

$$Nu_l = 0.023 * {Re_l}^{0.65} * \ De^{0.2} * {Pr_l}^{0.4} \quad 2\text{-}15$$

Similar to the liquid, the gas Nusselt number is defined using the convective heat transfer coefficient:

$$Nu_g = \frac{h_g * D_o}{k_g} \quad 2\text{-}16$$

In order to be applicable to a large range of applications for different gases at different flow regimes, the Zukauskas Nusselt correlation was selected for THEEM [25], [29]:

$$Nu_g = C_2 C_1 {Re_g}^m {Pr_g}^{0.36} \left(\frac{Pr_g}{Pr_{s,o}} \right)^{\frac{1}{4}} \quad 2\text{-}17$$

This correlation can be used for gases with the following parameters:

$$\begin{Bmatrix} 0.7 \leq Pr_g \leq 500 \\ 10^3 \leq Re_g \leq 2 \times 10^6 \end{Bmatrix}$$

These ranges are large enough that this correlation should work for almost any gas and flow regime for which the CTGH would be designed. For example, the Mk1 PB-FHR CTAH has the following range of values: $0.70 \leq Pr_g \leq 0.72$ and $6.0 \times 10^3 \leq Re_g \leq 1.6 \times 10^4$, which fall within the Zukauskas formula parameters. Re_g is the gas Reynolds number using the tube outer diameter as a length scale, Pr_g is the gas Prandtl number at the bulk gas temperature, and $Pr_{s,o}$ is the Prandtl number of the gas at the tube's outer surface temperature. In this correlation, C_1 and m are obtained from empirical chart data based on the gas Reynolds number and the pitch-to-diameter ratios for the tube bank. These values are given in Table 2-1. C_2 is a correction factor based on the number of tube rows. If there are more than 20 tube rows, the gas

flow is assumed to be fully developed and C_2=1.0. For less than 20 rows, Table 2-2 gives the value of C_2.

Table 2-1. Constants for Zukauskas Correlation [25], [29]

Re_g	C_1	m
$10^3 - 2\times10^5$ $(\frac{S_T}{S_L} < 2)$	$0.35(S_T/S_L)^{1/5}$	0.60
$10^3 - 2\times10^5$ $(\frac{S_T}{S_L} > 2)$	0.40	0.60
$2\times10^5 - 2\times10^6$	0.022	0.84

Table 2-2. Correction Factors for Zukauskas Correlation [25]

Number of Tube Rows	**1**	**2**	**3**	**4**	**5**	**7**	**10**	**13**	**16**	**20**
C_2	0.64	0.76	0.84	0.89	0.92	0.95	0.97	0.98	0.99	1.0

2.1.4.2 Pressure Drop Calculations

For the liquid, the pressure drop across a control volume is calculated based on the formula for frictional head loss flowing through a pipe, under the assumption that the pressure drop across each tube in the control volume is equal. THEEM uses the Darcy-Weisbach equation:

$$\Delta P_l = f_l * \frac{L}{D_i} * \rho_l * \frac{{v_l}^2}{2} \qquad 2\text{-}18$$

The friction factor formulas for the coiled tubes depend on both the Dean number and the flow regime. If the flow in the pipe is laminar, then the Manlapaz-Churchill friction factor correlations are used [30]:

$$f_l = \frac{64}{Re_l}\left[\left(1 - \frac{0.18}{\left[1+\left(\frac{35}{De}\right)^2\right]^{1/2}}\right)^2 + \frac{De}{88.33}\right]^{1/2} \qquad De \le 20 \qquad 2\text{-}19$$

$$f_l = \frac{64}{Re_l}\left[1 - \frac{0.18}{\left[1+\left(\frac{35}{De}\right)^2\right]^{1/2}} + \frac{De}{88.33}\right]^{1/2} \qquad 20 < De \le 40 \qquad 2\text{-}20$$

$$f_l = \frac{64}{Re_l}\left[1 + \frac{De}{88.33}\right]^{1/2} \qquad De > 40 \qquad 2\text{-}21$$

If the flow in the pipe is in the transitional regime or turbulent, then the Rogers-Mayhew correlation is used to find the friction factor for the liquid [28]:

$$f_l = \left[0.076 * {Re_l}^{-0.25} + 0.00725 * \left(\frac{D_i}{2 * R_{curv}}\right)^{0.5}\right] * \left(\frac{Pr_l}{Pr_{s,i}}\right)^{-\frac{1}{3}} \qquad 2\text{-}22$$

For the gas flow, the pressure drop is predicted using the Zukauskas formula for pressure loss over a tube bank:

$$\Delta P_g = f_g * \chi * N_L * \frac{\rho_g * {v_g}^2}{2} \qquad 2\text{-}23$$

The friction factor, f_g, and the correction coefficient, χ, were found from graphs that were created using empirical data [25], [29]. The coefficient graphs for a staggered tube bank are shown in Figure 2-3.[9] These graphs could not easily be implemented directly into a code like THEEM since they are based on experimental measurements. However, an open source set of MATLAB scripts was developed in order to calculate those coefficients based on a given geometry and Reynolds number so that the pressure drop could be calculated [31]. These scripts were modified and implemented into THEEM so that the friction factor and correction coefficient could be calculated accurately.

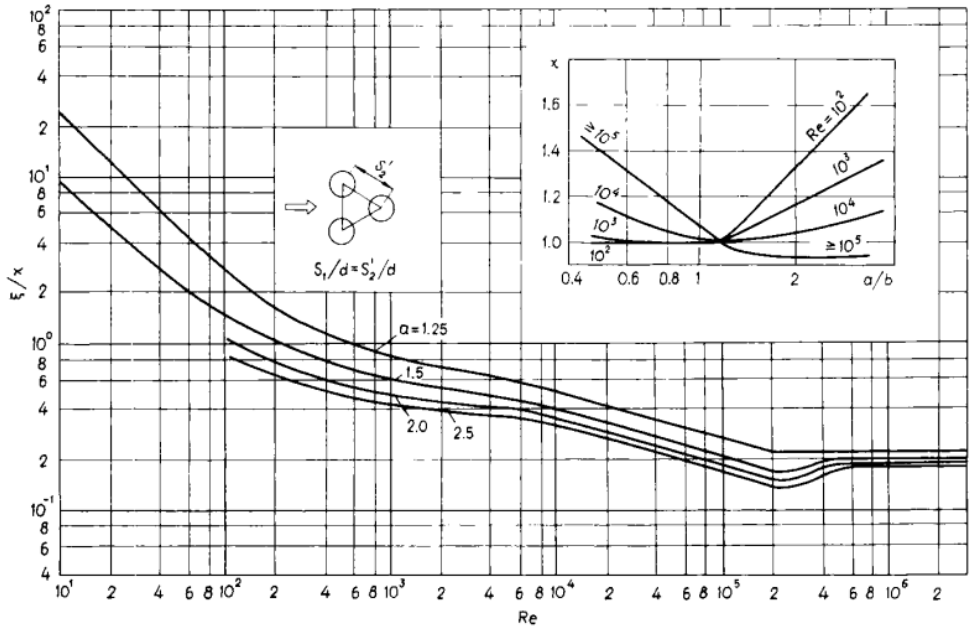

Figure 2-3. Zukauskas Graph of Pressure Drop Coefficients for a Staggered Tube Bank [29]

[9] In Figure 2-3, Zukauskas uses different notation than this dissertation. He uses the variables $\frac{Eu}{\chi}$ instead of f_g and a/b instead of S_T/S_L

2.1.5 Fluid Properties

In order to use the equations from Section 2.1.4, THEEM requires the thermophysical properties of the heat transfer fluids. Currently, THEEM has the material properties for the following liquids:

1. Molten flibe salt (LiF-BeF_2) [32], [33]
2. Molten flinak salt (LiF-NaF-KF) [33]
3. Molten nitrate salt for solar applications ($NaNO_3 - KNO_3$) [34]
4. Molten nabe salt (NaF-BeF_2) [32]
5. Liquid sodium [35]
6. Penreco Drakesol 260 AT Mineral Oil [36]
7. Water [37]

It has the material properties for the following gases/supercritical fluids [37]:

1. Dry Air
2. Helium
3. Supercritical CO_2

For each fluid, THEEM finds the following material properties:

1. Density, ρ
2. Heat Capacity at Constant Pressure, C_p
3. Dynamic Viscosity, μ
4. Thermal Conductivity, k
5. Prandtl Number, Pr

In the future, other fluids, such as humid air, can be added to THEEM for a more in-depth analysis. However, with humid air or other mixtures consisting of non-ideal gases, it will be necessary to include other thermophysical properties, such as vapor pressure. This will allow THEEM to also test for condensation throughout the heater. For now, it is assumed that any heat transfer liquid that is used in the CTGH will be relatively incompressible and will be operating near atmospheric pressure, so the liquid material properties are only temperature dependent. For the gases/supercritical fluids, the density is dependent on both the temperature and the pressure. The other fluid properties are assumed to be only temperature dependent.

Some of the fluid thermophysical properties have empirically derived temperature dependent equations. For example, the thermophysical property equations for molten salt flibe between 873-1073 K are given in Equation 2-24 through Equation 2-27 [32], [33]. Except for water, THEEM uses similar equations based on experimental measurements for estimating the other liquids' thermophysical properties over an appropriate temperature range.

$$\rho = 2279.92 - 0.488 * T(℃)\ [\frac{kg}{m^3}] \qquad 2\text{-}24$$

$$C_p = 2415.78\ \frac{J}{kg * K} \qquad 2\text{-}25$$

$$\mu = 0.000116 * e^{\frac{3755}{T[K]}} \, [Pa * s] \qquad 2\text{-}26$$

$$k = 0.629697 + 0.0005 * T[K] \, [\frac{W}{m * K}] \qquad 2\text{-}27$$

If the fluid thermophysical properties were given in tables, the tables were exported into THEEM. Then, THEEM used linear interpolation to find the material properties at the given temperature and pressure. For example, all of the gas and water properties were calculated using NIST tables [37].

2.1.6 Simulation Methodology

The 2-D THEEM model solves for the temperature distribution across the bundle by simultaneously solving the governing heat transfer equations for each volume (Equations 2-5 thru 2-7). These equations were selected because they are linear equations that can easily be solved using linear algebra. Equation 2-7 specifically was selected to use the Arithmetic Mean Temperature Difference (AMTD) formula over the Log Mean Temperature Difference (LMTD) formula. The AMTD is less accurate than the LMTD, however, the temperature changes of both the liquid and the gas in these volumes are small enough that the error of using the AMTD should be negligible. THEEM then applies a radial coordinate system to the entire cross-section and assigns a radial coordinate, i, and an azimuthal coordinate, j. THEEM starts at the first outer liquid manifold and follows the path of that tube loop. It calculates the heat transfer coefficient and liquid and gas pressure drops across each volume until it reaches the corresponding inner manifold. Then, it moves to the next outer manifold. It repeats this process for all loops in the sub-bundle. As THEEM moves around the sub-bundle, it also needs to account for the tie rod gaps between the tube rows. It is assumed that there is perfect mixing of the gas in the gaps. THEEM calculates the mean gas temperature entering each gap and estimates that to be the outlet temperature of each gap. It is also assumed that there is minimal gas pressure loss across these gaps.

In order to perform these calculations, the fluid thermophysical properties are needed. For the first run, THEEM assumes that these properties are constant across the bundle based on the inlet temperatures and pressures. After it has calculated the temperatures and pressures across the bundle, it repeats the calculations using properties based on the temperature and pressure distribution that were just derived for each volume. The simulation repeats this process until the derived temperature and pressure distributions converge to less than 1%. Then, it can perform the final heat exchanger effectiveness calculations and plot the results. The algorithm for how the 2-D model works is shown in a flowchart in Figure 2-4.

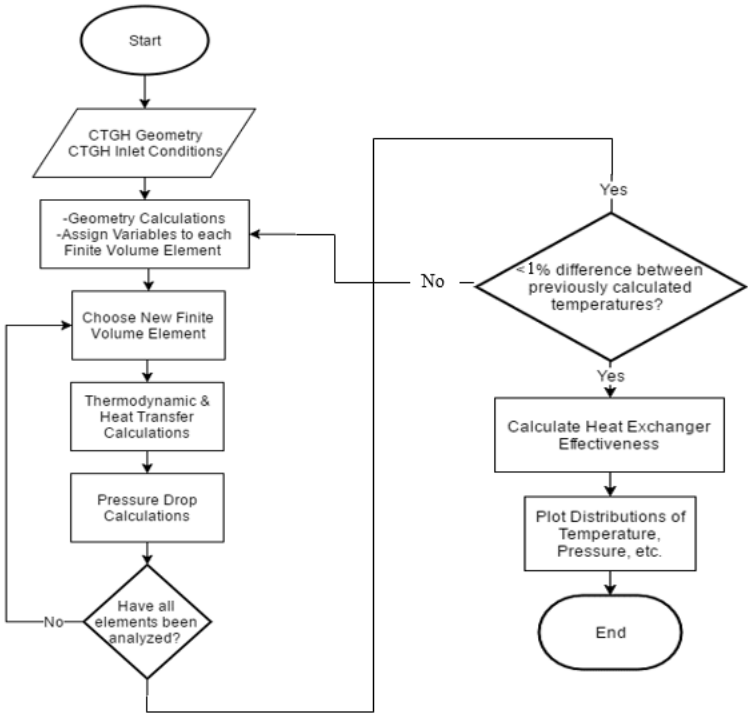

Figure 2-4. Flowchart of THEEM 2-D Model

2.1.7 Heat Exchanger Effectiveness Calculations

Once the simulation calculates the temperature, pressure, and heat transfer distributions for all of the volume elements across the sub-bundle, it finds both the overall effectiveness and the F-factor for the bundle. For the effectiveness, it uses Equation 2-28:

$$\varepsilon = \frac{Q_{tot}}{Q_{max}} \tag{2-28}$$

The program finds the actual heat transfer, Q_{tot}, by summing the heat transfer of each volume. The maximum heat transfer for the heat exchanger is found using the following equations:

$$Q_{max} = C_{min}\left(T_{l,in} - T_{g,in}\right) \tag{2-29}$$

$$C_{min} = min\left(\dot{m}_l C_{p_l}, \dot{m}_g C_{p_g}\right) \tag{2-30}$$

The F-factor is used to compare a heat exchanger to a perfect counterflow heat exchanger. It is calculated using Equation 2-31. In order to estimate the overall heat transfer coefficient, UA_{tot}, THEEM finds the mean U for each volume element and sums up the heat transfer surface area of each volume in the sub-bundle to obtain the total surface area for the cross-section. These are then multiplied together to obtain the overall heat transfer coefficient. Then, it finds the LMTD, ΔT_{LMTD}, based on the bundle inlet and outlet temperatures.

$$F = \frac{Q_{tot}}{UA_{tot} * \Delta T_{LMTD}} \qquad 2\text{-}31$$

Finally, using three-dimensional surface plots, THEEM plots the temperature and pressure distributions, as well as heat transfer distribution, across the sub-bundle.

2.2 3-D Code Development

One of the ultimate goals of THEEM was met when the 3-D simulation that could model the entire CTGH instead of just a single cross section of one sub-bundle was developed. The 3-D model can calculate the overall effectiveness of the entire CTGH. It gives the vertical distribution of the average outlet temperatures and pressures for each sub-bundle, which can be used to design the pressure vessel around the tube bundle. These results are also more accurate than the 2-D results because it uses a more realistic vertical distribution of liquid and gas flow rates. The 2-D model assumes that the flow rates are perfectly distributed between each sub-bundle, so it only needs to model one cross-section. However, the 3-D model actually calculates the flow and pressure loss in the manifolds before the fluids enter each sub-bundle. First, it calculates the liquid and gas mass flow rate for each sub-bundle cross section. Based on this information, it finds the pressure loss in the manifolds to find the pressure distribution of the fluid before it enters the bundle. Then, it performs a 2-D analysis of each cross section with these flow rates. The 3-D model essentially treats each 2-D cross section as a heat exchanger in parallel with the other 2-D cross sections, as shown in the diagram in Figure 2-5.

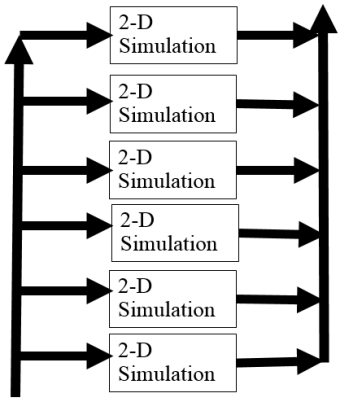

Figure 2-5. 3-D Simulation Methodology

The CTGH design allows for THEEM to model the bundle as multiple heat exchangers in parallel. For the tube-side, once the liquid has entered the tubes of a sub-bundle, it cannot mix with the liquid in the tubes of other sub-bundles until it enters the outlet manifold. For the shell-side, the sub-bundles are separated by spacer plates to prevent vertical flow distribution in the bundle. With these spacer plates, the gas flowing through each sub-bundle cannot mix with the gas flowing through any other sub-bundle until exits the tube bundle. It is also assumed that bulk gas temperatures will not vary more than a couple of degrees between adjacent sub-bundles. This small temperature gradient would mean that any conductive heat transfer across the spacer plates would be negligible.

2.2.1 Liquid Flow Distribution

In order to realistically model the mass flow distribution for each cross section, the 3-D simulation needed a generalized model for modeling flow in a manifold. A method for calculating the flow distribution in the liquid manifold is described by Wang [38]. This method involved performing a control volume analysis of the manifold. The control volumes were designed so that they each lined up with one "port" along the manifold. Each control volume's inlet was the outlet of the previous control volume in the manifold. The fluid could then exit the control volume to the next control volume in the manifold or it could exit through the port. A diagram of Wang's control volume is shown in Figure 2-6.

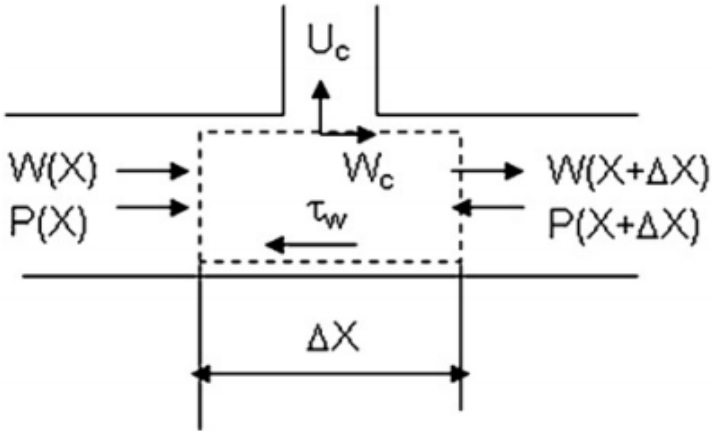

Figure 2-6. Manifold Control Volume Diagram [38]

In Figure 2-6, W(x) represents the velocity of the liquid in the manifold at location X, and U_c represents the liquid velocity flowing through the port. For the CTGH, the port would be the collection of tubes inside of a THEEM control volume. Using the manifold control volumes, Wang derives equations for the velocity of the liquid in the manifold and in each port as a function of position in the manifold. In order to obtain the velocity equations, Wang applies mass conservation (Equations 2-32 and 2-33), momentum conservation (Equation 2-34), and Bernoulli's Equation (Equation 2-35) to each control volume.

$$\rho F_M W = \rho F_M \left(W + \frac{dW}{dX}\Delta X\right) + \rho F_c U_c \qquad 2\text{-}32$$

$$\Delta X = \frac{L_M}{n} \qquad 2\text{-}33$$

$$\frac{1}{\rho}\frac{dP_M}{dX} + \frac{f}{D_H}W^2 + (2-\beta)W\frac{dW}{dX} = 0 \qquad 2\text{-}34$$

$$P_M - P_c = \rho\varsigma\frac{{U_c}^2}{2} \qquad 2\text{-}35$$

In Equations 2-32 thru 2-35, the subscript c refers to the port and the subscript M refers to the manifold. F_M is the flow area of the manifold, F_c is the flow area for each port, n is the

total number of ports along the manifold, L_M is the length of the manifold, β is the average velocity ratio in the manifold (W_c / W), P_M is the static pressure of the liquid in the manifold, f is the friction factor of the manifold pipe, and ς represents the average head loss coefficient for port flow, including friction factor and turning losses. The friction factor was estimated using the 0-D model, which is described later, to give a rough estimate of pressure loss through the tubes. The flow area of the "ports" is based on the number of tubes in volume defined by the THEEM meshing algorithm. Each volume with its multiple tubes is treated as one port. These equations were then non-dimensionalized using the correlations in Equation 2-36. Then, combining these sets of equations gives an ordinary differential equation for the velocity in the manifold whose solution is Equation 2-37. (Equations 2-39 thru 2-43 give definitions of the different variables in this solution.) Using this solution, the continuity equation (Equation 2-32), and the definition of ΔX (Equation 2-33), Wang was also able to derive Equation 2-38 to calculate the velocity in each port [38]. Then, given the density of the liquid and the various manifold and tube flow areas, THEEM can calculate the liquid mass flow rate for each sub-bundle based on the calculated velocities.

$$p_M = \frac{P_M}{\rho {W_0}^2}\ , p_c = \frac{P_c}{\rho {W_0}^2}\ , w = \frac{W}{W_0}\ , u_c = \frac{U_c}{W_0}\ , x = \frac{X}{L_M} \tag{2-36}$$

$$w_{i+1} = e^{\frac{-B_i x_{i+1}}{2}} \left[\frac{\sin(\frac{\sqrt{3}}{2} J_i [1 - x_{i+1}])}{\sin(\frac{\sqrt{3}}{2} J_i)} \right] \tag{2-37}$$

$$u_{c\,i+1} = \left(\frac{F_M}{2nF_c}\right) e^{\frac{-B_i x_{i+1}}{2}} \left[\frac{B_i \sin(\frac{\sqrt{3}}{2} J_i [1 - x_{i+1}]) + \sqrt{3} J_i \cos(\frac{\sqrt{3}}{2} J_i [1 - x_{i+1}])}{\sin(\frac{\sqrt{3}}{2} J_i)} \right] \tag{2-38}$$

$$J_i = \left[R_i + \sqrt{{Q_i}^3 + {R_i}^2} \right]^{1/3} - \left[R_i - \sqrt{{Q_i}^3 + {R_i}^2} \right]^{1/3} \tag{2-39}$$

$$B_i = \left[R_i + \sqrt{{Q_i}^3 + {R_i}^2} \right]^{1/3} + \left[R_i - \sqrt{{Q_i}^3 + {R_i}^2} \right]^{1/3} \tag{2-40}$$

$$Q_i = \frac{2 - \beta_i}{3\zeta_i} \left(\frac{F_c n}{F_M}\right)^2 = \frac{2k_i}{3\zeta_i} \left(\frac{F_c n}{F_M}\right)^2 \tag{2-41}$$

$$R_i = -\frac{f_i L_M}{4 D_h \zeta_i} \left(\frac{F_c n}{F_M}\right)^2 \tag{2-42}$$

$$k_i = \alpha + 2\gamma ln \frac{W_i}{W_o} \tag{2-43}$$

In these equations, W_0 is the liquid's velocity at the manifold's inlet, k is the pressure recovery factor, α is the pressure recovery factor of the first port branch, and γ is the increment of the pressure recovery factor along the geometry. The pressure recovery factor is the correction factor for the fluid losing some axial momentum when the fluid leaves the manifold through one of the ports. Both α and γ are dependent on the geometry of the manifold and should normally be determined experimentally. However, Wang [39] gives an estimate of $\alpha \cong 0.5$, $\gamma \cong 0.146$ for $20 \leq L_M/D_M \leq 30$ and $\alpha \cong 0.6$, $\gamma \cong 0.15$ for $30 < L_M/D_M \leq 40$. For the sake of THEEM modelling the CTGH, the estimates given by Wang should be sufficient. In Equations 2-37 and 2-38, w and u_c represent the dimensionless values of the manifold velocity and the port velocity along the manifold, respectively.

Finally, it is important to calculate the liquid pressure along the manifold to account for changes in pressure due to friction losses and momentum changes due to flow leaving the manifold. Wang inserts the manifold velocity solution (Equation 2-37) into the momentum equation (Equation 2-34) and integrates the equation in order to derive a formula for the static pressure change in the manifold, which is shown in Equation 2-44. In this equation, $p_{m,0}$ represents the nondimensionalized static pressure at the inlet of the manifold and $p_{m,i+1}$ is the liquid static pressure at x_{i+1} in the manifold. It is assumed that any heat transfer along this manifold is negligible compared to the heat transfer in the tube bundle itself. Under this assumption, THEEM assumes the bulk fluid temperature in the manifold does not change.

$$
\begin{aligned}
p_{m,i+1} - p_{m,0} = {} & \frac{f_i L_M}{4 D_h B_i \sin^2\left(\frac{\sqrt{3}}{2} J_i\right)} \left(e^{-B_i x_{i+1}} - 1\right) \\
& - \frac{f_i L_M}{4 D_h \left(B_i{}^2 + 3 J_i{}^2\right) \sin^2\left(\frac{\sqrt{3}}{2} J_i\right)} \Big\{ B_i e^{-B_i x_{i+1}} \cos\left[\sqrt{3} J_i (1 - x_{i+1})\right] \\
& - \sqrt{3} J_i e^{-B_i x_{i+1}} \sin\left[\sqrt{3} J_i (1 - x_{i+1})\right] + B_i \cos\left(\sqrt{3} J_i\right) \\
& + \sqrt{3} J_i \sin\left(\sqrt{3} J_i\right) \Big\} - k_i \frac{e^{-B_i x_{i+1}} \sin^2\left[\frac{\sqrt{3}}{2} J_i (1 - x_{i+1})\right]}{\sin^2\left(\frac{\sqrt{3}}{2} J_i\right)}
\end{aligned}
\qquad 2\text{-}44
$$

2.2.2 Gas Flow Distribution

In order to model the gas flow rate distribution in the center of the tube bundle, it is necessary to treat this center area of the tube bundle as a manifold. However, unlike the liquid manifolds, this manifold does not have individual "ports". The gas flows upward through the inside of the annulus while flow is distributed through the tube bundle in every direction. Instead of using a pipe with individual ports branching off, the gas "manifold" can be modeled as a uniformly distributed porous pipe. Many chemical reactors use a porous pipe with constant cross-sectional area to distribute the chemical species uniformly throughout the reactor, which motivated Wang to model this type of manifold as well. Wang gives a diagram of what this flow would look like in Figure 2-7 [39]. The tube bundle can be modeled as a porous structure surrounding the center "pipe" in all directions. However, since the liquid manifolds and the gas

"manifold" flow in opposite directions in the CTGH, the position in the gas manifold will be given by the variable Y so that $Y = L_M - X$.

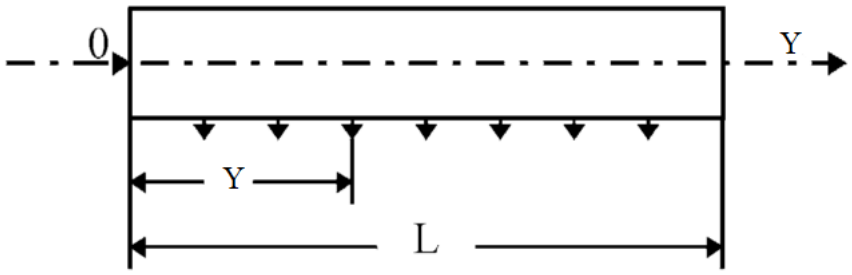

Figure 2-7. Diagram of Porous Pipe Manifold Flow Distribution [39]

Using the same governing equation as the liquid manifold (Equations 2-32 thru 2-35), Wang derives the same ordinary differential equation to model the flow velocity in the manifold. However, with the porous pipe, Wang states that if the "port" holes are the same size and are distributed uniformly along the length of the pipe, it can be assumed that there should be uniform fluid flow through each "hole". This means that the fluid velocity in the gas manifold will vary linearly from a maximum at the inlet to zero at the end. This gives Equation 2-45 to model the velocity in the gas manifold, with w_g representing the non-dimensionalized gas velocity and y representing the nondimensionalized location in the manifold.[10]

$$w_g = 1 - y \qquad 2\text{-}45$$

Then, similar to the liquid manifold derivation, this equation can be inserted into the continuity equation to give Equation 2-46, which gives the fluid velocity in each port. Since it is assumed the flow is uniform across the tube bundle, the port velocity is constant in terms of y.

$$u_{g,c} = \left(\frac{F_{M,g}}{nF_{c,g}}\right) \qquad 2\text{-}46$$

The derivation of the port velocities and consequently the gas mass flowrates was relatively simple. However, it is also necessary to calculate the pressure distribution along the manifold in order to know what gas inlet pressure at each sub-bundle. Similar to the liquid manifold, in order to find the pressure change throughout the gas "manifold", the equation for the manifold flow velocity (Equation 2-45) can be inserted into the gas manifold momentum equation.[11] Integrating that equation gives an equation for the pressure change. Using the Reynolds number to determine whether the manifold gas flow regime is laminar, transitional, or turbulent, Wang derived Equations 2-47 thru 2-49 to model the pressure along the manifold in

[10] The gas manifold equations use similar non-dimensional parameters as the liquid manifold, i.e. $w_g = \frac{W_g}{W_{g,0}}$, $u_{g,c} = \frac{U_{g,c}}{W_{g,0}}$, $y = \frac{Y}{L_M}$, where $W_{g,0}$is the inlet gas velocity.

[11] This equation is nearly identical to the liquid manifold momentum (Equation 2-34) except for using the appropriate variables for the gas manifold.

terms of the Euler number, $Eu_{y,0} = \frac{(P_{m,g,y} - P_{m,g,0})}{\rho_g {W_{g,0}}^2}$, where $P_{m,g,0}$ is the inlet gas static pressure [39]. These equations use the Reynolds number at each point along the manifold to determine the flow regime, but it uses the Reynolds number at the inlet, $Re_{g,0}$, for the actual calculations. The equations also use the pressure recovery factors α and γ. These factors have the same values as the liquid manifold. D_h is the hydraulic diameter of the gas "manifold."

For $Re_g \leq 2200$:

$$Eu_{y,0} = \left(\alpha - \frac{16L_M}{D_h Re_{g,0}}\right)[1-(1-y)^2] - 2\gamma\left[(1-y)^2 ln(1-y) - \frac{1}{2}y(y-2)\right] \quad 2\text{-}47$$

For $2200 < Re_g < 10^5$:

$$Eu_{y,0} = \alpha[1-(1-y)^2] - \frac{0.058L}{D_h {Re_{g,0}}^{0.25}}[1-(1-y)^{2.75}] - 2\gamma\left[(1-y)^2 ln(1-y) - \frac{1}{2}y(y-2)\right] \quad 2\text{-}48$$

For $Re_g \geq 10^5$:

$$Eu_{y,0} = \alpha[1-(1-y)^2] - \frac{0.0032L}{6D_h}[1-(1-y)^3] - \frac{0.04L}{D_h {Re_{g,0}}^{0.237}}[1-(1-y)^{2.763}] - 2\gamma\left[(1-y)^2 ln(1-y) - \frac{1}{2}y(y-2)\right] \quad 2\text{-}49$$

2.3 0-D Code Development

The THEEM 0-D model was designed mainly as rough calculation that could be used to calculate the size of the tube bundle, estimate the total pressure losses across the tube bundle, and give an estimate of the F-factor. Unlike the 2-D and 3-D models, the 0-D model requires the estimated outlet temperatures of the gas and liquid. Then, using the F-factor, it can be used to determine if a certain bundle geometry can deliver the desired heat transfer. For example, if the F-factor is greater than 1, that geometry will not work with the given fluid parameters. Also, since the 0-D model requires little time or memory, it can be used as a rough estimate for the pressure loss calculations required for the 3-D manifold flowrate calculations and for the optimization program discussed later in Chapter 4.

As for the actual calculations, it uses the same heat transfer and pressure loss correlations as the 2-D and 3-D models. The main difference is that it does not split the bundle into individual volumes. It finds the overall heat transfer surface area and calculates the average heat transfer coefficient of the entire bundle. It does not take into account the different pressure and temperature distribution across each sub-bundle. For the shell-side calculations, it uses the mean flow area to find the pressure loss and flow velocity. In order to find this gas flow area, THEEM

uses the middle of the tube bundle, $R_{avg,bund}$. This point is the average of the inner bundle radius, $R_{in,bund}$, and the outer bundle, $R_{out,bund}$, found using Equation 2-3. The circumference of the bundle at this radius is found and then multiplied by the height of the bundle, which is found using Equation 2-4, giving the gas flow area. For the tube-side calculations, it calculates the average tube length using Equation 2-50. It uses this parameter to estimate total heat transfer surface area and the tube-side pressure loss.

$$L_{tube} = N_{loops} * 2 * \pi * R_{avg,bund} \quad 2\text{-}50$$

Once it calculates the overall heat transfer coefficient, U, for the tube bundle and its total heat transfer surface area, it calculates the surface area required for an ideal counterflow heat exchanger that has the same heat transfer coefficient, heat transfer, and log-mean temperature difference. The F-factor is then calculated as the ratio of the ideal counterflow heat exchanger surface area, A_{ideal}, to the actual surface area, A_{actual}.

$$F = \frac{Q_{actual}}{Q_{ideal}} = \frac{UA_{actual}\Delta T_{LMTD}}{UA_{ideal}\Delta T_{LMTD}} = \frac{A_{actual}}{A_{ideal}} \quad 2\text{-}51$$

2.4 Results for Mk1 FHR Design

2.4.1 2-D Model Results

The Mk1 FHR CTAHs were modeled using both the 2-D and 3-D THEEM models. The 2-D model gives an estimate of what the average sub-bundle cross-section will look like. Since the RACC design includes both a high-pressure (HP) and low-pressure (LP) CTAH, both designs were modeled in THEEM for comparison. The design parameters for the RACC CTAHs are given in Table 2-3 [10], [11].

Table 2-3. Mk1 FHR CTAH Fluid Parameters

Inlet Parameter	Flibe Salt	HP Air	LP Air
Temperature	700.0ºC	418.6ºC	418.6ºC
Pressure	3.50 bar	18.76 bar	4.99 bar
Mass Flow Rate	480.2 kg/s	418.5 kg/s	418.5 kg/s

Since the only difference between the LP CTAH and the HP CTAH is the air inlet pressure, they will have the same geometry. This simplifies modeling and reduces manufacturing and design costs. Based on the RACC and Mk1 FHR design, the CTAHs would be design for a nominal heat transfer rate of 116 MW each. Based on these RACC design parameters and minimizing the overall pressure loss, the CTAHs were designed with the geometry parameters given in Table 2-4.

Based on this design, the tube bundle has an outer diameter of 2.20 m and a height of 5.46 m. The design of the FHR calls for all components to be rail transportable, limiting the width of components to less than 3.5 to 4 m. This tube bundle design is small enough that a pressure vessel can be fabricated around it while keeping its overall size well under the rail-

transportability limit. THEEM also predicts that this design will give the desired heat transfer with minimal pressure loss on both the tube and shell-side, as shown in Table 2-5.

Table 2-4. Mk1 FHR CTAH Geometry

Tube Outer Diameter	0.635 cm (0.25 in)
Tube Wall Thickness	0.0889 cm (.035 in)
Longitudinal Pitch-to-Diameter Ratio (S_L)	1.256
Transverse Pitch-to-Diameter Ratio (S_T)	1.45
Number of Liquid Manifolds	4
Number of Loops	3
Number of Tubes per Layer per Manifold	3
Number of Tube Layers per Sub-bundle	28
Number of Sub-bundle	40
Number of Tie Rod Gaps	2
Width of Tie Rod Gaps	3.80 cm
Number of Tube Holders	12
Annulus Inner Radius	45 cm
Tube Slope	0.003
Heating Rods per Tube Layer	1/2

Table 2-5. 2-D THEEM Prediction for Mk1 FHR CTAHs

Parameter	**HP CTAH**	**LP CTAH**
Effectiveness	0.917	0.917
F-factor	0.968	0.968
Estimated Total Heat Transfer	119 MW	119 MW
Flibe Mean Outlet Temperature	597ºC	597ºC
Flibe Pressure Drop	2.75 bar	2.75 bar
Air Mean Outlet Temperature	678ºC	678ºC
Air Pressure Drop	0.0908 bar	0.353 bar

As the results in Table 2-5 show, changing the air inlet pressure of the CTAH does not affect the effectiveness or overall heat transfer of the heat exchanger. The only difference is the air pressure loss. This can be attributed to both heat exchangers having the same geometry and mass flow rate. Modeling the air as an ideal gas, the density of the air is directly proportional to its pressure. The density of the air will be lower at the lower pressure, but since the mass flow rate remains constant, the air velocity through the heat exchanger increases to offset the decreased density. Assuming that the temperatures are the same, $\rho v = constant$. This relationship means that the air Reynolds number will be the same for both heat exchangers since they have the same geometry and temperature distribution. In Figure 2-9, THEEM predicts that the air Reynold number distribution across both the LP CTAH and HP CTAH are identical[12],

[12] The gaps in this figure and other THEEM figures in this section represent the tie rod gaps in the design. THEEM does not calculate the Reynolds numbers in these gaps.

ranging between 5,900 and 16,000. As Equation 2-17 indicates, the air's Nusselt number is a function of the Prandtl number and Reynolds number. The effect of the pressure is negligible on the gas Prandtl number, so the Nusselt number, and consequently the thermal resistance, of the air will be identical for both heat exchangers. However, the air pressure drop is a function of the density and the velocity squared as shown in Equation 2-23. The increased velocity will lead to a higher pressure drop, as shown in Table 2-5.

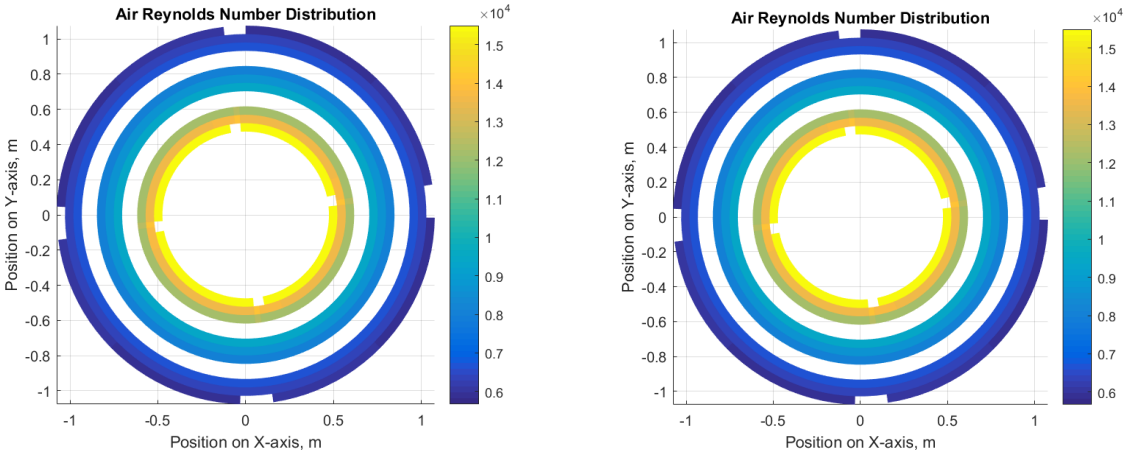

Figure 2-8. Air Reynolds Number Distribution of Mk1 HP CTAH (Left) and LP CTAH (Right)

The THEEM results indicate that this heat exchanger design has a high effectiveness. Also, given its F-factor of 0.968, it approximates a counterflow heat exchanger well. This is further proven in the flibe and air temperature distributions in Figure 2-9.[13] The location of the lower temperature flibe at the inner radius corresponds to the location of the lower temperature air during steady-state operation. The hotter flibe salt that enters the bundle is also at the same location as the hot air exiting the bundle. Figure 2-10 shows that most of the heat transfer occurs towards the center of the tube bundle at the lower temperatures.

[13] Since the LP and HP CTAHs are identical except for their air pressure distributions, only the results from the HP CTAH will be shown in these results, except where indicated.

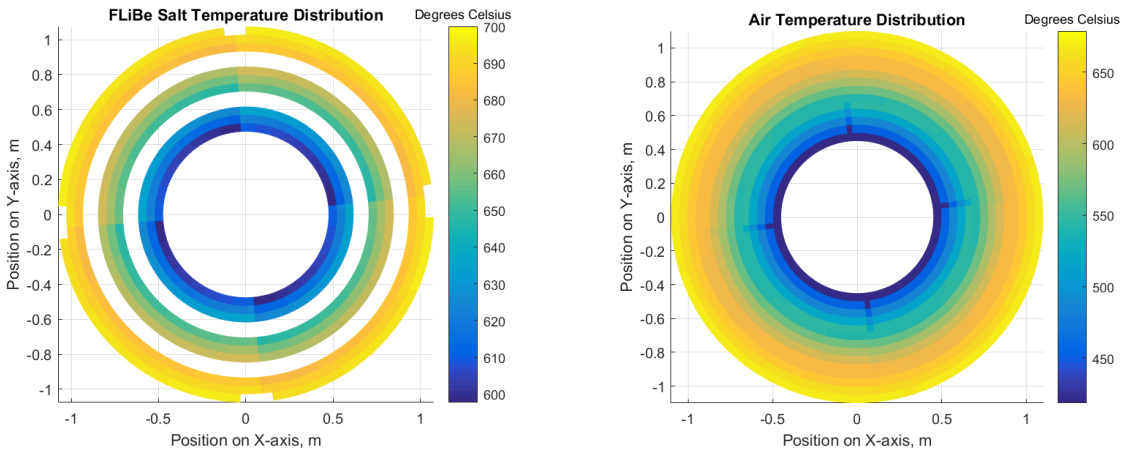

Figure 2-9. Mk1 CTAH Flibe (Left) and Air (Right) Temperature Distribution

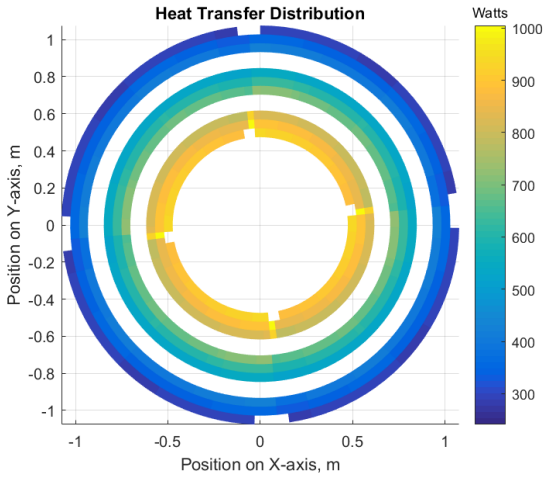

Figure 2-10. Mk1 CTAH Heat Transfer Distribution

For the pressure distribution of the flibe shown in Figure 2-11, the pressure decreases as expected following each tube loop, starting at each of the flibe outer manifolds. This is then used to find the overall flibe pressure loss, which can then be used in the salt pump sizing calculations for the FHR design. Figure 2-12 shows the pressure distribution of the air across both the HP and LP CTAH. The pressure decreases radially as the air flows outward over the tube bundle. The HP CTAH has a 0.48% decrease in air pressure, whereas the LP CTAH has a 7.08% decrease. It is important to minimize this pressure loss because it minimizes the circulating power loss and increases the overall efficiency of the RACC.

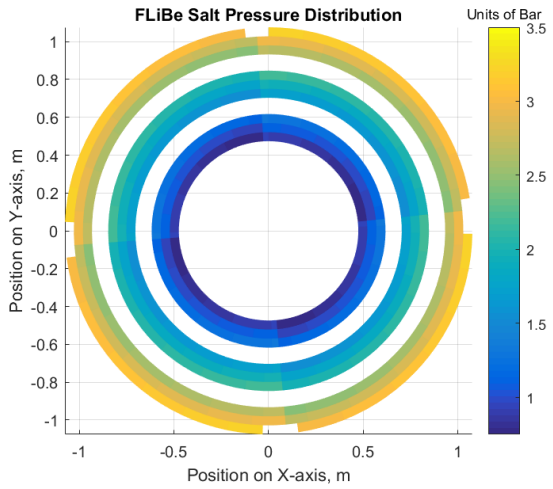

Figure 2-11. Flibe Pressure Distribution for Mk1 CTAH

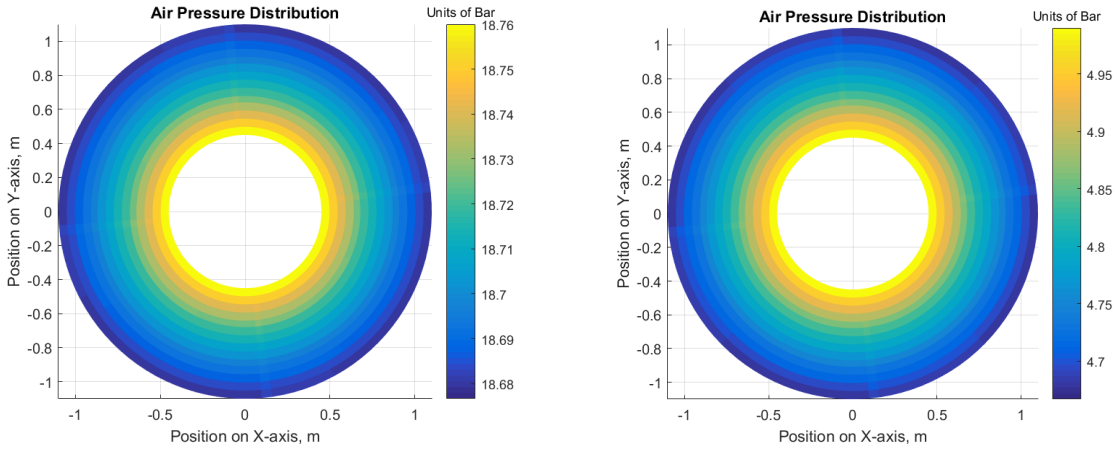

Figure 2-12. Air Pressure Distribution for HP CTAH (Left) & LP CTAH (Right)

Finally, THEEM also calculates the tube inner surface temperature around the tube bundle based on the heat transfer, salt bulk fluid temperature, and salt convection heat transfer coefficient at each point. One of the larger design challenges with the FHR design is preventing the molten salt from freezing. Molten flibe salt has a relatively high freezing temperature of ~459ºC [8], [32]. The salt temperature distribution in Figure 2-9 shows that the bulk fluid temperature stays well above freezing. However, there is still the possibility of freezing at local points along the tube wall. Fortunately, as Figure 2-13 shows, the tube wall temperature stays well above the freezing point of the salt. Even at its coldest location, the tube wall is approximately 90ºC higher than the freezing point. So, during normal operation, the CTAH will not encounter any localized or bulk salt freezing.

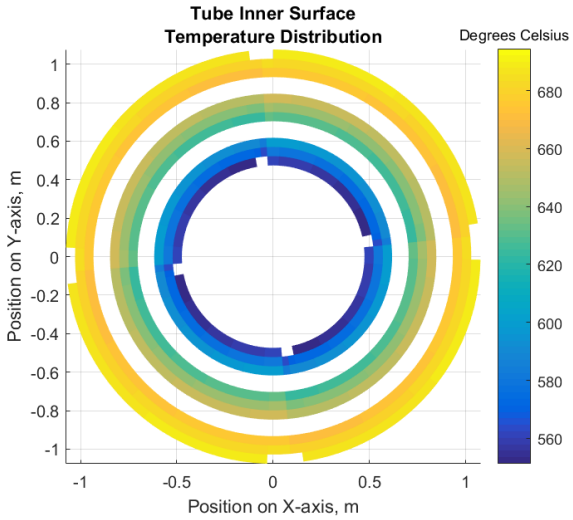

Figure 2-13. Tube Wall Inner Surface Temperature Distribution

2.4.2 3-D Model Results

After using the 2-D model to estimate the effectiveness, temperature distribution, and pressure drops across the manifold, the CTAHs were then modeled using the 3-D version of THEEM. This 3-D analysis used the same input parameters as the 2-D analysis, which are given in Table 2-3 and Table 2-4. First, the 3-D model calculated the mass flow rate in each manifold. Figure 2-14 shows what those flow distributions looked along the vertical axis of the CTAH.[14] The 3-D model uses the vertical position in the CTAH, starting at the bottom, as the x-axis for each figure it generates. Since the air and flibe flow in opposite directions in their respective manifold, it was necessary to choose one set of axes in order to prevent any confusion in the results. As Figure 2-14 shows, the maximum flow rate for each fluid in their respective manifold occurs at the inlet of that manifold. For the air, that is at the bottom of the bundle before it flows up into the bundle. For the salt, it is at the top of the bundle before it flows down each manifold outside of the bundle. The air manifold mass flow rate is modeled as a linear function based on its position that starts at its maximum flow rate and ends at 0 as it moves through the manifold. (See Equation 2-45.) However, it should be noted that the salt manifold also appears to approximate a linear relationship even though Equation 2-37 is not linear function. This is likely due to the even distribution of numerous ports along the liquid manifold. Given that there are a large number of ports for the liquid manifold, it appears to be approximating a porous manifold, similar to the air "manifold."

[14] As with the 2-D model, the LP and HP CTAH were identical except for air pressure drop. So, unless specified otherwise, only the results of the HP CTAH are shown in each figure.

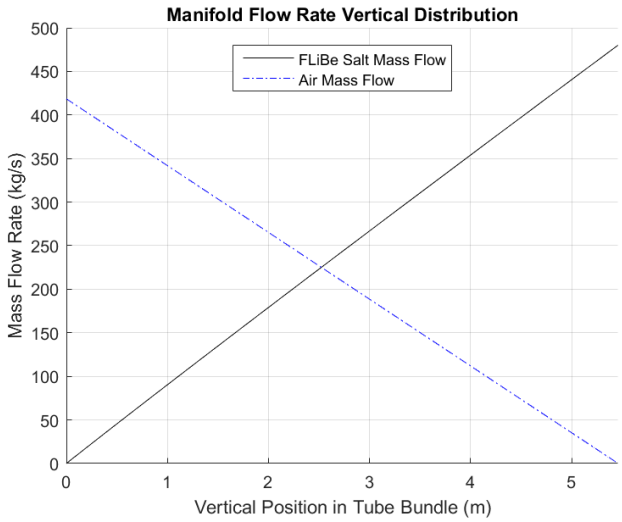

Figure 2-14. Vertical Distribution of Flow Rate in CTAH Manifolds for both Flibe and Air

THEEM then calculated the pressure changes in these manifolds as well as finding the mass flow rate for each sub-bundle. Figure 2-15 shows the mass flow rate of the flibe salt for each sub-bundle.[15] This vertical distribution calculated by the 3-D model is compared to the flow rate estimated by the 2-D model. The flowrate does not vary too greatly with a range of 2.94 kg/s to 3.27 kg/s and a mean flow rate of 3.01 kg/s, which is close to the 2-D flowrate of 3.00 kg/s. As seen in Figure 2-15, the flibe flowrate is lowest near the inlet of manifold at the top of the tube bundle. It increases as the flibe flowrate in the manifold decreases. The sharp increase near the bottom of manifold corresponds to the flow becoming laminar in the manifold. For the air-side, Equation 2-46 indicates that the flowrate to the bundle is not a function of position in the "manifold." So, as Figure 2-16 shows, the flowrate to each sub-bundle is constant for each sub-bundle cross-section and is identical to the air flowrate used in the 2-D model.

[15] This the combined flowrate of all of the liquid manifolds. It is assumed that the flow is distributed evenly between all of the liquid manifolds.

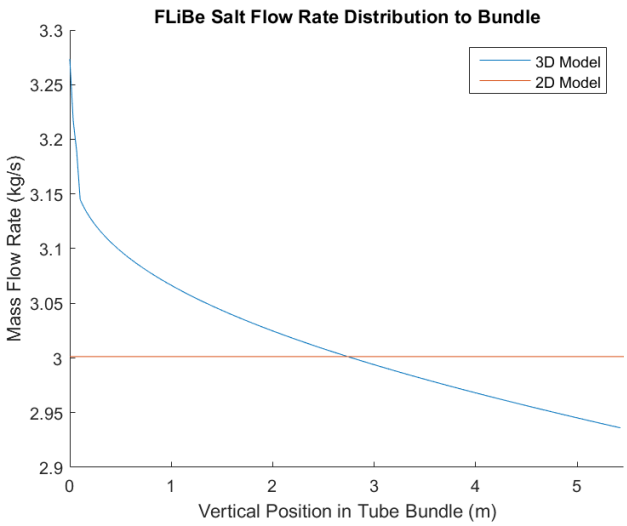

Figure 2-15. Vertical Distribution of Flibe Flowrate to each CTAH sub-bundle

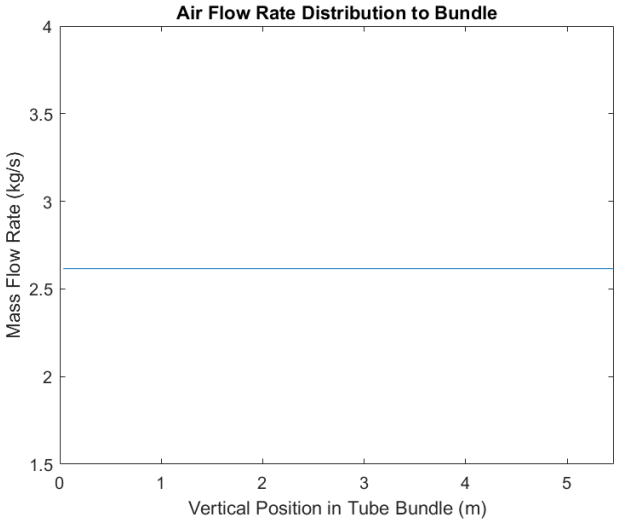

Figure 2-16. Vertical Distribution of Air Flowrate to each CTAH sub-bundle

The overall results for the 3-D model are given in Table 2-6. As with the 2-D model, the only difference between the LP CTAH and the HP CTAH are the air pressure drops. The effectiveness and F-factors were calculated based on the mean outlet air and salt temperatures. The mean outlet temperatures and pressure drops were calculated using a weighted average based on the mass flowrate of each cross-section. The total heat transfer was found by summing up the heat transfer of each cross-section. The 3-D model confirms a high effectiveness and high F-factor for this design and matches the 2-D model almost perfectly with the heat transfer and effectiveness results. Between the two models, the effectiveness has a percent difference of 0.02% and the F-factor has a percent difference of 0.03%. The 2-D model predicts a lower heat transfer of 118.7 MW because it does not account for the possibility of higher rates of heat transfer vertically in different sub-bundles. As Figure 2-17 shows, the heat transfer increases as

the salt flow rate increases through the tubes. The spike in heat transfer near the bottom of the CTAH tube bundle corresponds to the spike in the salt flow rate in Figure 2-15. The outlet temperatures of both the salt and the air follow the same pattern as shown in Figure 2-18 and Figure 2-19. For the salt, only the mean outlet temperature is shown because there is little variation between the salt temperatures in each manifold at each cross-section. (The 2-D results show that there was almost no difference between the flibe outlet temperatures in each manifold.) For the air, the outlet temperature varies around the outer diameter of the bundle, as shown in Figure 2-9 in the 2-D results. This is due to the different flow paths of the air being heated by salt at different temperatures around the loop. So, in order to show the azimuthal variation in the outlet air temperatures at each cross-section, Figure 2-19 shows the minimum, mean, and maximum outlet temperature at each vertical position of the tube bundle. They vary at the same rate as the heat transfer and salt flow rate.

Table 2-6. 3-D THEEM Prediction for Mk1 FHR CTAHs

Parameter	**HP CTAH**	**LP CTAH**
Effectiveness	0.918	0.918
F-factor	0.968	0.968
Total Heat Transfer	119 MW	119 MW
Flibe Mean Outlet Temperature	598ºC	598ºC
Flibe Pressure Drop	2.76 bar	2.76 bar
Air Mean Outlet Temperature	678ºC	678ºC
Air Pressure Drop	0.125 bar	0.490 bar

The flibe pressure drop distribution and air pressure drop distributions are given in Figure 2-20 and Figure 2-21, respectively. For the flibe pressure drop, the 2-D and 3-D models give similar prediction. The 3-D model has a slightly higher pressure drop, which comes from a combination of the vertical pressure distribution shown in Figure 2-20 and the friction loss in the manifolds. Similar to the temperature distribution of the flibe, the change in pressure between each inlet manifold and its corresponding outlet manifold is the same for each loop in each cross-section, so the mean pressure drop is sufficient. There is also a higher pressure drop in the cross-sections near the bottom of the bundle because of the higher salt mass flow rates through these tube bundles. The higher flow rates mean higher salt velocities in these tubes and consequently higher pressure drops. For the air pressure drop, there is a much larger percent difference between the 2-D and 3-D models. The 3-D model calculates a higher pressure drop in both the HP and LP CTAH. The percent difference for the HP CTAH is 31.5% and for the LP CTAH is 32.6%. One of the likely reasons that the 3-D model is higher is because of the friction loss in the bundle center, or the air "manifold." The total pressure for the salt in the tubes is so large that any friction loss in the salt manifolds will be negligible in comparison. However, for the air flowing through the tube bundle, the pressure loss is much smaller so the friction loss in both the HP and LP CTAH air "manifolds" is much more significant in comparison. Similar to the air outlet temperatures, Figure 2-21 gives the minimum, mean, and maximum air pressure drop for both the LP and HP CTAH to show the azimuthal variation at each vertical position. Also, there is a small spike in the pressure drop near the bottom of the tube bundle. This corresponds to the higher air temperatures and consequently higher air densities at these positions. The higher air density will give higher pressure drops. For the LP CTAH, this spike is not as significant

because the lower pressures lead to higher air velocities that correspond to significantly higher pressure drops. The vertical distribution dwarfs this small spike.

As mentioned earlier, it is important to have the temperature and pressure distributions in order to design the pressure vessel around the bundle, to correctly size the primary pump for the flibe coolant, and to calculate the circulation power loss of the RACC. It is also important to have the 3-D model to give a more accurate and complete effectiveness calculation in order to design the CTGH for the given application.

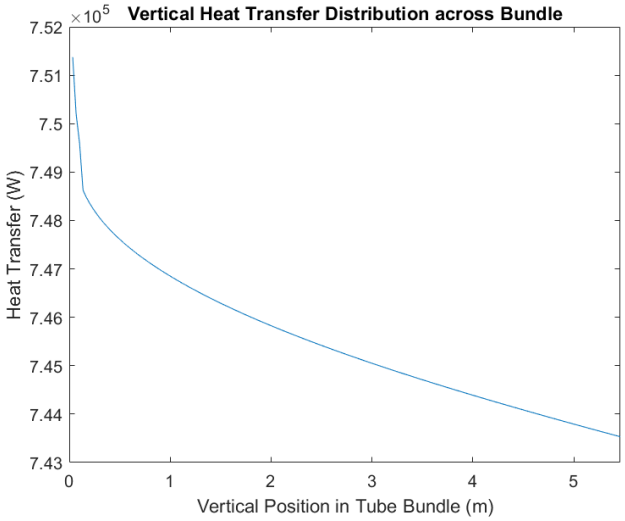

Figure 2-17. Vertical Heat Transfer Distribution in CTAH

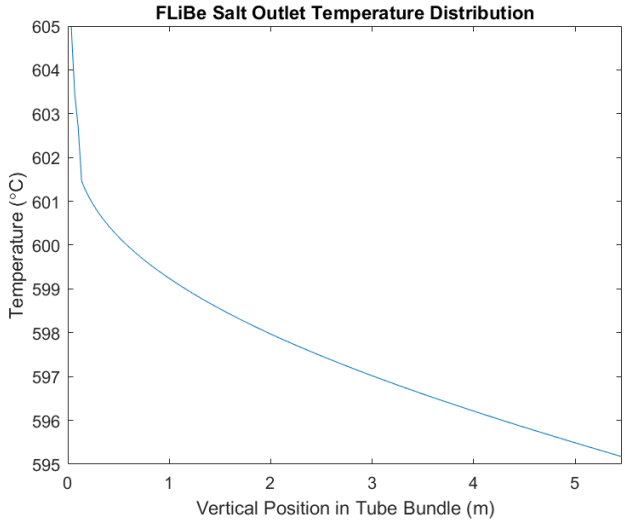

Figure 2-18. Vertical Distribution of Mean Flibe Temperature in CTAH Outlet Manifold

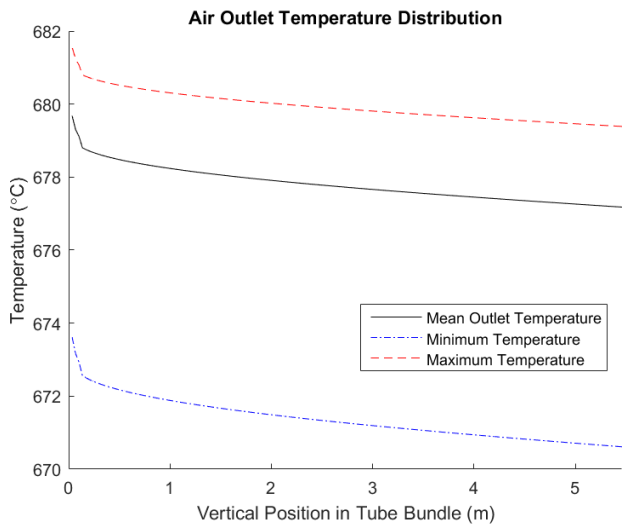

Figure 2-19. Vertical Distribution of Air Temperatures in CTAH Outer Annulus

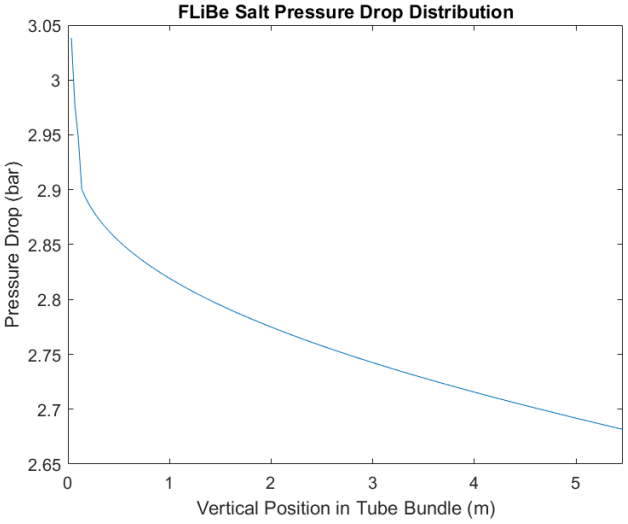

Figure 2-20. Vertical Distribution of Mean Flibe Pressure Loss in CTAH

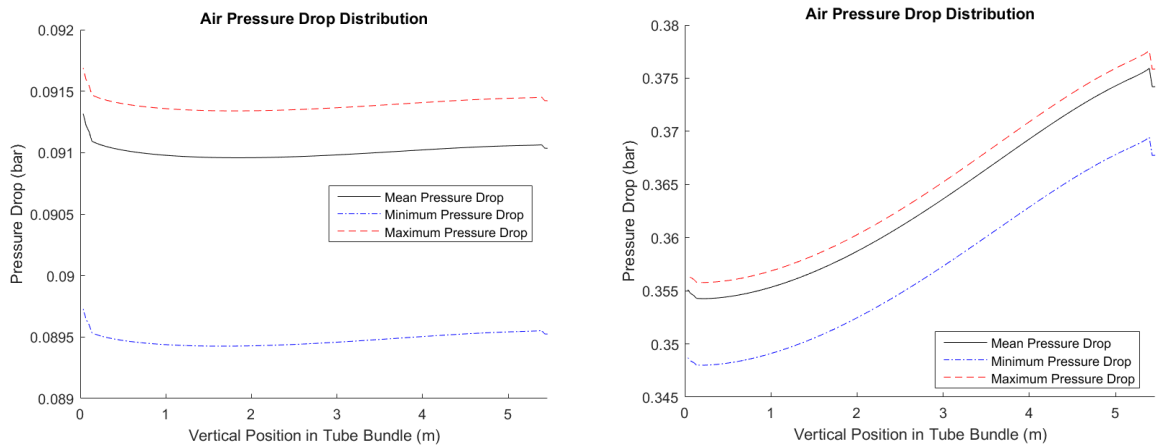

Figure 2-21. Vertical Distribution of Air Pressure Loss in HP CTAH (left) and LP CTAH (right)

2.5 Additional Code Features

THEEM was designed to model the heat transfer and flow through the CTGH under nominal conditions. However, certain modifications can be made to THEEM to account for special conditions and certain design changes. These changes and design issues will require further research. However, THEEM was designed so that it could be used to model these phenomena or it could account for how these changes affected the CTGH design. This section covers how THEEM can handle these special cases in the future.

2.5.1 Anti-Vibration Rod and Spacer Bar Implementation

The shell side of the CTGH involves gas flowing through the tube bundle. At high flow rates and high pressures, mechanical vibrations of the tubes can become a significant problem. For example, the spacing between the tubes in the FHR is on the order of a couple of millimeters. Large mechanical vibrations can cause tube fretting over the lifetime of the CTGH, leading to tube failure and shortening the life of the heat exchanger. It is also possible that it can affect the gas flow distribution through the bundle and create larger flow maldistributions across the tube bundle, reducing the effectiveness.

Païdoussis [40] lists the most common vibration excitation mechanisms for tubes in crossflow, which include: i) response to non-resonant turbulent buffeting, (ii) synchronization with the flow periodicity, which is often referred to as vortex induced vibration, and (iii) fluid-elastic instability. Non-resonant buffeting is characterized by a fluctuating pressure field around the tube bundle which can lead to excitation of the turbulent flow. Generally, this mechanism occurs at lower flow velocities and the amplitude levels caused by it are relatively small, so this mechanism is usually not worrisome. Vortex induced vibrations are generally caused when the frequency of the vortices shedding produced by flow over the tube matches the natural frequency of the tubes. Fluid-elastic instability occurs at significantly high flow velocities and is a self-excited vibration phenomenon. This mechanism is a significant problem because it sharply increases the vibration amplitude of the tubes and causes large structure deflection which can have a catastrophic effect on the tubes over a short period of time. Therefore, it is important to keep the flow below the critical flow velocity for the onset of fluid-elastic instability. Connors [41] gives the following formula to estimate the critical flow velocity:

$$U_{crit} = K f_n D_{out} \left(\frac{m_t \delta}{\rho_g {D_{out}}^2} \right)^{\frac{1}{2}} \quad 2\text{-}52$$

In this model, K is a constant dependent on the geometry of the tube bundle, f_n is the natural frequency of the tube, m_t is the mass of the tube, and δ is the logarithmic decrement for the tube vibrating in the *n*th mode.

Both vortex-induced vibrations and fluid-elastic instability are dependent on the natural frequency of the tubes. One of the simplest ways to minimize tube vibrations for either one of these mechanisms is to change the tubes' natural frequency. Treating each tube as a simply supported beam, Equation 2-53 gives the formula of natural frequency of each tube.

$$f_n = \frac{K_n}{2\pi L^2} \sqrt{\frac{EI}{m_t}} \quad 2\text{-}53$$

In this equation, K_n is a constant dependent on the mode of vibration, E is the modulus of elasticity of the tube, I is the area moment of inertia for the tube, and L is the tube span length. The simplest way to increase the natural frequency of the tubes is to decrease the span length of the tube. The CTGH design already has tube holders around the bundle that support the tubes. Increasing the number of these holders is one method of reducing the tube span lengths. Another method is to insert simpler anti-vibration rods. Future research and experiments will determine the number of tube holders and anti-vibration rods necessary to prevent flow-induced vibrations. THEEM can even be used as tool to determine the flow rates at various points around the tube bundle. However, the holders and anti-vibration rods will affect the flow through the tube bundle by restricting flow in the azimuthal direction. For the sake of simplicity, THEEM treats the anti-vibration rods as tube holders by stopping the gas from penetrating the holders or anti-vibration rods. Since the number of holders and anti-vibration rods need to be determined in the future, THEEM leaves this as a variable in the input file.

2.5.2 Thermal Effects of Tritium Diffusion Barrier

Due to the lithium in the flibe coolant, tritium production and release to the environment is a major concern in the Mk1 PB-FHR design. There are various components added to the FHR design to absorb tritium in the flibe salt before it reaches the CTAHs. However, since the CTAHs connect the primary loop of the FHR directly with an open-air Brayton cycle, tritium diffusion through the stainless-steel tubing and air could release tritium concentrations to the environment above the NRC limit. One solution for the Mk1 CTAH design is to coat the tubes in an aluminum oxide layer, Al_2O_3 [8]. Nuclear fusion experiments have demonstrated that coatings of aluminum oxide have been particularly effective at reducing tritium permeation by factors of 1,000 to 100,000 [42]. Further research will be performed to perfect application of the coating to the tubes and to study if the coating can handle the high temperature and thermal stresses of the CTAH environment. This research will examine if aluminum oxide is an effective choice for coating material and how thick this coating should be. From the perspective of heat transfer, the coating will have a different thermal conductivity from the stainless steel and will add an extra thermal resistance term. The coating will likely be too thin to have a significant effect on the heat transfer, and there is only a small difference in the thermal conductivity of aluminum oxide ($k_{Al2O3} = 8.79 \ \frac{W}{m*K}$) and 316 stainless steel ($k_{316SS} = 13.4 \ \frac{W}{m*K}$) at the

expected CTAH temperatures [43]. However, THEEM can still account for the small change by adding the aluminum oxide thermal resistance term in Equation 2-54 to the other thermal resistances in Equation 2-8.

$$R_{Al2O3} = ln\left(\frac{D_o + 2t_{Al2O3}}{D_o}\right) * \frac{1}{N_t * 2 * \pi * k_{Al2O3} * L} \quad 2\text{-}54$$

The user will specify the coating material and appropriate thermal conductivity, k_{Al2O3}, and the thickness of the coating, t_{Al2O3}. This coating is specific to the FHR design, but other designs may require similar coatings for multiple reasons, so THEEM can model them as well. Since this coating will likely be so thin that its effect on the tube outer diameter size will be negligible, the shell-side calculations will use the tube's original outer diameter for THEEM's gas calculations.

2.5.3 Tube Fouling Effects

Since the CTGH will be operating at high temperatures over its lifetime with molten salt or other coolants, tube fouling will pose a challenge for continued operation. Tube fouling is the deposition of undesired material on either the inner or outer surface of the tubes. Fouling increases the tubes overall thermal resistance, which in turns reduces the effectiveness of the heat exchanger. It also reduces the flow area inside the tubes and through the tube banks, which can lead to larger pressure losses over the lifetime of the heat exchanger. Fouling can also accelerate the rate of corrosion of the tubing material. The rate of tube fouling is a function of the chemistry of each fluid and its interaction with the tubing material at the elevated temperatures. Future studies will measure the rate of tube fouling for a particular coolant, such as flibe, and what material properties these deposits have, such as thermal conductivity. THEEM can be modified to use this data to account for the material deposition. First, THEEM will need to account for thickness of the material deposition layer on either inside or outside the tube. Then, THEEM will find the added thermal resistance of this layer. For any tube external fouling, it will use Equation 2-54 with the appropriate thickness and thermal conductivity values. For any tube internal fouling, it will use Equation 2-55 to find the added thermal resistance. THEEM will finally modify the tube internal and external diameters appropriately to account for tube fouling for the heat transfer and pressure drop calculations.

$$R_{Al2O3} = ln\left(\frac{D_i}{D_i - 2t_{deposit}}\right) * \frac{1}{N_t * 2 * \pi * k_{deposit} * L} \quad 2\text{-}55$$

Chapter 3.
CTGH Experiments

In order to use THEEM for actual CTGH design, it needed to be validated experimentally in a laboratory setting. This required a small CTGH sub-bundle operating at much lower temperature and pressures than the FHR CTAHs. Two different experimental setups were used to take measurements to validate THEEM. The original CTGH experiment was fabricated as a proof of concept design. The bundle was coiled by hand in the lab by students and could be used for some simple experiments, but it was not built with the intention of code validation. After performing experiments on the original CTGH experiment, a second bundle was fabricated using professional manufacturing techniques. This bundle was used in the more sophisticated Coiled-tube Air-heater Separate Effects Test, or CASET. This setup was designed for THEEM code validation, but it was also possible to perform various other experiments to study other phenomena with CTGH sub-bundles.

3.1 Original CTGH Experiment

A mock-up of a CTGH sub-bundle, as shown in Figure 3-1 was previously fabricated to experimentally measure the effectiveness and pressure drops across the sub-bundle. This bundle was fabricated out of 40 stainless steel tubes in a thin acrylic vessel. It was designed with 2 liquid manifolds with each tube looping around the bundle 4 times. To simplify fabrication, it was designed without any tie rod gaps or tube sloping for drainage. The CTGH bundle geometrical parameters are given in Table 3-1.

Figure 3-1. Original CTGH Experiment Sub-bundle

Table 3-1. Original CTGH Experiment Bundle Geometry

Tube Outer Diameter	0.635 cm (0.25 in)
Tube Wall Thickness	0.0508 cm (.02 in)
Longitudinal Pitch-to-Diameter Ratio (S_L)	1.37
Transverse Pitch-to-Diameter Ratio (S_T)	1.67
Number of Liquid Manifolds	2
Number of Loops	4
Number of Tubes per Layer per Manifold	1
Number of Tube Layers per Sub-bundle	20
Number of Sub-bundles	1
Number of Tie Rod Gaps	0
Number of Tube Holders	6
Annulus Inner Radius	22.23 cm
Tube Slope	0

After the initial fabrication of the tube bundle and vessel, the full experiment was constructed in multiple phases by several people, and consequently, there was not an initial design basis for this experiment. This setup was designed so that the fan would be at the bottom of the experiment and would pull air through the experiment. The air would enter the top of the bundle via the hole in the center of vessel and then flow out radially through the tube bundle before exiting out the bottom of the vessel. For the liquid side of the experiment, the pipes feeding the tube bundle were made from clear PVC, which limited the choice of heat transfer liquid to water. The water entered the outer manifolds, which connected to the stainless-steel tubes via flexible plastic tubing around the outer diameter of the bundle. More flexible tubes connected to the bundle tube outlets around the inside diameter of the tube bundle. These flexible tubes then dumped the water in an open-air plastic tub of water. This tub had a pipe penetration at the bottom which fed a pump that would circulate the water through a water heater before it flowed back to the liquid inlet manifolds. The original experiment used the following equipment for the experiment:

- ¼ HP Single Phase Centrifugal Water Pump
- 9.5 kW Electric Tankless Water Heater
- 0.16 HP Axial Fan with a maximum air flowrate of 1500 CFM

The final addition to the original setup was a flow straightener at the fan outlet. The full setup along with this flow straightener is shown in Figure 3-2. Initially, the easiest way to measure the air's flowrate was to measure the velocity at the outlet of the fan as the fan had a constant cross section with no obstructions. However, initial velocity measurements showed a large variance in air velocity across the fan outlet. As seen in Figure 3-2, the air duct has a 90-degree bend right before the fan. This turn along with the fan likely caused eddies and turbulence in the air. To obtain more consistent measurement at the fan outlet, a flow straightener was installed. The flow straightener consisted of a long tube that was 3 tube diameters in length with a honeycomb screen at the outlet. The extra length would allow for the air to have a more fully developed flow profile at the outlet, and the honeycomb screen would reduce the eddies. Baker [44] states that 60 diameters is often quoted as the minimum length in order for the flow profile to fully develop; however, this length is often unrealistic. For example,

this experiment has a 14-inch diameter pipe which would require a minimum pipe length of 70 feet. A shortened pipe combined with a flow straightener screen should still reduce the swirls and give a partially developed flow. Since this flow was being measured to estimate the overall air mass flowrate, this straightener was sufficient to reduce swirls for flow measurements. After installing the straightener, the air flow rate measurements were much more consistent.

Figure 3-2. Full setup for Original CTGH Experiment

The inlet and outlet temperatures for both the water and the air were measured using Type-T thermocouples. A thermocouple was installed in one of the inlet manifolds, and a second thermocouple was placed in the open-air tub to measure the water inlet and outlet temperatures, respectively. The air inlet temperature was taken to be the ambient air temperature in the lab. The outlet air temperature was taken at probe holes that were drilled in the plastic vessel around the tube bundle so that the outlet air temperature could be measured at different points around the bundle. The water pressure drop was measured using water manometer lines, and the air pressure drop was measured at the different probe holes using a U-tube manometer filled with water.

For model validation, the pump, fan, and heater were all run at full power until the bundle reached steady-state heat transfer. This was monitored by the water inlet and outlet temperatures. Once the system reached steady-state, the bundle had the inlet parameters shown in Table 3-2.

Table 3-2. Original CTGH Bundle Inlet Parameters

Inlet Parameter	Water	Air
Temperature	49.9±0.1°C	21.7±0.2°C
Pressure	~1.5 bar	1.01 bar (~1 atm.)
Mass Flow Rate	0.184 ± 0.016 kg/s	0.329±0.023 kg/s

Using the inlet parameters from Table 3-2 and the geometry in Table 3-1, THEEM was used to model the experiment. The measured results of the experiment are compared with the THEEM results in Table 3-3.

Table 3-3. Original CTGH Experimental Results

	Experimental Measurements	**THEEM Value**	**Percent Error**
Water Temperature Drop	6.0±1.0°C	9.1°C	34.10%
Bulk Air Temperature Rise	21.6±1.0°C	21.0°C	1.9%
Water Pressure Drop	0.0243±0.0006 bar	0.0173 bar	40.46%
Bulk Air Pressure Drop	0.0004±0.0002 bar	0.0013 bar	69.23%

For this experiment, THEEM appeared to have only predicted the air temperature rise accurately. It was expected that if the air temperature was predicted accurately, then THEEM would also accurately predict the water temperature since the temperatures are found using the same set of equations. However, the air temperature drop listed in Table 3-3 is the simple arithmetic mean of all temperature measurements around the outer diameter of the tube bundle. THEEM predicted that these temperatures would range between 41.0°C to 42.9°C. The actual measurements ranged from 34.7°C to 47.6°C. Therefore, THEEM's air temperature predictions do not match the experimentally measured air temperatures. In addition, THEEM's pressure drop predictions for both water and air did not match the experimental results.

The large range of air outlet temperatures indicated that there was large flow maldistribution across the bundle, which THEEM did not account for. The flow maldistribution is likely due to the fabrication method of the tube bundle. These tubes were coiled by hand using tube holders to approximate the shape. Visual inspection of the bundle shows that many tubes either overlap or come into contact with other tubes. This will reduce or block flow through sections of the bundle, which will change the heat transfer distribution in the bundle, resulting in a change in both the air and water temperatures. The flow maldistribution might also account for the difference in the air pressure drop measurements between THEEM and the experiment. With different flow through the bundle, the pressure gradient in the tube bundle is also likely to be different from the ideal geometry modeled in THEEM. As for the water pressure loss in the tubes, the source of error is possibly due to bubbles in the line. Since the water was open to the air once it exited the bundle, air was easily trapped in the lines during the experiment. This was confirmed by visual inspection of the experiment. These bubbles could cause inaccurate manometer readings, which might account for the difference in the pressure drop measurements.

The results of this experiment did not validate the THEEM model. In fact, the results indicated a better tube bundle and experimental setup needed to be constructed to validate THEEM. The bundle needed to be professionally manufactured in order to reduce airflow maldistribution. The tubes also needed to be connected to manifolds like they would in a large scale CTGH instead of using flexible tubing. For the other components in the setup, the fan and pump speeds were each limited to one speed that could not easily be adjusted. In addition, the new setup would need to have a more powerful fan and a more powerful pump that could reach

higher flowrates. An additional improvement to the setup would be easily adjustable speeds so that multiple experiments could be performed under various conditions. The new setup needed improved instrumentation than this experiment, which included using more thermocouples placed closer to the inlet and outlet of the bundle itself. Finally, this experiment would be designed to minimize air leaking through the vessel and through the probe holes. With all these requirements in mind, a second CTGH experiment was fabricated.

3.2 CASET Experiments

3.2.1 Experimental Design and Fabrication

3.2.1.1 Tube Bundle Design

In order to fabricate CASET, it was necessary to design and construct a CTGH tube bundle, to decide on the working fluids and flow conditions to be used for the experiment, and, finally, to build an experimental apparatus around the bundle in order to deliver these conditions and take measurements. The most important part of the CASET's construction was the fabrication of the tube bundle. This bundle would be designed based on the Mk1 PB-FHR CTAH. The Mk1 design uses ¼" (0.635 cm) OD 316 stainless steel tubing with wall thickness 0.035" (0.0889 cm). This tubing material was chosen due to its low cost and corrosion resistance to the molten salt flibe coolant [8], [45]. As with the original CTGH experiment, stainless steel was used as the tubing material for CASET due to its corrosion resistance and relative low cost. The same diameter tubing with a thinner wall was selected to further reduce costs.

In the Mk1 PB-FHR's CTAH, the tubes are arranged in a staggered pattern with fixed pitch-to-diameter ratios in the horizonal and vertical directions. The bundle was designed to match these same ratios, S_L and S_T, as close as possible. Originally, the tube bundle was planned to be sloped for drainage like the FHR design. However, it would be difficult and expensive to fabricate the tube holders that kept this sloped pattern and to construct the vessel around this sloped bundle. It would be difficult for the vessel to fit the shape of the sloped bundle so that there was not bypass flow around the bundle. Having sloped tubes would show experimentally how well the CTGH could drain the coolant in the tubes, but it is difficult to scale how different fluids drain. It is unlikely that the heat transfer fluid used in CASET would have the same viscosity as the molten salt flibe or any other coolant used in the CTGH. The extra cost and difficulty of fabricating a sloped tube bundle did not appear to be justified, therefore the tube bundle design was changed to a flat design.

Since the tube bundle was designed to be flat, the tube holders could simply be flat aluminum bars with holes machined in them for the tubes stacked on top of each other. The thinnest aluminum bars available without further machining were 3/16" (0.47625 cm) thick. The Mk1 PB-FHR CTAH design uses pitch-to-design ratios of S_L=1.256 and S_T=1.45. CASET was designed to try and match these ratios; however, due to the size of the aluminum bars, the pitch-to-design ratios became of S_L=1.256 and S_T=1.50. A fabricated tube holder can be seen in Figure 3-3. Next, in order for the experiment to have a more manageable bundle size, it was designed with only 2 liquid manifolds instead of 4. In order to use fewer tubes, each manifold would have 10 staggered rows with 2 tubes per row. This manifold layout is shown in Figure 3-4 along with the direction of flow through the tube bundles. These tubes looped 3 times before reaching the inner manifolds. Finally, the tube bundle's inside annulus diameter was chosen as 50 cm in order to minimize the size of the bundle. The tube bundle design geometry is summed up in Table 3-4.

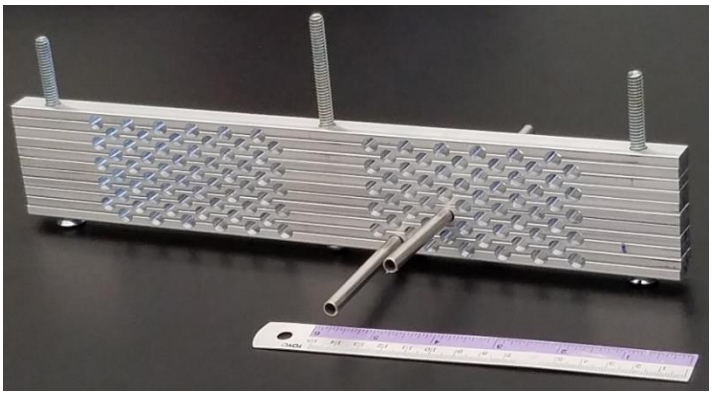

Figure 3-3. CASET Tube Holders

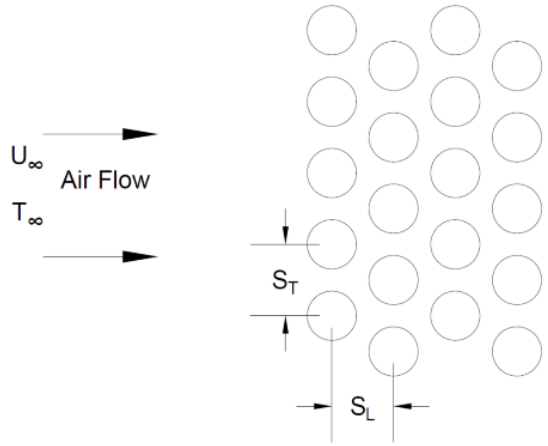

Figure 3-4. CASET Tube Layout with Air Flow

Table 3-4. CASET Tube Bundle Design Geometry

Tube Outer Diameter	0.635 cm (0.25 in)
Tube Wall Thickness	0.0508 cm (.02 in)
Longitudinal Pitch-to-Diameter Ratio (S_L)	1.256
Transverse Pitch-to-Diameter Ratio (S_T)	1.50
Number of Liquid Manifolds	2
Number of Loops	3
Number of Tubes per Layer per Manifold	2
Number of Tube Layers per Sub-bundle	10
Number of Sub-bundles	1
Number of Tie Rod Gaps	1
Width of Tie Rod Gaps	3.80 cm
Number of Tube Holders	8
Annulus Inner Radius	25 cm
Tube Slope	0

3.2.1.2 Tube Bundle Fabrication

One of the most important aspects of this experiment was the fabrication of the tube bundle. This fabrication method would need to be more precise than the fabrication method for

the original tube bundle in order to reduce flow maldistribution through the tube bundle. In addition, using a professional metal fabricator would help in the selection of a fabrication method that could be used to fabricate the CTGH tube bundles for larger applications, such as the FHR. This tube bundle was fabricated using a die attached to a mandrel. The tube was fed onto the die, which spun slowly around the mandrel forming a coiled shape, as shown in Figure 3-5. When the tube is removed from the die, the coils tended to expand due to the elasticity of the steel. So, in order to obtain the more precise shape of the tube bundle, the tube is laid on top of a 1:1 drawing of the tube and is shaped by hand until the tube has the correct coil shape, which is also shown in Figure 3-5.

Figure 3-5. Bundle Fabrication: (Left) Tube Coil Die on Mandrel; (Right) Shaped by Hand to Match Drawing

Once the tubes were coiled to the desired shapes, the bundle was then assembled in layers using the machined aluminum tube holders. After all the tube layers were assembled in the tube bundle, the inner and outer manifolds were attached to the bundle. The manifolds consisted of a stainless-steel tube sheet bolted to an aluminum body with a clear polycarbonate window to view the liquid inside the manifold during experiments. The method for connecting the tubes to the tube-sheet for the manifold is an ongoing challenge for the CTGH design in general. This connection appears to be the weak point structurally in the tube bundle, especially when the bundle is in a high pressure and high stress environment as is expected for the FHR CTAH and for the sodium to supercritical CO_2 CTGHs. Under these conditions, thermal shock and creep deformation can become an issue. Proposed methods of tube-to-tube sheet connections include different methods of diffusion bonding , including simple diffusion bonding, tube expansion followed by diffusion bonding, and hybrid friction diffusion bonding [23], [24]. Further material analysis and creep deformation studies of different tube-to-tube sheet connections will need to be done to determine the best bonding method. However, for this experiment, the temperatures and pressures were too low for creep deformation to be a major concern. So, the tubes were simply inserted in the tube sheet and TIG welded to the sheet. Unfortunately, this method created multiple leaks at the welds that needed to be sealed with silicone sealant, indicating that this method would not be practical for nuclear applications. The completed tube bundle is shown in Figure 3-6.

Figure 3-6. CASET Fabricated Tube Bundle

3.2.1.3 Heat Transfer Fluid Selection

Once the tube bundle was designed and fabricated, the next step was to determine the working fluids and the flow conditions. In order to simplify the experimental design and make it safer, the working fluid for the gas would be the air in the lab space around the experiment. The air is at room temperature and atmospheric pressure. In the design for the FHR CTAH, the inlet air is 418.6°C and either 18.76 bar or 4.99 bar [10], [11]. For the liquid, there was the possibility of using water or the heat transfer oil Penreco Drakesol 260 AT Mineral Oil. Drakesol 260 AT matches the Prandtl number of the molten salt flibe at the FHR temperatures of 600-700°C at relatively low temperatures of 60-140°C, which can be reached safely in a laboratory setting [46]. This oil was considered because it had been used in other separate effect tests for studying different components of the FHR [47]. Drakesol 260 AT was used often because it would allow for experiments to have dynamic similitude with the Mk1 PB-FHR design. In these heat transfer experiments, it would match the Prandtl number and the flow could be adjusted until it matched the Reynolds numbers in the FHR and, therefore, approximated the Nusselt numbers in the FHR CTAHs. However, the oil can be corrosive to the plastics that are used for piping and heaters. Then, even though 60-140°C is much lower than the flibe temperatures in the FHR, those temperatures are still high enough to pose a risk of burns. In order to reduce the cost of the piping materials and to operate at lower temperatures for lab safety, water was selected as the liquid for the experiment. In order to keep the water single phase and to stay within the limitations for water heaters on the market, the water would not be heated above 80°C.

3.2.1.4 CASET Experiment Design & Construction

After selecting the working fluids, the next step was to design the vessel and ductwork to guide air through the tube bundle. The vessel around the bundle was made of acrylic to reduce

cost and weight of the vessel. Also, using a transparent material allowed visual inspection of the bundle during experiments. Ductwork was connected around the acrylic vessel so that air could enter from the top of the bundle, flow through the tube bundle, and then exit out the bottom of the vessel. In order to easily take flowrate measurements, the inlet of the bundle starts as a chimney. This reduces the turbulence and eddies in the air before it enters the tube bundle. It also allowed for easy measurement of the air flowrate entering the bundle since there is little turbulence and a known flow area. Therefore, airflow measurements did not pose a challenge in CASET like it did in the original experiment. It was then necessary to determine the Reynolds number in order to select a fan for this application. Using THEEM, it was found that the air in the FHR CTAHs had Reynolds numbers between 3700 and 8500. Based on these Reynolds numbers and the geometry of the tube bundle, a flowrate was calculated. With this flowrate, the estimated head loss across the tube bundle calculated by THEEM, and the estimated head loss across the ducting, it was possible to find a fan that met these requirements. A 5 hp squirrel cage fan was selected to pull air through the system.

Figure 3-7. CASET Complete Experimental Setup

Once the ducting was finished, the water loop was designed. The first step was heating the water. Based on the existing electrical components in the lab space, a 16.6 kW tankless electric water heater was selected. This meant the maximum heat transfer of the CTGH would be 16.6 kW because at steady state the bundle could not remove more heat than the heater put into the system. It seemed likely the heat transfer would be less since there would be some parasitic heat loss via the pipes between the tube bundle and the heater. This heater also was designed to shutoff if the water reached 80°C, so the pipes, seals, and measuring devices needed to be capable of operating up to 80°C. In order to reduce cost, to simplify pipe construction, and to minimize contamination from pipe corrosion, plastic pipes were used instead of steel or copper pipes. To operate up to 80°C, CPVC was chosen as the pipe material. According to ASTM standards, CPVC can be used safely for water systems up to 180°F, or 82°C, which makes it ideal for CASET [48]. Manometer lines, thermocouples, and rotameters were installed

at key points in the loop in order to take necessary measurements for the experiment. Once the piping was designed, the flowrate was calculated. Similar to the air calculations, the flowrate was based on matching CASET's liquid Reynolds numbers to the FHR Reynolds numbers. According to the THEEM results for the FHR from the previous chapter, the molten salt flibe Reynolds numbers are between 1000 and 1800. Based on these Reynolds number and the tube geometry, the water flowrate was calculated. Following the flowrate calculation, a ¾ HP centrifugal water pump was selected using the estimated head loss throughout the loop and using the calculated flowrate. A head tank was added to increase the total head of the water in the system. Figure 3-7 shows the completed CASET experiment. Figure 3-8 shows an overhead view of the tube bundle in the completed CASET and maps the number locations of the probe holes.

Finally, in order to prepare the experiment, it was necessary to calculate the nominal temperatures and flowrates of the experiment. The flowrates, $\dot{m}$, were already calculated to size the pump and fan. For the air inlet temperature and pressure, it was assumed to be room temperature air at atmospheric pressure. It should be noted that the lab where this experiment was performed was large and well ventilated enough so that the hot air exhaust from the experiment likely had little effect on the overall room temperature. For the water inlet, the pressure would be close to atmospheric. The maximum water temperature was 80°C; however, it was unlikely that the water at the bundle inlet would reach that temperature. It was assumed that some heat would be lost to the surroundings while flowing in the pipes between the heater and the tube bundle. So, to be conservative, the water inlet was assumed to be around 70°C. Assuming the CTGH would have the maximum heat transfer, Q, of 16.6 kW, the outlet temperatures for the air and water were found using Equation 3-1. The nominal values of the flowrates, inlet and outlet temperatures, and inlet pressures are given in Table 3-5.

$$Q = \dot{m} C_p \Delta T \qquad 3\text{-}1$$

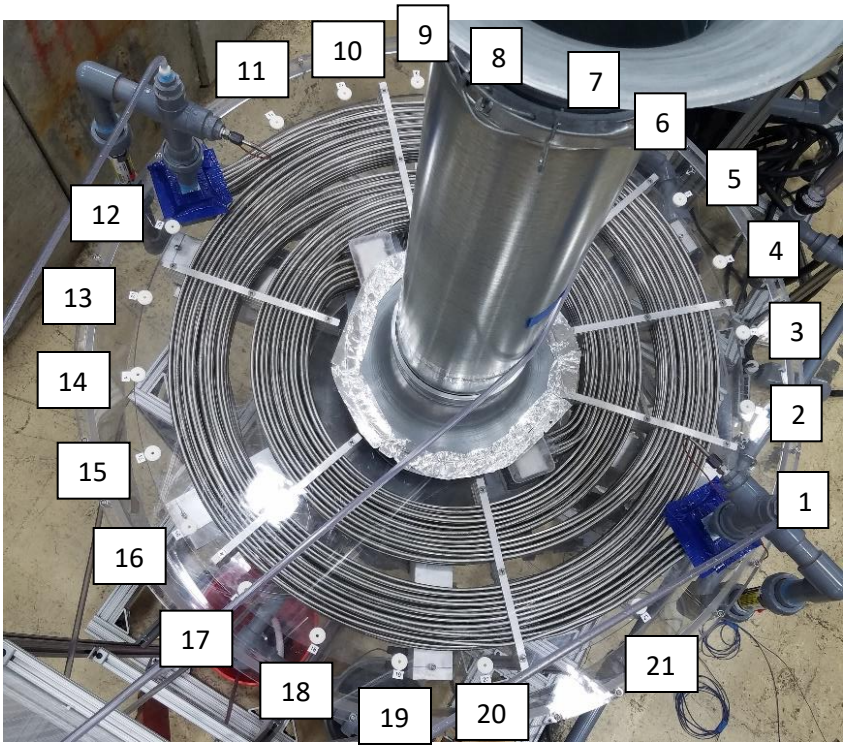

Figure 3-8. Overhead View of CASET Tube Bundle

Table 3-5. Nominal Values for CASET Experiment

Air Flowrate	0.649 kg/s
Air Inlet Pressure	1.01 bar
Air Inlet Temperature	25.0°C
Air Outlet Temperature	51.0°C
Water Flowrate	0.100 kg/s
Water Inlet Temperature	70.0°C
Water Outlet Temperature	20.0°C
CTGH Heat Transfer	16.6 kW

3.2.2 Description of CASET Experiments

As mentioned earlier in this chapter, CASET was constructed to provide data to validate the THEEM code. However, it was possible to perform other experiments and measurements. This section describes each of the experiments that were performed using CASET.

3.2.2.1 THEEM Validation

The primary purpose of CASET was to generate experimental data to validate the THEEM code. This was done by performing an experiment that THEEM could model, taking relevant experimental measurements, and comparing the THEEM results with the experimentally measured results, similar to the original CTGH experiment. Specifically, it was necessary to measure the flowrates, the pressure drops across the tube bundle, and the inlet and outlet temperatures of both the air and water. The pump and fan speeds were controlled by a variable frequency drive (VFD), so the flowrates could be decreased if necessary. This allowed for measurements under different flow conditions.

For the tube-side measurements, the water flowrate was measured using a rotameter (Dwyer UV-1112) installed in the water loop just before the heater with an experimental uncertainty of ± 0.5 gpm, or ± 0.031 kg/s at 70°C. The water temperatures were measured using Type-T thermocouples (Omega # TMTSS-020U-3) installed in the inlet and outlet manifolds of the tube bundle with a manufacturer defined uncertainty of ± 1.0°C. The pressure drop was measured using manometer lines connected to the same manifolds. These lines were attached to a manometer board with grid tape for measuring the height difference between the inlet and outlet manometer lines with an uncertainty of ± 0.5 mm. This height difference was then converted to the pressure drop with an uncertainty of ± 0.00005 bar at 25°C.

Figure 3-9. Schematic Diagram of Simple Pitot Tube (Left) & Pitot-Static Tube (Right)

For the shell-side measurements, the air flowrate was measured using a pitot-static tube inserted into the vertical air inlet duct through a hole that can be seen in Figure 3-7. The pitot-static tube was connected to a U-tube manometer in order to measure difference between the

total and static pressure of the air in the duct. This height difference, which had an uncertainty of ± 1 mm was used to find the average velocity of the air. The tube was inserted at different depths in order to measure velocities across the duct profile. Then, assuming the duct flow profile had not fully developed because the duct was too short, the average velocity was calculated. The velocity was converted to the mass flowrate using the cross-sectional area of the duct and the density of the air, which also gave an uncertainty of ± 0.000098 bar at 25°C. The air inlet temperature, which was essentially the ambient room temperature, was measured with a Type-T thermocouple near the inlet of CASET. The air outlet temperature was found by taking measurements at 21 different points along the outer diameter of the tube bundle. These probe holes can be seen in Figure 3-8. In order to prevent the air from mixing with the cooler ambient air, a thermocouple was fitted with a plug so that it would seal the probe hole while measuring the temperature. For the air pressure drop, a simple pitot tube was connected to one end of the U-tube manometer. The other end of the U-tube manometer was left opened to the ambient air. For clarity, schematic diagrams are given in Figure 3-9 to show the difference between a simple pitot tube and a pitot-static tube. The simple pitot tube was inserted into each probe hole in order to measure the total pressure difference between the ambient air and the bundle outlet air. However, this measured the pressure drop of the air between the vertical inlet duct entrance and the bundle outlet. The head loss from the air entering the inlet duct, flowing through the duct, and then making a 90-degree turn to flow through the tube bundle was found by taking simple pitot tube measurements at the inlet of the tube bundle. By taking into account this head loss, it was possible to isolate the head loss just across the tube bundle.

3.2.2.2 Airflow Distribution Measurements

Figure 3-10. Hot-Wire Anemometer Probe Measurement

The next experiment performed with CASET was measuring the airflow distribution across the tube bundle. The spacing between the tubes is on the order of a couple of millimeters, which meant there was little room for error. However, even though the bundle fabrication method was an improvement over the original experiment, it was too difficult to match these tight tolerances perfectly during the fabrication of this tube bundle. Therefore, the tube spacing was not consistent across the tube bundle, meaning that there was still some flow maldistribution. In order to measure the scale of airflow maldistribution, the blower was run while taking isothermal velocity measurements at each probe hole around the outer diameter of the tube bundle using a 2 wire hot-wire anemometer probe. The setup consisted of a Dantec

StreamLine 90N10 Frame with a 55P64 probe, and according to Dantec, under typical experimental conditions, the velocity's uncertainty is ± 3%. This probe could measure 2 components of the velocity at each point giving more data on the direction of the flow as it exits the bundle. The hot-wire probe was modified to hold a plug while taking measurements, as seen in Figure 3-10. Similar to the thermocouple, this plug sealed the hole so that the probe's measurement of the air leaving the tube bundle was not distorted by air flowing through the probe hole.

3.2.2.3 Wilson Plot Method

Originally developed by Wilson in 1915, the Wilson plot method is a technique to estimate the convection coefficients of the different heat transfer processes occurring within a heat exchanger. It is based on separating the overall thermal resistance of the heat exchanger into the thermal resistance of each component of the heat exchanger. For CASET, the overall thermal resistance was separated into the thermal resistances corresponding to the external convection through air, the conduction through the tube wall, and the internal convection through water. This method avoids directly measuring the surface temperatures of the tubes, where attaching temperature sensors to the tubes can consequently alter the flow of fluids and distort the temperature measurements. Using the Wilson plot method, it is possible to find the heat transfer coefficient based on the bulk fluid temperatures[16] [49].

As the methods for calculating the heat transfer coefficients have become more accurate, the Wilson plot method was modified as well. The Wilson plot method can be adapted to be used with different empirical correlations to find the convection coefficients of the different fluids in a heat exchanger. First, it was necessary to find the overall heat transfer coefficient, $(UA)_{ov}$, with Equation 3-2 based on the total heat transfer, Q_{tot}, and the overall log mean temperature difference, $LMTD$.

$$(UA)_{ov} = \frac{Q_{tot}}{LMTD} \qquad 3\text{-}2$$

The overall resistance is then written in terms of the shell, tube, and tube wall thermal resistances as shown in Equation 3-3. This equation shows the overall resistance in terms of the tube wall thermal resistance, R_w, the shell and tube convection heat transfer coefficients, h_s and h_t, and the shell and tube surface areas, A_s and A_t, respectively.

$$\frac{1}{(UA)_{ov}} = \frac{1}{h_s A_s} + \frac{1}{h_t A_t} + R_w \qquad 3\text{-}3$$

In order to find the convection heat transfer coefficients, it is necessary to use the definition of the Nusselt number (Nu), shown in Equation 3-4, and the empirical Nusselt number correlations for the air flowing through the tube bundle and the water flowing through the tube bundle.

[16] For the shell-side, the bulk fluid temperature for the air leaving the bundle is found by averaging the air outlet temperatures around the bundle since heat loss via conduction through the acrylic vessel would have made measurements downstream of the bundle less accurate.

$$Nu_s = \frac{h_s D_O}{k_s} \quad 3\text{-}4$$

For the shell-side, the air flowing through tube bundles can be modelled using the Zukauskas Nusselt correlation showing in Equation 3-5 [29]. Re is the Reynolds number and Pr is the Prandtl number of the gas. C_s and m are left as variables to be solved using the Wilson plot method.

$$Nu_s = C_s(Re^m Pr^{0.36})_s \quad 3\text{-}5$$

For the tube-side, the flow was designed to be laminar. In order to model the laminar flow through coiled tubes in THEEM, the Nusselt correlation developed by Manlapaz and Churchill was used since it could be used for all Dean numbers and a large range of Prandtl numbers [27]. Unfortunately, this formula was too complex to be used with the Wilson plot method. So, a Nusselt number correlation developed by Kalb and Seader [50] was used since it is also a function of Dean and Prandtl numbers. Equation 3-6 is a function of the Dean number, De, and the liquid Prandtl number, Pr_t. C_t and p are left as variables to be solved using the Wilson plot method.

$$Nu_t = C_t(De^p Pr^{0.2})_t \quad 3\text{-}6$$

Combining Equations 3-3 thru 3-6 gives the linear form of Equation 3-7 with unitless variables:

$$Y = b + nX \quad 3\text{-}7$$

where

$$Y = \left[\frac{1}{(UA)_{ov}} - R_w\right] * \left[\frac{k_s A_s}{D_O} * (Re^m Pr^{0.36})_s\right]$$

$$X = \frac{\frac{k_s A_s}{D_O} * (Re^m Pr^{0.36})_s}{\frac{k_t A_t}{D_i} * (De^p Pr^{0.2})_t}$$

$$n = \frac{1}{C_t}$$

$$b = \frac{1}{C_s}$$

Then, by taking the natural log of Equation 3-5, Equation 3-8 is obtained:

$$\ln\left(\frac{Nu_s}{Pr_s^{0.36}}\right) = \ln(C_s) + m * \ln(Re_s) \quad 3\text{-}8$$

Similarly, Equation 3-9 can be obtained by taking the natural log of Equation 3-6:

$$\ln\left(\frac{Nu_t}{Pr_t^{0.2}}\right) = \ln(C_t) + p * \ln(De_t) \quad 3\text{-}9$$

From Equations 3-7 thru 3-9, there 4 unknowns: m, p, C_s, and C_t. They can be solved by modifying an iterative process described by Jin et al. [51]:

1. Guess m and p.
2. Solve for C_t and C_s from Equation 3-7 by a linear regression of Y on X.
3. Solve for Nu_s from Equations 3-3 and 3-6 using the C_t in step 2.
4. Solve for C_s and m from Equation 3-8 by a linear regression of $\ln\left(\frac{Nu_s}{Pr_s^{0.36}}\right)$ on $\ln(Re_s)$ using the Nu_s in step 3.
5. Solve for Nu_t from Equations 3-3 and 3-5 using the C_s in step 2.
6. Solve for C_t and p from Equation 3-9 by a linear regression of $\ln\left(\frac{Nu_t}{Pr_t^{0.2}}\right)$ on $\ln(De_t)$ using the Nu_t in step 5.
7. Repeat steps 1–6 until m, C_s, p, and C_t converge.

3.2.2.4 Impulse Response Measurement

Nuclear reactors have a history of using frequency response testing to examine how changing certain parameters affect the system as a whole. For example, in some early research reactors, frequency response testing was used to study the change in power and coolant temperature by changing the control rod position, which varied the reactivity, or opening and closing coolant valves [52]. These tests were also used in experiments that modeled reactor behavior. For example, the Compact Integrals Effects Test (CIET) was developed to model the thermal hydraulics and safety systems of the Mk1 PB-FHR design in a laboratory setting. Using frequency response testing, it was possible to extract data that could be used to validate system models of the FHR and to predict FHR system behavior during a transient event, such as start-up, shutdown, or various accident scenarios [53].

CASET is a separate effects test that does not have as many components that can influence the system response. Therefore, frequency response tests were not a priority in its design. However, some basic testing could give some data about the CTGH that could be used in CIET and about how the CTGH would respond in a transient scenario. Due to the electrical system available, it was not possible to control the heater power. Control was limited to turning the heater power on or off. However, the heater was powered by two separate electrical breakers, so it could operate at full power or half power by keeping one of the breakers off. This meant that any frequency response test would just measure the impulse response of turning the heater on or off. The output variable that was used to measure the response was the water

temperatures at the inlet and outlet of the tube bundle since there were already thermocouples installed at these locations. The impulse response measurements consisted simply of switching the heater to either full or half power or off and measuring the temperature change over time.

The fan and pump were each powered by a VFD, allowing control over their speed. It would be possible to use them to recreate an accident scenario, such as a turbine trip without reactor SCRAM or a loss of forced circulation (LOFC) of the reactor coolant. This scenario would require the development of a control system for CASET, which was outside of the scope of this project. However, the control system can be developed in the later for future frequency response testing experiments on CASET. This means that these impulse response measurements set the groundwork for future frequency response testing experiments using CASET, which can be used to improve the overall FHR system model.

3.2.3 CASET Experimental Results & Discussion

3.2.3.1 THEEM Validation

Table 3-6 shows the flow rates and inlet temperatures recorded from the experiment that were inputted into THEEM. Table 3-7 compares the experimental measurements with the values predicted by THEEM. The bulk outlet air temperature rise was calculated using a weighted average of the local temperatures and the mass flow rate at each point. These mass flow rates were calculated based on the outlet radial velocities that were found using the data from the airflow distribution measurement, which are shown in Figure 3-12 and Figure 3-13.

Table 3-6. CASET Experimental Measurements

Parameter	Measurement
Air Flowrate [kg/s]	0.606 ± 0.156
Air Inlet Temperature [°C]	19.9 ± 1.0
Water Flowrate [kg/s]	0.136 ± 0.031
Water Inlet Temperature [°C]	67.9 ± 1.0

Table 3-7. Initial Validation Comparison with THEEM

Parameter	Experimental Measurements	THEEM Value	Percent Difference
Mean Water Temperature Drop	27.9 ± 1.0°C	32.0°C	12.81 %
Mean Water Pressure Drop	0.01538 ± 0.00005 bar	0.0099 bar	55.35 %
Bulk Air Temperature Rise	31.8 ± 1.0°C	29.8°C	6.71 %
Mean Air Pressure Drop	0.00764 ± 0.000098 bar	0.0211 bar	63.79%

The initial measurements indicated that there were some discrepancies between the THEEM calculations and the experimental measurements. There was approximately 5-10% error in predicting the temperature changes and approximately 60% error in predicting both pressure drops through the tube bundle. However, on closer analysis, an error in the setup was

discovered. Equation 3-1 was used to estimate the heat transfer on both the shell and tube side. Since the measurements were taken at the inlets and outlets, the heat lost by the water should equal the heat transferred to the air. The experiment is performed at steady-state, so the heat transfer in the tube bundle cannot be greater than the heat generated by the 16.6 kW water heater. Using the temperature changes in Table 3-7 and the mass flow rates from Table 3-6, it was found that Q_{air}=19.5 kW and Q_{water}=-15.9 kW. Since the heat transfer values are different and the calculation for the air implied that the air was heated more than the water heater could heat the system, this indicated that the local outlet temperature measurements for the air were not representative of the bulk air outlet temperature. The air outlet temperatures were measured at a single elevation around the outlet of the tube bundle, so they were not measurements of the temperature distribution exiting the full outlet face of the heat exchanger. However, the air flow rate was measured downstream of the tube bundle. It was likely that there was some bypass flow around the top and/or bottom of the tube bundle.

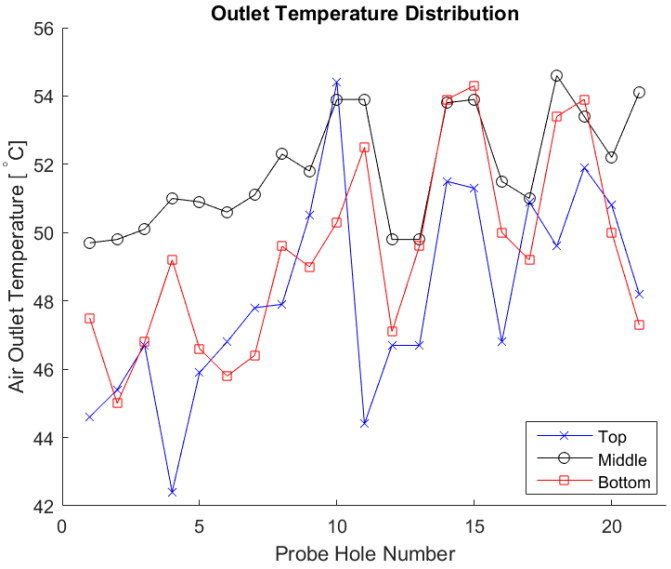

Figure 3-11. CASET Air Outlet Temperature Distribution

In order to confirm that there was bypass flow, another experiment was performed. In this experiment, the air outlet temperatures were measured at the top, middle, and bottom of the tube bundle at each probe hole. These temperatures are given in Figure 3-11. CASET was run at full power in order to match the results of the first experiment. This graph shows that the air exiting the center of the tube bundle was usually hotter than the air exiting near the top and bottom of the bundle. These cold spots at the top and the bottom implied that the air is not being heated as effectively as it is in the center if the tube bundle. This can be partially attributed to parasitic heat loss due to conduction through the top and bottom acrylic plates. However, the difference in temperature vertically at some points is too large to be attributed to simply conduction. It is likely that the air is not being heated properly at the top and bottom of the bundle due to bypass flow at these locations. It also appears that most of the bypass flow occurs at the top of the bundle from this graph. The temperatures at the bottom of the bundle do not vary as much from the center of the tube bundle temperatures, especially at probe holes 13 through 19. The large variance in temperatures at the top of the bundle also imply some flow mixing from flow maldistribution. Both the flow maldistribution and the bypass flow around the bundle mean that the flowrate through the center elevation of the tube bundle would be reduced

and the outlet temperature at the mid-elevation was higher than the actual bulk outlet temperature, giving different results for THEEM. The graph in Figure 3-11 confirms that the mid-elevation temperatures are higher and thus will give a higher bulk temperature.

In order to reduce this bypass flow, the acrylic vessel would need to be redesigned to form a stronger seal at the top and bottom of the tube bundle. Unfortunately, this would be an expensive and time-consuming process. THEEM also cannot account for this large of bypass flow, so it was assumed that THEEM only modeled the flow through the center of the bundle. This meant it was necessary to calculate the flow rate at this center elevation. Using Equation 3-1 and setting Q_{air}=- Q_{water}, Equation 3-10 was derived to estimate the air mass flow rate through the tube bundle:

$$\dot{m}_{air} = \frac{(\dot{m} C_p \Delta T)_{water}}{(C_p \Delta T)_{air}} \qquad 3\text{-}10$$

The estimated air mass flow rate was $\dot{m}_{air}$= 0.494 kg/s. Since each temperature and pressure drop measurement was taken at the vertical center of the tube bundle right at the outlet of tube bundle, it was assumed that any effect from the bypass flow on these measurements will be negligible. The new flow rate and the other values from Table 3-6 were used with THEEM to obtain the results in Table 3-8.

Table 3-8. Modified THEEM Results Comparison

Parameter	**Experimental Measurements**	**THEEM Values**	**Percent Difference**
Mean Water Temperature Drop	27.9 ± 1.0°C	28.8°C	3.13 %
Mean Water Pressure Drop	0.0154 ± 0.00005 bar	0.0096 bar	60.42 %
Bulk Air Temperature Rise	31.8 ± 1.0°C	33.0°C	3.64 %
Mean Air Pressure Drop	0.00764 ± 0.000098 bar	0.0150	49.07%

The THEEM temperature predictions match closely with the temperature changes that were measured with only 3-4% error, which are also almost completely within experimental error of the thermocouple measurement. This indicates that THEEM can accurately predict the CTGH temperatures, and subsequently, its heat exchanger effectiveness. This is further shown with the comparison of the individual air outlet temperature drop measurements with the THEEM predictions. Table 3-9 shows how THEEM's prediction for the temperature drop at each probe hole location compares with the actual measurement. The maximum error was around 9% in these predictions, which can be attributed partly to the flow maldistribution of the bundle that is discussed in the next section.

It should be noted that the pressure drop measurements have 40-60% error. This indicated that the pressure drop calculations through the tube bundle on both the tube and shell side need to be reexamined. Though it is possible that defects in the experiments caused these errors. For the tube-side measurements, it is possible that the error comes from using the

incorrect friction factor correlation for a curved tube. It may be necessary to use different friction factor correlations to predict the pressure drop across the tube bundle. However, since the bundle is flat, it was also possible that some error may have come from air entrapped in the tubes and the manometer lines. For the shell-side measurements, the error was not as large. It was possible that the bypass flow caused the error in the pressure drop measurements. It also was possible that the difference may have come from THEEM not accounting for the flow maldistribution in the bundle.

Table 3-9. Measured vs. THEEM Air Temperature Changes

Probe Hole	Experimental Measurements[17] [°C]	THEEM Values [°C]	Percent Difference
1	28.4	28.9	1.73%
2	29	31.9	9.09%
3	29	31.9	9.09%
4	30.4	32.2	5.59%
5	30.6	32.5	5.85%
6	29.8	32.8	9.15%
7	31.4	33.4	5.99%
8	32.2	33.7	4.45%
9	31.8	34	6.47%
10	33.2	34.3	3.21%
11	34.7	34.6	0.29%
12	30.1	28.9	4.15%
13	30.2	31.9	5.33%
14	33.7	31.9	5.64%
15	31.9	32.2	0.93%
16	32.3	32.5	0.62%
17	32.9	32.8	0.30%
18	34.1	33.4	2.10%
19	35	33.7	3.86%
20	33.8	34	0.59%
21	35.2	34.5	2.03%

To confirm these results, this experiment was repeated multiple times with varying flowrates to compare multiple configurations with THEEM. The measured inlet values for each experiment are given in Table 3-10. The water temperature drop measurements are given in Table 3-11, the air temperature change measurements are given in Table 3-12, the water pressure drop measurements are given in Table 3-13, and the air pressure drop measurements are given in Table 3-14.

[17] All measurements have an experimental uncertainty of ± 1.0°C, which was defined by thermocouple manufacturer

Table 3-10. Validation Experiments' Inlet Values[18,19]

Experiment	Measured Air Flowrate	Modified Air Flowrate	Air Inlet Temperature	Water Flowrate	Water Inlet Temperature
1	0.606 kg/s	0.494 kg/s	19.9°C	0.136 kg/s	67.9°C
2	0.617 kg/s	0.499 kg/s	21.5°C	0.134 kg/s	69.8°C
3	0.579 kg/s	0.506 kg/s	21.3°C	0.136 kg/s	68.6°C
4	0.605 kg/s	0.526 kg/s	20.1°C	0.113 kg/s	70.4°C
5	0.493 kg/s	0.485 kg/s	21.5°C	0.141 kg/s	69.0°C
6	0.614 kg/s	0.466 kg/s	20.0°C	0.141 kg/s	66.4°C

Table 3-11. Mean Water Temperature Drop

Experiment	Experimental Measurements	THEEM Values	Percent Difference
1	27.9 ± 1.0°C	28.8°C	3.13 %
2	28.3 ± 1.0°C	29.4°C	3.74 %
3	28.2 ± 1.0°C	28.8°C	2.26 %
4	34.1 ± 1.0°C	35.2°C	3.27 %
5	26.8 ± 1.0°C	27.5°C	2.73%
6	26.7 ± 1.0°C	26.3°C	1.33 %

Table 3-12. Mean Air Bulk Temperature Rise

Experiment	Experimental Measurements	THEEM Values	Percent Difference
1	31.8 ± 1.0°C	33.0°C	3.64 %
2	31.6 ± 1.0°C	32.9°C	3.84 %
3	31.4 ± 1.0°C	32.2°C	2.41 %
4	30.3 ± 1.0°C	31.4°C	3.52 %
5	32.2 ± 1.0°C	33.3°C	3.23 %
6	31.9 ± 1.0°C	33.0°C	3.43 %

Table 3-13. Mean Water Pressure Drop

Experiment	Experimental Measurements	THEEM Values	Percent Difference
1	0.0154 ± 0.00005 bar	0.0096 bar	60.42 %
2	0.0156 ± 0.00005 bar	0.0093 bar	68.19 %
3	0.0143 ± 0.00005 bar	0.0095 bar	50.22 %
4	0.0118 ± 0.00005 bar	0.0077 bar	52.95 %
5	0.0161 ± 0.00005 bar	0.0098 bar	64.35 %
6	0.0148 ± 0.00005 bar	0.010 bar	47.89%

[18] Experiment 1 is the experiment described earlier in this section. It is included for comparison.

[19] The experimental uncertainty value for each measurement is given in Table 3-6. They are not included here so that it is easier to read this table.

Table 3-14. Mean Air Pressure Drop

Experiment	Experimental Measurements	THEEM Values	Percent Difference
1	0.00764 ± 0.000098 bar	0.0150 bar	49.07 %
2	0.00631 ± 0.000098 bar	0.0153 bar	58.76 %
3	0.00675 ± 0.000098 bar	0.0153 bar	57.03 %
4	0.00739 ± 0.000098 bar	0.0166 bar	55.47 %
5	0.00581 ± 0.000098 bar	0.0146 bar	60.19 %
6	0.0080 ± 0.000098 bar	0.0140 bar	42.63 %

Over multiple experiments, THEEM was able to predict the overall temperature change of both the air and the water with an error of only 1-4%. This further confirms that THEEM can be used to model the heat transfer and predict the effectiveness of the CTGH. Multiple experiments also confirm that THEEM is not able to accurately predict the pressure drop of CASET. For the tube-side, THEEM consistently underestimates the water pressure drop by 50-60%. There is the possibility that air bubbles in the water loop are giving inaccurate manometer readings or are causing greater head loss in the tubes than THEEM predicts. This problem was further exasperated by the need to drain CASET between experiments. There was one minor leak in one of the tube-to-tube sheet joints that could not be sealed with silicone. The leak was small enough that it did not affect CASET during experiments. However, if left for a long period of time, large amounts of water would eventually leak out. Refilling CASET introduced more air bubbles in the system. If CASET could be left filled between experiments, it might have been possible to force most of the air bubbles out of the system, which may change the pressure drop measurements. For the shell-side, THEEM also consistently overestimated the air pressure drop by 40-60%. This is likely due to bypass flow and flow maldistribution. The bypass flow would encounter less friction than the flow through the tube bundle, resulting in a smaller pressure drop overall. In order to correct for these issues on both the shell-side and tube-side, either a new experiment needs to be constructed or modifications need to be made to CASET. Until then, the current experimental results indicate that THEEM is a fairly accurate tool for modeling the heat transfer and effectiveness.

3.2.3.2 Airflow Distribution Measurements

The bypass flow discovered in the validation experiment was also a factor in measuring the flowrate distribution. The velocity measurements were taken at the vertical center of tube bundle like the temperature and pressure drop measurements. However, as seen in Figure 3-10, the anemometer probe is relatively small and is set further back than the other probes from the outer edge of the tube bundle. It is possible that any flow over the top or bottom of tube bundle may have distorted the flowrate measurements. It was assumed that the separation between the tube bundle and the top and bottom plate were consistent around the tube bundle, giving a relatively uniform bypass flow across the tube bundle. Therefore, it should be possible to compare the flow at each point in order to find the flow distribution across the bundle. The placement and 2-D design of the anemometer probe meant that it would only measure the flow in the radial and azimuthal directions. The bypass flow mainly affected the vertical velocity component since the air flowed over the top and bottom of the bundle, so it would not have caused much issue with the velocity measurements.

After taking the measurements at each point, the average outlet air velocity was calculated to be 5.74 m/s with a standard deviation of 1.36 m/s. Figure 3-12 shows how the flow rates vary from the average velocity. The relative flow rates at points 1 and 12 were larger because those points were adjacent to the outer manifolds and were set further back from the tube bundle. The manifolds cause some flow distortion, so it was to be expected to have increased flow at these points. The flow at point 19 was likely caused by manufacturer defects in the tube bundle leading to some flow maldistribution. It should also be noted that the supports for the tubes were much closer between points 2 through 9, as seen in Figure 3-8. The tubes' free spans were much shorter in this part of the bundle, which meant the tubes were less likely to overlap or touch as they would with the longer spans seen between points 10 through 21. This meant the flow should be more consistent at these points. In Figure 3-12, the flow did not vary as greatly at these points as it did with the points with longer tube spans.

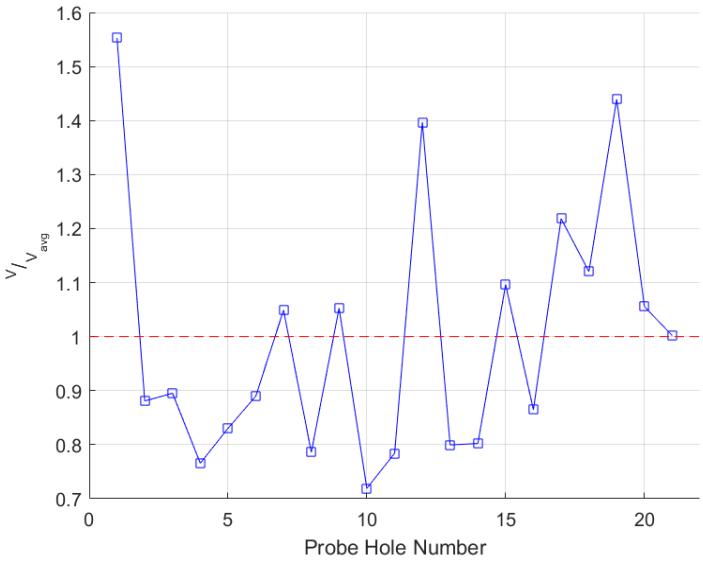

Figure 3-12. Airflow Velocity Distribution around Tube Bundle

Another important factor in the flow distribution was the direction of the airflow. The 2-D probe measured the azimuthal and radial components of the air velocity. In the tube bundle, the flow would not be purely radial due to manufacturer defects and realistic air flow. Since the probe was positioned in each measurement to be facing the bundle in the radial direction, it was possible to calculate in what direction the flow was heading as it exited the tube bundle. Figure 3-13 shows at what angle the air was flowing relative to a purely radial flow. Similar to Figure 3-12, the azimuthal angles were greater at points 1 and 12 since the air flowed around the manifolds at those points. The rest of the points were useful in modeling the flow through the bundle. The data in both Figure 3-12 and Figure 3-13 can be used in a future iteration of THEEM to predict the flow distribution through the bundle, which will improve the accuracy of both the effectiveness and gas pressure drop calculations.

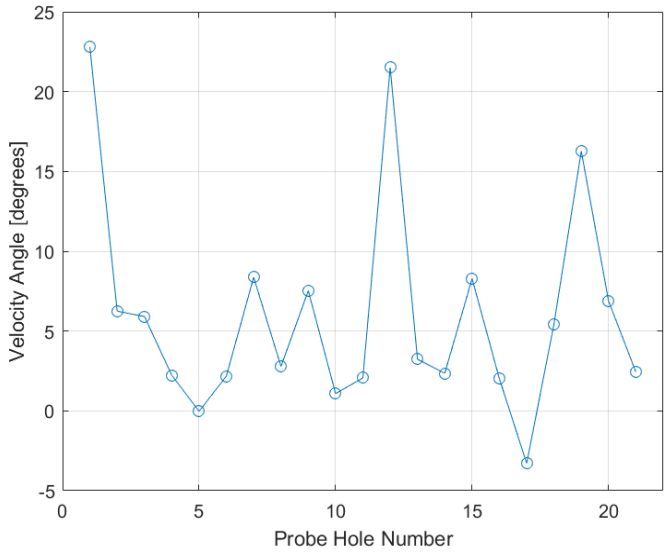

Figure 3-13. Airflow Direction around Tube Bundle

3.2.3.3 Wilson Plot Method

Similar to the validation experiments, the air flow rates were adjusted using Equation 3-10 in order to account for the bypass flow over the bundle. Using the iteration method described earlier, a linear regression was performed on Equation 3-7. The experimental data points and the linear regression are shown in Figure 3-14. Equation 3-11 gives the derived equation and the R^2 value of the regression.

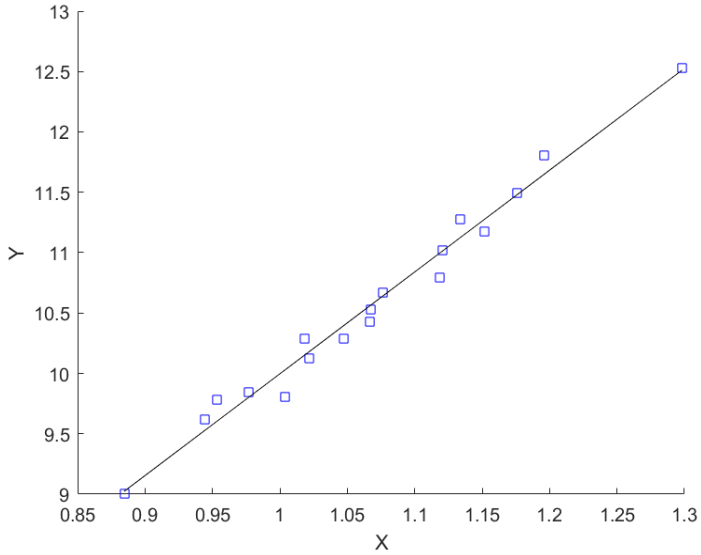

Figure 3-14. Linear regression of thermal resistances according to the Wilson Plot method

$$Y = 8.431X + 1.562 \qquad 3\text{-}11$$
$$R^2 = 0.9806$$

After iteratively guessing the values for m and p and combining Equations 3-7 and 3-11, the remaining variables were found and used with the original Nusselt number correlations. Table 3-15 and Figure 3-15 compare the theoretical and experimental Nusselt number

correlations for the shell-side. Table 3-16 and Figure 3-16 compare the Nusselt number correlations for the tube-side.

There is a significant difference between the theoretical correlations and the experimental correlations for the convection heat transfer correlations for both the shell-side and tube-side. The shell-side theoretical model (Zukauskas) underestimates the convection heat transfer coefficient by a factor of approximately 6. The tube-side theoretical model (Kalb and Seader) overestimates the convection heat transfer coefficient by a factor of approximately 5.5. On the tube-side, the model presented by Kalb and Seader was developed for tubes with a curvature ratio (radius of bend/inside radius of tube) between 10 and 100. The mean curvature ratio of this tube bundle is 137. Since this tube bundle is outside the range of application of this correlation, it is sensible that this experiment developed a different Nusselt number correlation. On the shell-side, the Zukauskas model was developed specifically for straight tubes in crossflow. The air flowing through the CTGH flows through coiled tubes radially, which may explain the difference between the theoretical and empirical correlation. It is also possible that some error may come from the bypass flow. Using the air temperature at the center of the bundle, using the calculated flow through the tube bundle, and assuming that the effect of the bypass flow was negligible at the center of the bundle may be the reason that the experimental results did not match the theoretical models. This could be confirmed by fabricating another experiment or modifying CASET so that there is no more bypass flow.

Table 3-15. Air Nusselt Number Correlations

Model	Formula
Zukauskas [29] (Theoretical)	$Nu_s = 0.3627 * (Re^{0.60} Pr^{0.36})_s$
Experimental	$Nu_s = 0.640 * (Re^{0.741} Pr^{0.36})_s$

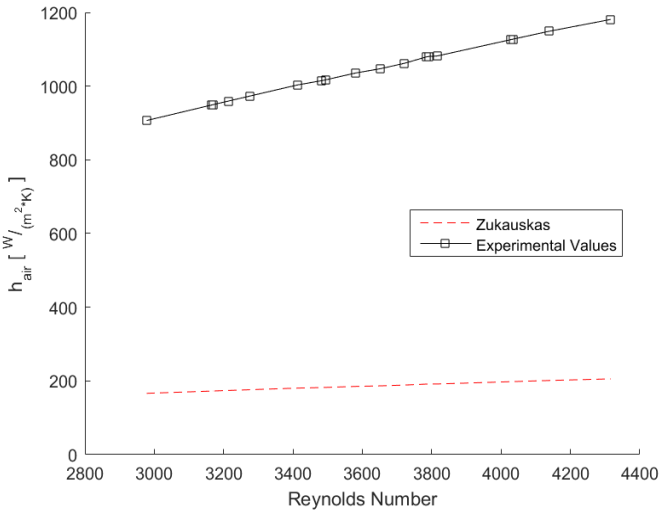

Figure 3-15. Comparison of theoretical & experimental model for air convection heat transfer coefficients

Table 3-16. Water Nusselt Number Correlations

Model	Formula
Kalb and Seader [50] (Theoretical)	$Nu_t = 0.913(De^{0.476}Pr^{0.2})_t$
Experimental	$Nu_t = 0.119(De^{0.516}Pr^{0.2})_t$

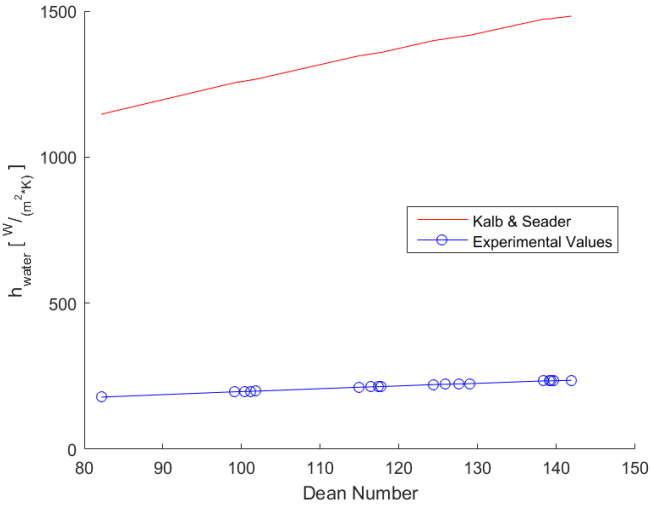

Figure 3-16. Comparison of theoretical & experimental model for water convection heat transfer coefficients

3.2.3.4 Impulse Response Measurement

As expected, the impulse response measurement gave some general data about the tube bundle and CASET itself. The pump and fan were started up before the heater. Once there were no more air bubbles in the loop, the heater was switched on to full power. Figure 3-17 shows the inlet and outlet water temperature of one of the loops change over time when the heater is first turned on at full power.[20] The inlet temperature rises almost immediately by 10-15°C. The outlet temperature has approximately a 52 second delay, which corresponds to the residence time of the water in the tube bundle. The inlet temperature plateaus for approximately another 40 seconds. This corresponds to the water residence time in the rest of the CASET experiment, giving the water a total residence time of approximately 90 seconds. The water temperature then rises slowly before reaching a steady-state temperature difference of about 28°C after approximately 15 minutes.

After the water reached steady-state, the heater was switched off completely. Figure 3-18 shows how the liquid temperature responds to a sudden full heat loss transient. Similar to the heater turning on, the inlet water temperature changes almost immediately. The water inlet temperature drops by approximately 25°C almost immediately. The outlet water temperature drop is delayed once again by the 52 second residence time in the tube bundle. After approximately another 40 seconds, the inlet water temperature begins dropping again after the

[20] The figures show the temperatures of Manifold 1. Manifold 2's temperatures are almost identical, so it is not shown for brevity.

water has completely circulated around the entire CASET loop. An 8-10°C temperature difference remains across the bundle until the outlet temperature begins approaching room temperature and levels off. The water at both the inlet and outlet reaches room temperature after about 10-12 minutes.

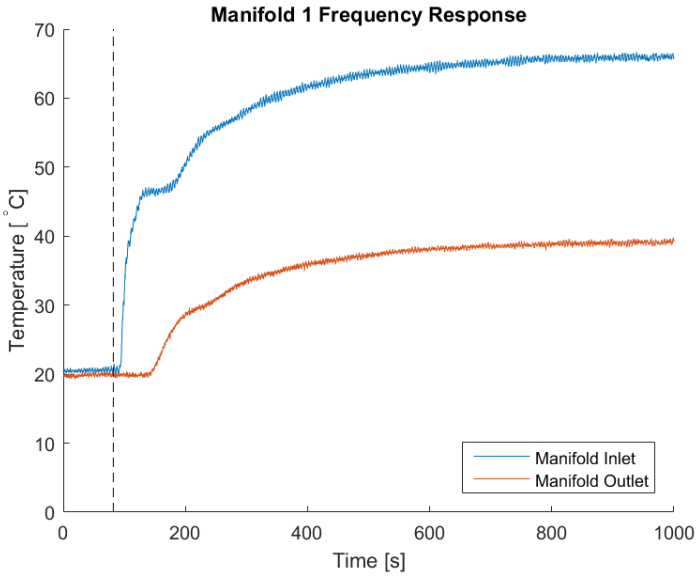

Figure 3-17. Impulse Response at Start-up

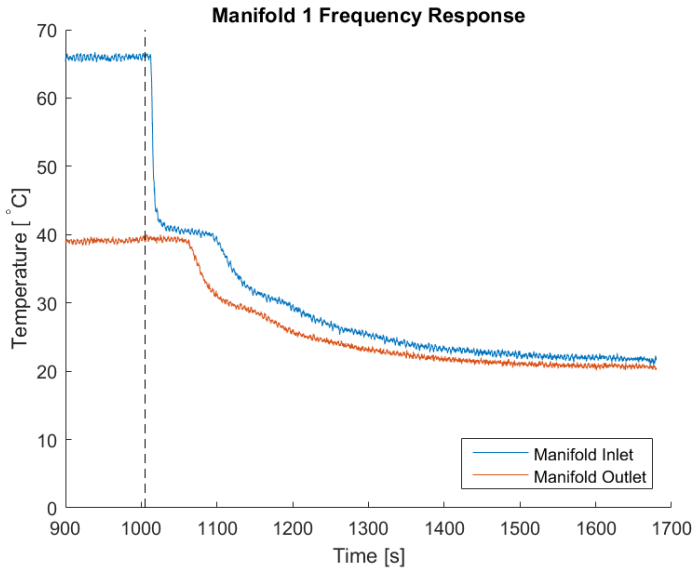

Figure 3-18. Impulse Response to Full Power Loss

After the first shutdown, the heater was switched to full power again and the water temperature was allowed to reach steady state. Then, only half the heater power was switched off. Figure 3-19 shows the impulse response of the water temperature to the loss of half power. Similar to full power loss, the inlet temperature dropped immediately. However, it only dropped

by 10°C instead of 25°C. The outlet temperature once again had the 52 second delay in temperature drop. Though, this time the temperature only drops by 5-7°C before reaching steady state. Since the water does not cool down to room temperature, it reached steady-state temperature much quicker. It reached a steady-state temperature difference of 14°C after approximately 8 minutes.

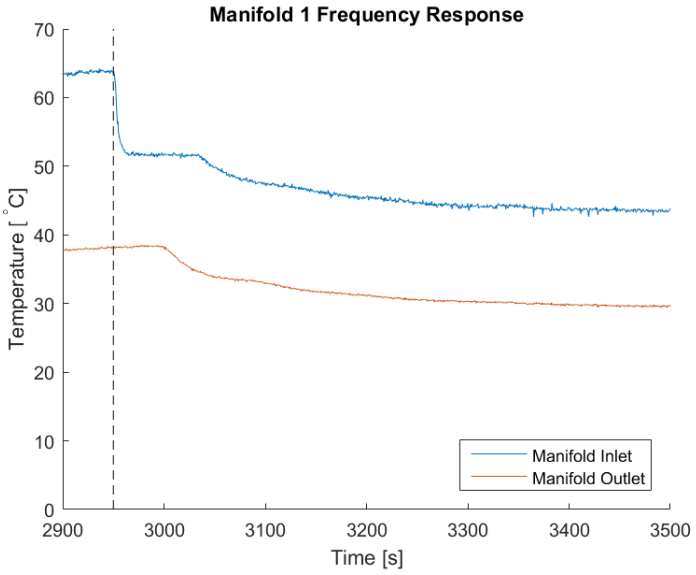

Figure 3-19. Impulse Response to Half Power Loss

This data was useful in measuring the residence time and also measuring how long it took the bundle to reach steady-state. This data could be used in the future to estimate how long the actual CTGH would take to reach steady-state after a shutdown or start-up in an actual reactor application. Further frequency response testing will need to be performed in the future in order to see how the CTGH will respond to various other transients or accident scenarios.

3.3 Experiment Conclusions & Future Work

3.3.1 Tube Fabrication

One outcome of the CASET experiment was the ability to measure the success of the tube fabrication method. Bending the tubes by hand was the fabrication method for the original CTGH experiment tube bundle. This would be a difficult process to scale to coil more tubes for much larger CTGHs. There would be a large amount of variation in each tube, and it would take a long time to fabricate thousands of these tubes. Also, as the results of the first experiment showed, this created large flow maldistribution through the bundle, confirming that this fabrication method would not be optimal for large scale production of a full-sized CTGH bundle. The CASET tube bundle was fabricated using a die and mandrel. This method produced more consistent tube coils than coiling them by hand. However, there was still some variability in tubes using this method since it required the tubes to be fixed by hand before they could be used in the tube bundle. This variability increased the probability of flow maldistribution in the tube

bundle. It also took time to fix each tube by hand, which made the process impractical for large-scale production of these tube bundles.

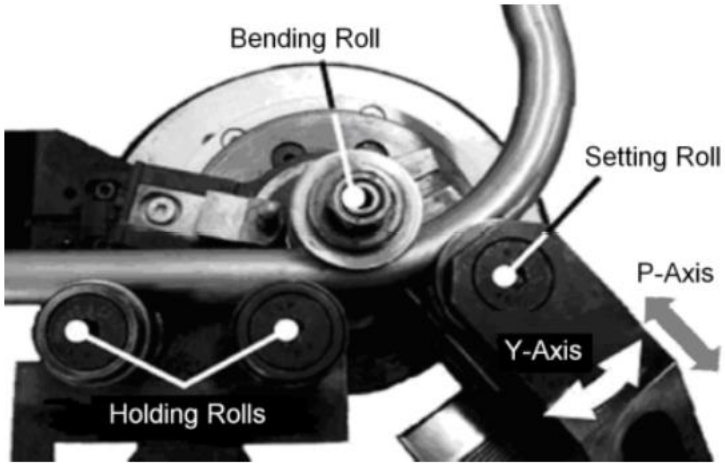

Figure 3-20. Tool of a three-roll push bending machine [54]

The tube coiling method needs to be a process that produce consistent tube coils while minimizing fabrication time. Preferably, this should be an automated method that requires minimal human assistance. One possible method is three-roll push bending. In this process, the tube is guided between a holding roller(s) and a bending roller. The tube is pushed through these rollers before it comes into contact with the setting roller. The position of the setting roller defines the bending radius of the tube. An example of a three-roll push bending tool is shown in Figure 3-20. The bending point is the tangent point between the tube and the bending roller. In this example, to change the radius of the tube, the setting roll's position can be changed along the p-axis or the y-axis. This method offers more control over the shaping the tube, gives the process better repeatability, and makes it possible for the shape to be formed by a computer. The setting roller can be designed so that a computer controls its position. There are research efforts to determine the machine parameters needed to form the tube correctly and minimize deviation. These parameters would account for the material spring back and the deflection of the machine itself [54], [55]. This method appears to have potential to be used for large scale CTGH fabrication. The next tube bundle that is constructed should be fabricated using this method to test its potential.

3.3.2 Experimental Results

The results of the experiments showed that THEEM can be an effective tool for predicting the effectiveness of CTGHs, but the pressure drop measurements indicated that further testing is needed. First, CASET needs to be modified to eliminate possible causes for the discrepancy between the predicted and measured pressure drops. The loop could be modified so that it is possible to force all the air bubbles out of the water loop. This could be done with either a new sloped bundle or by modifying the procedure to fill the CASET loop so that it flushes more air bubbles out. Then, the vessel around the tube bundle could be modified or redesigned to minimize bypass flow over the top and bottom of the tube bundle. If the results still do not

match the THEEM predictions, then the THEEM pressure drop calculations will need to be modified to match the experimental results. So, THEEM can be used for the design of CTGHs for various applications; however, the pressure drop predictions will need further consideration. However, the pressure drop predictions seem to be within an order of magnitude of the actual pressure drops, so they can be used as a general estimation of the actual pressure drop across the tube bundle.

Next, in order to further validate the results of these experiments, it will be necessary to build another tube bundle. For example, the flow maldistribution could be measured with these two tube bundles presented in this chapter, but they were fabricated with methods that are not optimal for large scale manufacturing. The effect of the different manufacturing processes on flow maldistribution can be studied further with multiple tube bundles. Also, another tube bundle will allow for further measurements to be used with the Wilson plot method in order to test the heat transfer correlations developed for the tube bundle. Currently, the experimental correlations in Table 3-15 and Table 3-16 can be used to model the heat transfer for the tube bundle. These simple correlations can easily be used by system modeling codes, such as RELAP, to model the heat transfer in a tube bundle. It should be noted that these correlations were derived using only one tube bundle and that there was a large difference between the theoretical correlations and the experimentally derived correlations. These correlations need to be tested on tube bundles of different sizes to confirm the correlation, to develop a geometric range in which these correlations apply, and to study why the theoretical and experimental correlations do not match.

Finally, it is necessary to modify CASET or build a new experiment in order to measure the frequency response of the CTGH to various accident scenarios. It likely would be easier to modify CASET so that it has a control system to control the fan and pump speed and to install a power supply for the heater so that it is possible to do more than just turn the heater on or off. These experiments could be used to model accident scenarios, such as a LOFC, a Loss of Offsite Power (LOOP), or a sudden and large insertion of positive reactivity, which increases the heat from the reactor. This data could be used in integral effect tests, like CIET, or in the design and licensing of reactor safety systems that use the CTGH as the primary method of heat removal.

Chapter 4.
CTGH Design Optimization

After validation of THEEM, the next step was to develop a tool to design CTGHs for various applications. This optimization tool was designed to use a Monte Carlo method algorithm with the 0-D THEEM code. This chapter examines how the different geometric parameters affect the overall design of the CTGH, discusses the development of the optimization tool, and gives example CTGH designs that were developed by using this tool for different nuclear and non-nuclear applications.

4.1 Geometric Parametric Study

In order to develop an optimization tool, the first step was determining which parameters should change to give an optimal CTGH design. All of the input parameters for THEEM are listed in Chapter 2. The heat transfer fluid properties, such as temperatures, pressures, and mass flow rates, are determined by the nuclear reactor and Brayton cycle design. The number of heater rods is a fixed quantity based on the freezing point of the liquid coolant. The slope of the tube is the minimum slope required for the liquid coolant to drain and therefore is dependent on the type of fluid. The number and width of tie rod gaps is derived from a stress analysis on the bundle and vessel, so they are also fixed quantities. Finally, the thickness of the tube wall is dependent on the pressure difference between the gas and the liquid. In order to minimize cost, the tube selection was based on commonly used tube sizes. In order to minimize liquid pressure loss, the thinnest tube available for a given tube diameter that meets ASME standards was used. This leaves 9 geometric parameters:

- Number of Sub-bundles ($N_{bundles}$)
- Tube outer diameter (D_o)
- Number of liquid manifolds ($N_{Manifolds}$)
- Number of tube layers per sub-bundle (N_{layers})
- Number of loops in bundle (N_{loops})
- Bundle Inside Radius ($R_{in,bund}$)
- Longitudinal Pitch-to-Diameter Ratio (S_L)
- Transverse Pitch-to-Diameter Ratio (S_T)
- Number of tubes per layer per manifold (N_{rows})

In order to design an optimal heat exchanger, it was necessary to study how variation of these parameters changed the overall effectiveness, the gas pressure drop, and the liquid pressure drop. This parametric study shows how changing each geometric parameter individually would affect each of these three output factors. An initial base design was needed in order to perform

this study, so the original prototypical Mk1 PB-FHR CTAH was chosen.[21] Then each geometric parameter was tested over a range of values. The code would keep all the other parameters constant; these inputs were then used for the 2D THEEM code. The results for each parameter is given in Figure 4-1 through Figure 4-18.

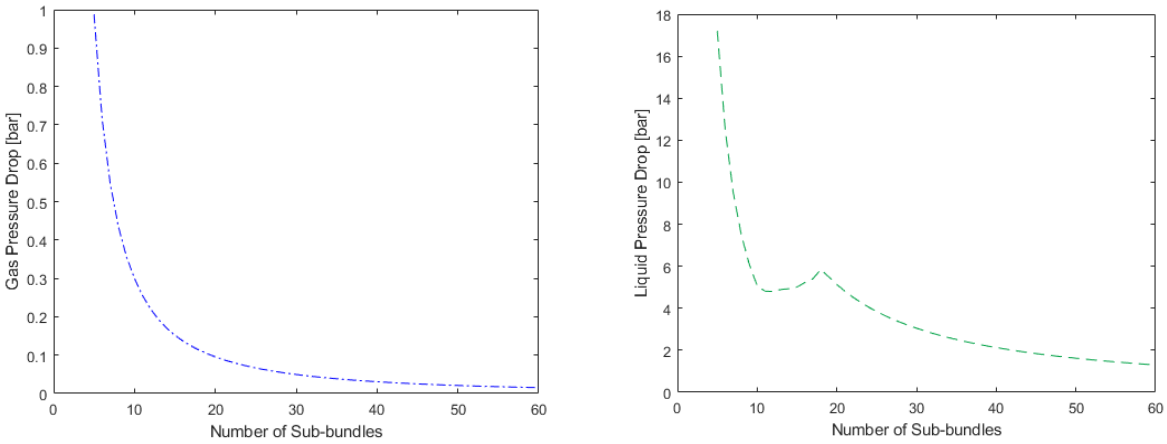

Figure 4-1. Number of Sub-bundles vs. Pressure Drop for Gas (Left) & Liquid (Right)

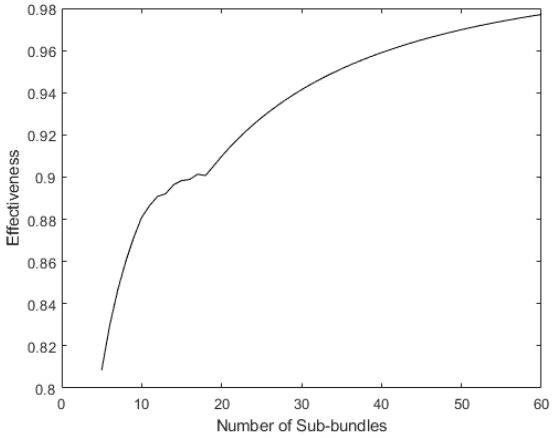

Figure 4-2. Number of Sub-bundles vs. CTGH Overall Effectiveness

[21] This base design is different from the Mk1 PB-FHR CTAH design presented in Chapter 2. That design was developed using the optimization tool discussed later in this chapter.

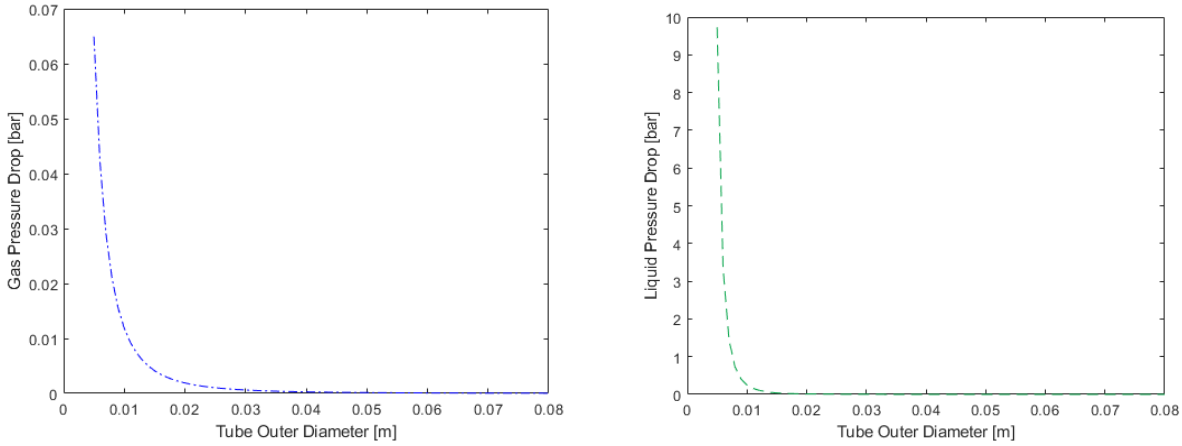

Figure 4-3. Tube Outer Diameter vs. Pressure Drop for Gas (Left) & Liquid (Right)

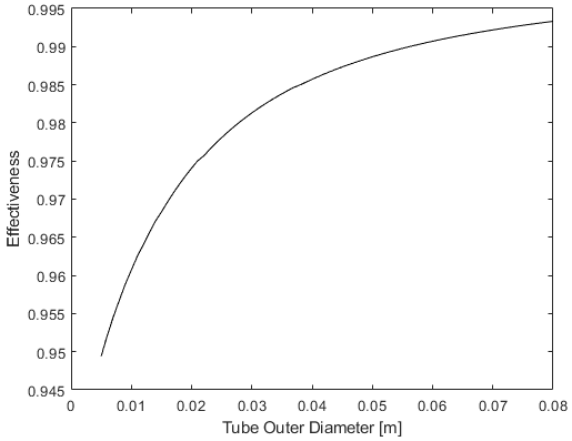

Figure 4-4. Tube Outer Diameter vs. CTGH Overall Effectiveness

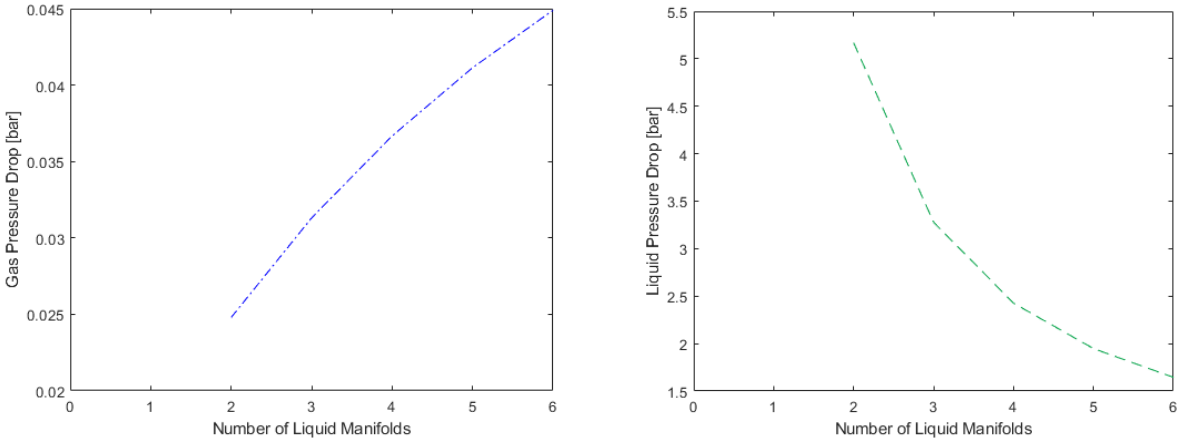

Figure 4-5. Number of Manifolds vs. Pressure Drop for Gas (Left) & Liquid (Right)

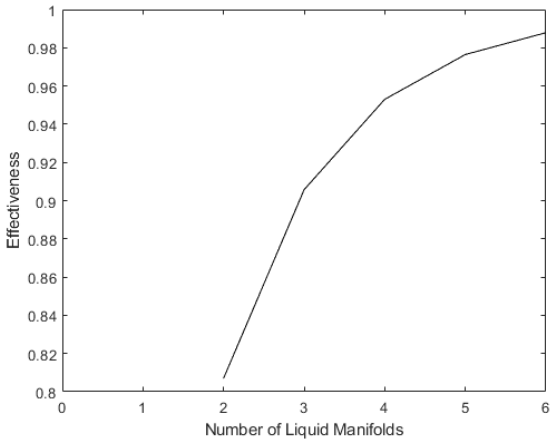

Figure 4-6. Number of Manifolds vs. CTGH Overall Effectiveness

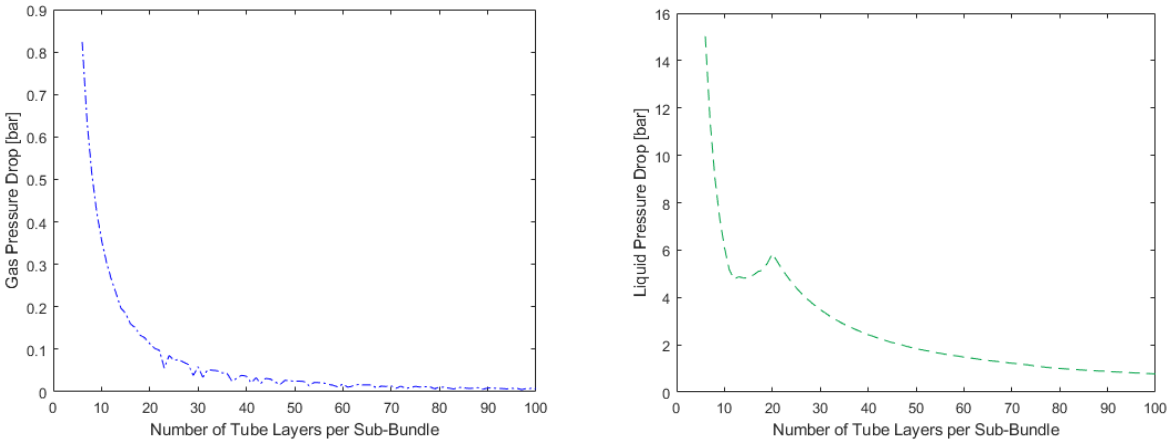

Figure 4-7. Number of Tube Layers vs. Pressure Drop for Gas (Left) & Liquid (Right)

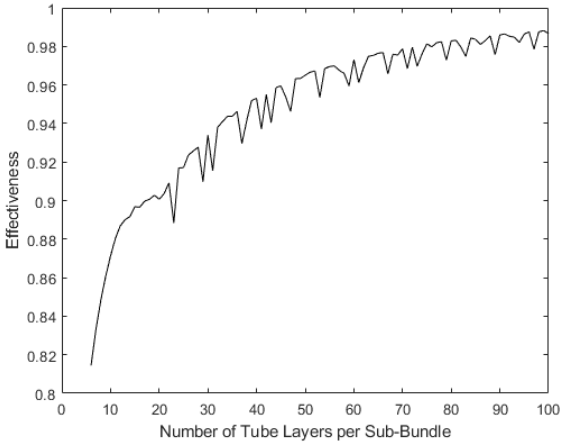

Figure 4-8. Number of Tube Layers vs. CTGH Overall Effectiveness

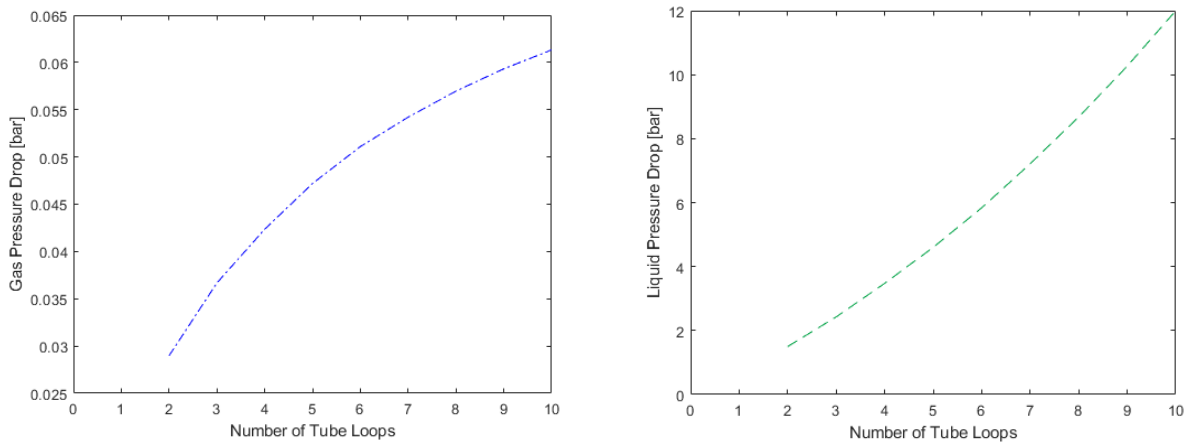

Figure 4-9. Number of Loops vs. Pressure Drop for Gas (Left) & Liquid (Right)

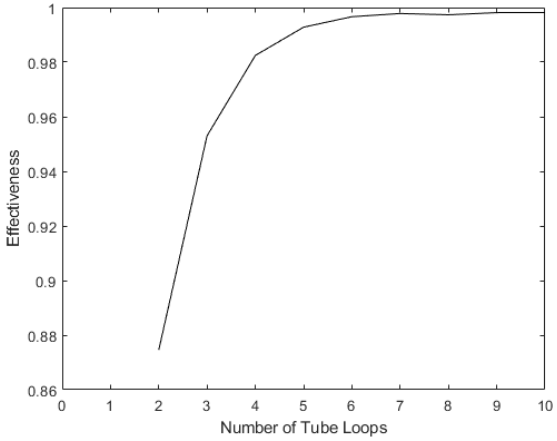

Figure 4-10. Number of Loops vs. CTGH Overall Effectiveness

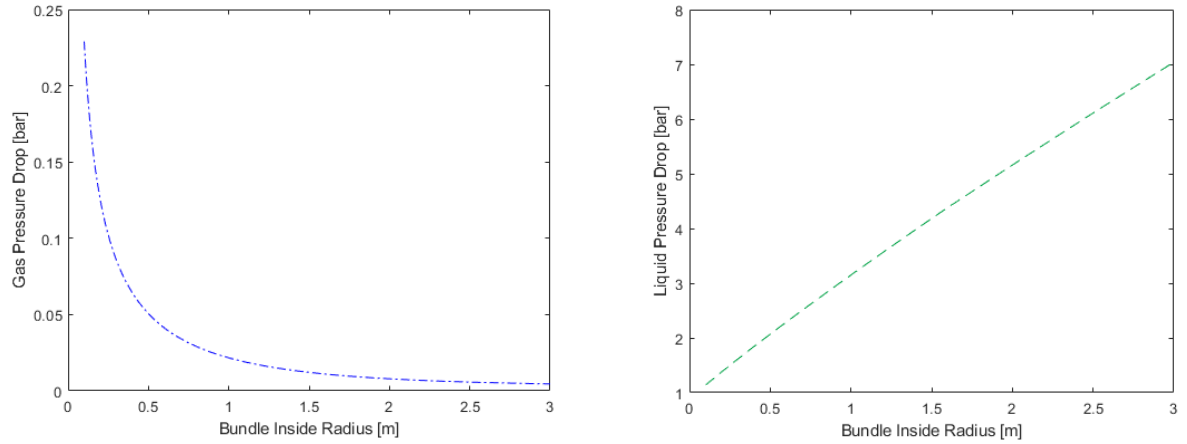

Figure 4-11. Bundle Inside Radius vs. Pressure Drop for Gas (Left) & Liquid (Right)

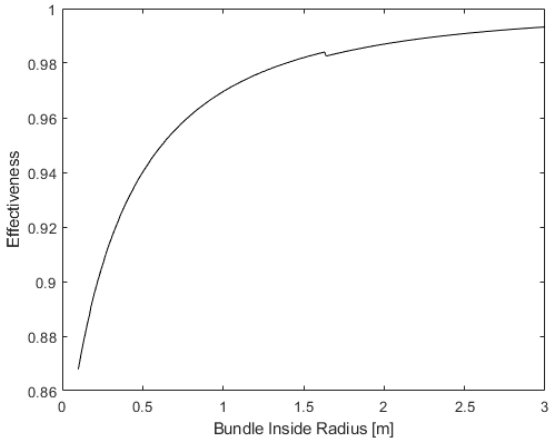

Figure 4-12. Bundle Inside Radius vs. CTGH Overall Effectiveness

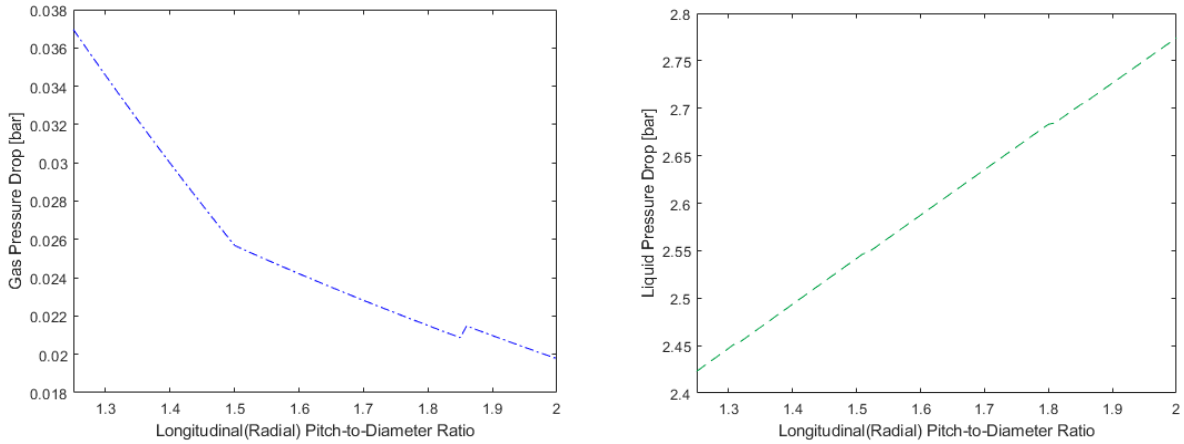

Figure 4-13. Longitudinal Pitch-to-Diameter Ratio vs. Pressure Drop for Gas (Left) & Liquid (Right)

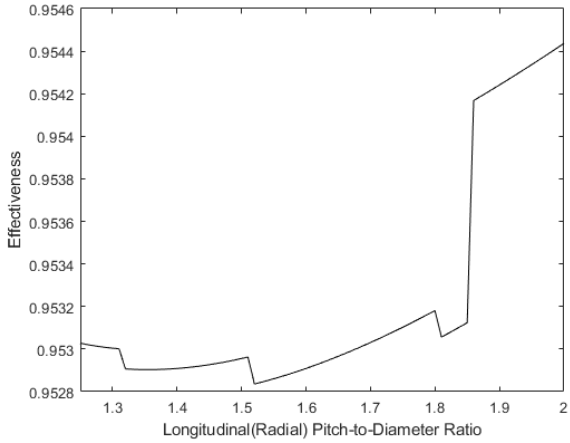

Figure 4-14. Longitudinal Pitch-to-Diameter Ratio vs. CTGH Overall Effectiveness

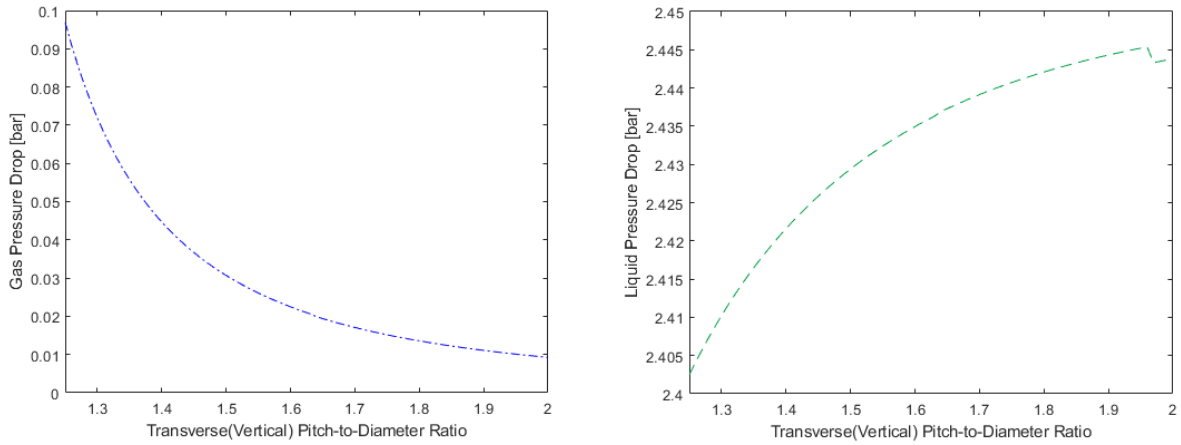

Figure 4-15. Transverse Pitch-to-Diameter Ratio vs. Pressure Drop for Gas (Left) & Liquid (Right)

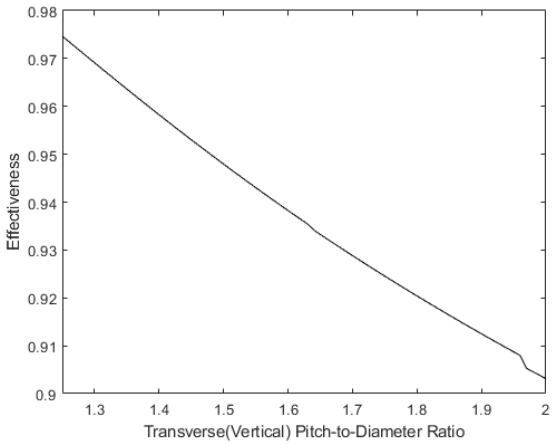

Figure 4-16. Transverse Pitch-to-Diameter Ratio vs. CTGH Overall Effectiveness

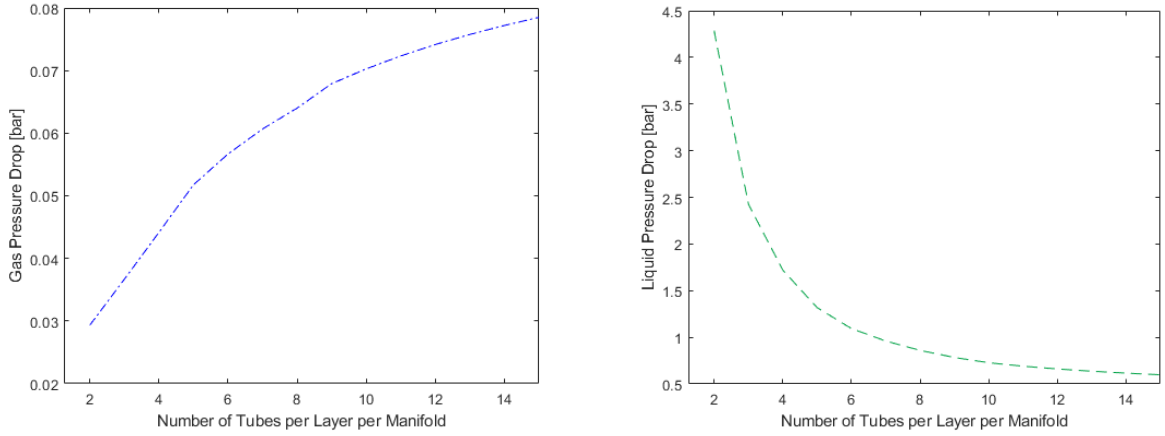

Figure 4-17. Number of Tubes per Layer vs. Pressure Drop for Gas (Left) & Liquid (Right)

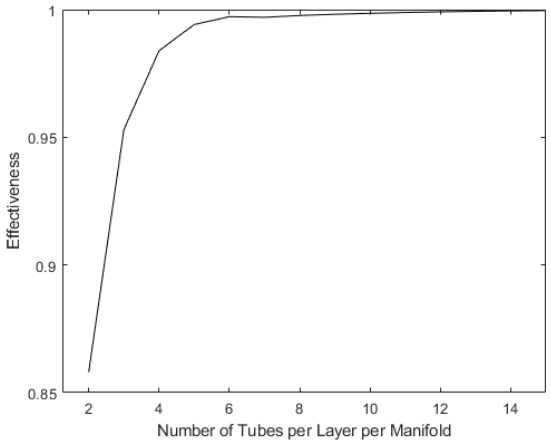

Figure 4-18. Number of Tubes per Layer vs. CTGH Overall Effectiveness

These results show the general influence of each geometric parameter on the frictional pressure drops and effectiveness. The output values will change with different base designs and different heat transfer fluids, but one design can still show the variation in these three outputs based on changing an individual geometric parameter. The variance for each graph was calculated to show the distribution of output values. The gas and liquid pressure drop variances from changing each geometric parameter are shown in Figure 4-19, and the variances of the effectiveness are shown in Figure 4-20. If a certain input parameter gives a larger distribution of output values, that geometric parameter will have a larger effect on the output values. This will show which geometric parameters should be a priority for the optimization tool. For example, the graphs for the longitudinal pitch-to-diameter ratio, S_L, (Figure 4-13 & Figure 4-14) show that as S_L increases, generally, the gas pressure drop decreases, the liquid pressure drop increases, and effectiveness increases. However, Figure 4-19 and Figure 4-20 show that the changes in pressure drops and effectiveness due to changing S_L are negligible in comparison to other geometric parameters and should not be a priority in the optimization tool. As a counter-example, the graphs for the number of sub-bundles (Figure 4-1 & Figure 4-2) show that increasing the number of sub-bundles in the CTGH generally decreases both the gas and liquid pressure drop and increases the effectiveness. These output values have a much larger distribution than the output values obtained by changing S_L. As Figure 4-19 and Figure 4-20 show, the variance for changing the number is sub-bundles is significant for each output. Based on these figures, the parameters could be ranked for each output on how significant of an effect it has on that output. This is discussed in further detail in the next section.

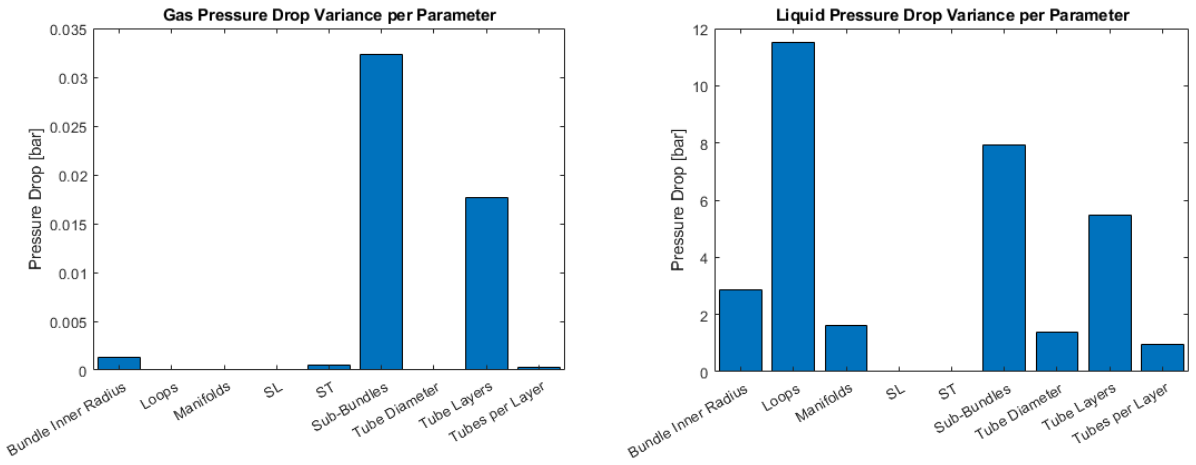

Figure 4-19. Statistical Variances of Gas Pressure Drop (left) & Liquid Pressure Drop (right) for Each Geometric Parameter

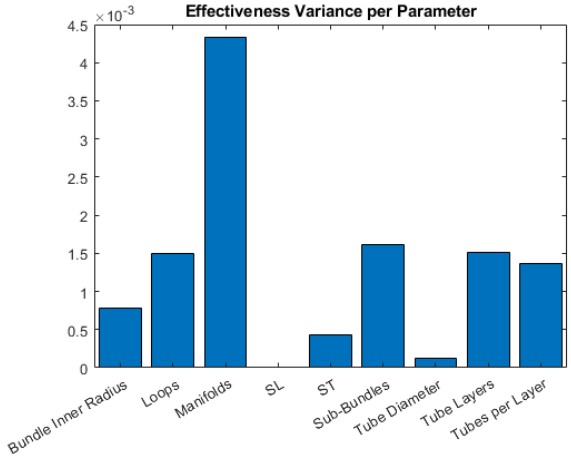

Figure 4-20. Statistical Variances of Effectiveness for Each Geometric Parameter

4.2 THEEM Optimization Tool Development

Optimizing the CTGH design poses a series of challenges. Out of the nine geometrical parameters, three are continuous variables (S_T, S_L, $R_{in,bund}$) with the remaining six being discrete variables ($N_{Manifolds}$, N_{loops}, N_{rows}, $N_{bundles}$, N_{layers}, D_o)[22]. This optimization problem also involves optimizing three outputs: maximizing the heat exchanger effectiveness, minimizing the overall gas pressure drop, and minimizing the overall liquid pressure drop. Due to the complexity of the THEEM calculations and trying to optimize three outputs at once, the optimization tool uses a Monte Carlo algorithm to find a design. A Monte Carlo simulation can be used as an optimization tool by applying a stochastic technique to a deterministic problem. The three outputs are deterministic problems that are difficult to optimize due to their

[22] In order to minimize costs, the CTGH will not use customized tubing, so the tube sizes are limited to what is available currently on the market. For this reason, the tube diameter is considered a discrete variable.

complexity. By introducing randomness artificially into this optimization problem, it is possible to try various combinations of different inputs and more efficiently search for optimal designs. Monte Carlo presents a relatively simple and flexible algorithm that can be used for various design optimizations. The optimization tool randomly select values for the 9 geometrical parameters, uses them as inputs for the THEEM 0-D code, and records the code output. It repeats this process thousands of times in order to test a large number of geometric combinations. By using a stochastic approach, the optimization tool will generally avoid any biases in selecting input parameters and give a more complete overview of what designs are possible. By testing a large enough number of random input combinations, this tool should be able to find one of the most optimal heat exchanger designs [56].

The Monte Carlo method randomly chooses the input parameters, but, in order for the design to be feasible, it was necessary to put constraints on these parameters by giving them a range of values to randomly choose from. These maximum and minimum values were not based on the parametric study discussed in the previous section; they were chosen as starting constraints, which could be modified later by the optimization code. These ranges constrain the parameters so that the design is physically possible, the heat exchanger maintains the characteristics of a CTGH, and the heat exchanger does not become unreasonably large. For the optimization code, the input parameters have the following initial constraints:

$$5 \leq N_{bundles} \leq 100$$

$$3/16" \leq D_o \leq 1"$$

$$2 \leq N_{Manifolds} \leq 6$$

$$5 \leq N_{layers} \leq 100$$

$$2 \leq N_{loops} \leq 10$$

$$0.25\ m \leq R_{in,bund} \leq 1.5\ m$$

$$1.25 \leq S_L \leq 2.0$$

$$1.25 \leq S_T \leq 2.0$$

$$2 \leq N_{rows} \leq 8$$

These initial constraints do not greatly restrict the CTGH tube bundle. However, depending on the application, there are often size constraints on the tube bundle. Since the CTGH was originally designed to be used with SMRs, it is important to keep the heat exchanger size relatively small. For example, the Mk1 FHR design required that the CTAHs be rail transportable, so the pressure vessel diameter cannot be greater than 3.5 meters. This means that these parameters would likely need to be constrained further. Equations 4-1 and 4-2, which were originally given in Chapter 2, show the that each of these nine geometric parameters have either a linear relationship with or no effect on the radius and the height of the tube bundle. Given bundle or vessel size constraints specified by the user, these equations can be used to further limit the input parameters.

$$R_{out,bund} = R_{in,bund} + (2 * N_{Manifolds} * N_{loops} * N_{rows} * S_L * D_o + N_{gap} * t_{gap}) \quad 4\text{-}1$$

$$H_{bund} = N_{bundles} * \left(D_o * S_T * \frac{N_{layers} + 1}{2} + t_{disk}\right) \quad 4\text{-}2$$

It is difficult to place constraints on all nine input parameters based on two equations. Using the results from the parametric study, it was possible to prioritize the parameters based on which parameters had the greatest effect on each of the three outputs. The most influential geometric parameters for each output, which were obtained by using Figure 4-19 and Figure 4-20, are given in Table 4-1. The table also states whether each parameter should be maximized or minimized based on the results from the parametric study (Figure 4-1 through Figure 4-18).

Table 4-1. Ranking of Geometric Parameters on CTGH Outputs

Output Variable Constraint	Most Influential Parameters Constraints
Minimize Gas Pressure Drop	1. Maximize Number of Sub-bundles 2. Maximize Number of Tube Layers per Sub-bundle
Minimize Liquid Pressure Drop	1. Minimize Number of Loops in Bundle 2. Maximize Number of Sub-bundles 3. Maximize Number of Tube Layers per Sub-bundle
Maximize Effectiveness	1. Maximize Number of Manifolds 2. Maximize Number of Sub-bundles 3. Maximize Number of Tube Layers per Sub-bundle 4. Maximize Number of Loops in Bundle

Based on Table 4-1, the longitudinal and transverse pitch-to-diameter ratios, the tube outer diameter, the number of tubes per layer per sub-bundle, and the inner radius of the tube bundle have the least effect on the pressure drops and effectiveness. However, they all still have a linear relationship with the bundle diameter and/or bundle height, therefore they should be minimized. Since the minimum value for S_L is 1.25 and the FHR CTAH had a value of 1.256, this parameter was fixed at S_L=1.256. In order to minimize vertical flow in the tube bundle and large pressure gradients along the plates separating bundle, the vertical and diagonal pitches between tubes need to be equal. In order for this to occur, the pitch-to-diameters need to have the following relationship: $S_T = \frac{S_L}{\cos(30°)}$. Since S_L is fixed at 1.256, S_T is fixed at 1.45. In order to restrict their size while having a reasonable bundle layout, the number of tubes per layer per sub-bundle were restricted between 3 and 7. The tubes also should remain small, so they were limited to outer diameter values between 3/16" and 1/2". Each one of these tube diameters have different tube wall thickness available. The tube wall thickness' effect on the effectiveness and gas pressure drop is negligible. However, a thicker tube wall means a greater liquid pressure drop, so the optimization code will use the minimum thickness necessary. The tube thickness is based on the pressure difference between the shell-side gas and the tube-side liquid. Based on

this pressure difference, the optimization tool uses the ASME Boiler and Pressure Vessel Code (BPVC) Section VIII, Division 1. The code uses the method presented in Paragraph UG-28: *Thickness of Shells and Tubes Under External Pressure* to estimate the minimum thickness required for the given pressure differential [57].

Even though the bundle inner radius is not one of the more influential parameters, it still has a significant effect on the diameter of the vessel. Equation 4-3 shows how it contributes to the bundle outer diameter. However, the vessel will be designed so that the gas flow area inside the bundle is equal to flow area outside of the bundle. By setting the flow areas equal, Equation 4-3 is derived for the radius of the pressure vessel.

$$R_{vessel} = \sqrt{{R_{in,bund}}^2 + {R_{out,bund}}^2} + t_{vessel} \quad \text{4-3}$$

In this equation, t_{vessel} represents the thickness of the vessel wall. This thickness is found using Equation 4-4, which comes from Paragraph UG-27: *Thickness of Shells Under Internal Pressure* of the ASME BVPC Section VIII, Division 1 [57].

$$t_{vessel} = \frac{P_g R_{vessel}}{S_{vessel} E - 0.6 P_g} \quad \text{4-4}$$

In this equation, P_g represents the internal pressure inside the CTGH pressure vessel and E represents the weld factor of the vessel, which is assumed to be ideal and is set equal to 1. The maximum allowable stress of the vessel, S_{vessel}, is a temperature dependent property of the vessel material. The code uses the maximum allowable stress specified for 316 stainless steel in ASME BVPC Section II, Part D: Properties (Metric) [58].

The range of values for the bundle inner radius can be constrained further given the restrictions on the vessel diameter. First, a restriction was placed on the minimum width of the tube bundle. This would ensure that the CTGH pressure vessel was not made up of just empty space and that the tube bundle took up a reasonable portion of the pressure vessel. Equation 4-5 gives the radius of the tube bundle where the minimum width of the tube bundle is a percentage, $x_{vess,min}$, of the pressure vessel radius.

$$R_{out,bund} = R_{in,bund,max} + x_{vess,min} R_{vessel} \quad \text{4-5}$$

Since this equation uses the minimum bundle width, the inner bundle radius will be the maximum allowable value for a given vessel size. Plugging Equation 4-5 into Equation 4-3, substituting $R_{in,bund,max}$ for $R_{in,bund}$, and solving for the maximum inner bundle radius gives Equation 4-6.

$$R_{in,bund,max} = \frac{1}{2}\left(\sqrt{-\left(x_{vess,min} R_{vessel}\right)^2 + 2{R_{vessel}}^2 - 4R_{vessel} t_{vessel} + 2{t_{vessel}}^2} - x_{vess,min} R_{vessel}\right) \quad \text{4-6}$$

This value becomes the new maximum allowable inner bundle radius, and the optimization tool selects a random value between the original minimum value and this new maximum value.

After the tool selects a value for the inner radius bundle, it can set limits on the width of the bundle itself. Using Equation 4-3 and the chosen $R_{in,bund}$, the maximum bundle width is given by Equation 4-7. The minimum bundle width, Equation 4-8, is the bundle width constraint used for Equation 4-5.

$$w_{bund,max} = \sqrt{(R_{vess} - t_{vessel})^2 - R_{in,bund}{}^2} - R_{in,bund} \quad 4\text{-}7$$

$$w_{bund,min} = x_{vess,min} R_{vessel} \quad 4\text{-}8$$

These equations can be used to put the final constraints on the two remaining input variables, $N_{Manifolds}$ and N_{loops}, in Equation 4-3. Optimizing these two variables gives Equation 4-10 for the minimum allowable values and Equation 4-9 for the maximum allowable values. Since these are discrete variables, the minimum values were rounded up to the nearest integer and the maximum values were rounded down to the nearest integer. If one of the maximum values is less than its respective minimum value, the code decreased the inner radius or went down a tube size until the maximum value was greater than or equal to the minimum value. Finally, the code randomly selected an integer value for each input parameter within its respective range.

$$N_{Manifolds,Max} = N_{loops,max} = \sqrt{\frac{w_{bund,max} - N_{gap} * t_{gap}}{2 * N_{rows} * S_L * D_o}} \quad 4\text{-}9$$

$$N_{Manifolds,Min} = N_{loops,min} = \sqrt{\frac{w_{bund,min} - N_{gap} * t_{gap}}{2 * N_{rows} * S_L * D_o}} \quad 4\text{-}10$$

Next, the code needed to choose values for the final two input variables, $N_{bundles}$ and N_{layers}. Using the previously selected inputs variable and a maximum tube bundle height, $H_{bund,max}$, specified by the user, the code constrained these input variables further. The code used Equation 4-4 to optimize these two input variables to find their maximum allowable values, which are given in Equation 4-11 and Equation 4-12. As with the previous two input variables, these input parameters were discrete values, so the maximum values were rounded down to the nearest integer. The code did not specify a minimum height requirement for the tube bundle, so the original minimum values were used. If one of the maximum values was less than its respective minimum value, the tool decreased the tube size until the maximum value was greater. Finally, the optimization tool randomly chose values for $N_{bundles}$ and N_{layers} within their

respective constraints. Then, the optimization tool ran the 0-D model, recorded the output, and repeated the process 10,000 times. The optimal design was then chosen from the different outputs based on the calculated effectiveness and pressure drops.

$$N_{bundles,max} = \sqrt{\frac{2 * H_{bund,max}}{S_T * D_o}} \quad 4\text{-}11$$

$$N_{layers,max} = N_{bundles,max} - 1 - \frac{t_{disk}}{S_T * D_o} \quad 4\text{-}12$$

4.3 Applications of Optimization Tool

The optimization tool helped develop the Mk1 PB-FHR CTAH design given in Chapter 2. This tool can also be used for other reactor designs and applications. This section gives various examples where the CTGH can be incorporated and uses the optimization tool to find an optimal design for that application.

4.3.1 Sodium to S-CO_2 CTGH Design

Using liquid sodium as a reactor coolant offers many benefits, such as low operation pressure, high-power density, and low corrosion. Since sodium does not readily moderate or absorb neutrons, sodium-cooled reactors operate in the fast neutron spectrum. This means nuclear waste that has high burn-up and contains minor actinides can be reprocessed as fuel for the reactor. This would ideally close the fuel cycle and reduce existing nuclear waste. For this reason, the Sodium Fast Reactor (SFR) was also selected by the GIF as an advance reactor design that could be used in the future [59]. One of the greatest challenges with the SFR design is coupling it with a power generation cycle due to sodium's chemical reactivity. With a steam Rankine cycle, sodium cannot come into contact with the water or it will explode. With an air Brayton cycle, sodium burns when it comes into contact with air. In order to reduce these risks, there is a proposal to couple the SFR with a supercritical carbon dioxide (S-CO_2) Brayton cycle, which has been optimized to be coupled with the SFR. The recompression in the cycle is highly recuperated, and the cycle operates well at the optimal temperature rise across the SFR core (~150 °C). However, in order to keep the carbon dioxide in a supercritical state and at the optimal conditions for use in the Brayton cycle, the temperature needs to be between 360-530°C and the pressure needs to be approximately 200 bar. Due to the relatively high temperature and pressure of the system, the CTGH could possibly be used as the primary heat exchanger to couple these fluids. The AFR-100, a 100 MWe SFR developed at Argonne National Laboratory, was chosen as the base design. The SFR to S-CO_2 CTGH would be based on the temperatures, flowrates, and physical requirements for this reactor design [60]. These fluid parameters, which are given in Table 4-2, were used as the input for the optimization tool to develop the optimal SFR to S-CO_2 CTGH.

Table 4-2. AFR-100 Fluid Parameters [60]

Inlet Parameter	**Sodium**	**S-CO_2**
Temperature	528.0ºC	367.0ºC
Pressure	3.50 bar	199.5 bar
Mass Flow Rate	1267 kg/s	1360.5 kg/s

Originally, the constraints placed on the optimization code were that the vessel would have a maximum diameter of 4 meters and the bundle would have a maximum height of 8 meters so that the CTGH would be rail transportable. However, a design could not be found using these restrictions. One of the greatest challenges for this reactor design was using sodium as a coolant. It has a high viscosity, which leads to significant head loss when flowing through the small tubes. This is exasperated further by the high-pressure S-CO_2. With a pressure difference of almost 200 bar, the tube walls and pressure vessel walls need to be significantly thick, limiting the size of the tube bundle and greatly increasing the sodium head loss. One advantage of sodium, though, is that is has a relatively low melting point of ~98ºC. This means that fewer electrically heated rods are needed to prevent the sodium from freezing during shutdowns. This bundle was assumed to have 1 heating rod every 4 tube layers. In order to overcome the large pressure loss on the tube side, the constraints were expanded to a 6-meter diameter pressure vessel and 15-meter tall tube bundle. With these new constraints, the optimization tool found the CTGH design described in Table 4-3. This geometry was then used as input for THEEM, giving the results shown in Table 4-4.

Table 4-3. AFR-100 CTGH Geometry

Tube Outer Diameter	0.635 cm (0.25 in)
Tube Wall Thickness	0.1651 cm (.065 in)
Longitudinal Pitch-to-Diameter Ratio (S_L)	1.256
Transverse Pitch-to-Diameter Ratio (S_T)	1.45
Number of Liquid Manifolds	5
Number of Loops	4
Number of Tubes per Layer per Manifold	6
Number of Tube Layers per Sub-bundle	50
Number of Sub-bundle	53
Number of Tie Rod Gaps	2
Width of Tie Rod Gaps	3.80 cm
Number of Tube Holders	12
Annulus Inner Radius	26.3 cm
Tube Slope	0.003
Heating Rods per Tube Layer	1/4

Table 4-4. THEEM Prediction for AFR-100 CTGH

Effectiveness	0.9725
F-factor	0.8175
Estimated Total Heat Transfer	251.2 MW
Sodium Mean Outlet Temperature	371.6ºC
Sodium Pressure Drop	1.94 bar
S-CO_2 Mean Outlet Temperature	512.4 ºC
S-CO_2 Pressure Drop	0.0195 bar
Bundle Outer Diameter	4.51 m
Vessel Outer Diameter	5.59 m
Bundle Height	12.6 m

Given the constraints of a high pressure supercritical fluid, it does not seem possible to keep the CTGH rail transportable. However, it is possible to obtain a heat transfer of 250 MW and still meet ASME BVPC standards. This heat exchanger has a high effectiveness, though its geometry does not approximate a counterflow heat exchanger too well as indicated by its F-factor. The sodium pressure loss of 1.94 bar is a reasonable head loss given the small tube size that means that the pump for the sodium loop does not need to be oversized. The supercritical carbon dioxide encounters a 0.00977% pressure loss, so there will be little efficiency loss in the S-CO_2 Brayton cycle. Overall, this heat exchanger is oversized, but given the difficult requirements of this application, the CTGH can deliver the desired effectiveness while keeping friction losses minimal.

4.3.2 370 kWt CTAH Test Loop Design

The previous chapter discussed experimental work with the CTGH using water and air as the heat transfer fluids. Even though THEEM can simulate high temperature applications and the calculations use non-dimensional numbers that allow for scaling, there are still practical applications to studying how the design operates with molten salt at the higher temperatures expected in a molten salt reactor. A 370 kWt CTAH test loop was proposed in a previous conference paper that used molten flinak as a coolant coupled with an air loop [61]. The air loop design was based on the RACC design coupled with the Mk1 PB-FHR [10], [11]. Unlike the FHR, the salt would be heated by an electric heater, and instead of running through a gas turbine, the air would run through a steam generator to cool it off. Since this was only a test loop, it was not designed to generate electricity. Though, this loop was designed to have some similarities to the RACC, which included operating at similar temperatures (~420ºC) and pressures (~5 bar), enabling demonstration of salt-to-air heating under the same conditions as the RACC. Table 4-1 shows the nominal parameters for the CTAH in this test loop.

Table 4-5. Test Loop CTAH Fluid Parameters [61]

Inlet Parameter	Flinak Salt	Air
Temperature	536.2ºC	420ºC
Pressure	3.50 bar	4.5 bar
Mass Flow Rate	12.52 kg/s	3.052 kg/s

It should be noted that this paper already included a CTAH design. However, this example provided a great opportunity to see if the optimization code could provide a more optimal design. The original geometry for this application was designed for observability and maintenance. The optimization tool developed a design based on minimizing pressure losses. The optimized CTGH geometry is given in Table 4-6, and the THEEM results for this geometry is given Table 4-7. Since the heat transfer is relatively small, the CTGH needed to be more compact so that it would not overcool the salt, which could lead to freezing. If it was too compact, the pressure losses would make the design impractical. This gave a design with a vessel diameter just under 1 meter and a bundle height of about 2.5 meters. This design gives a relatively small head loss of 0.0979 bar for the flinak salt. The air also sees only a 0.0064% pressure drop, which would mean an almost negligible circulating power loss if there was a turbine. For the CTAH design in the paper, the bundle diameter is much larger at 1.252 meter, but the bundle height is much smaller at 0.363 m. This means the new design has a 152% increase in volume, but this new design does show improvement with pressure losses. For approximately the same effectiveness, the new design has an 85% reduction in flinak head loss and a 95% reduction in air pressure loss. Even with the volume increase, the new design remains relatively small and well within rail transportable parameters, so overall, the new geometry can be seen as an improvement in the design.

Table 4-6. Test Loop CTAH Geometry

Tube Outer Diameter	0.635 cm (0.25 in)
Tube Wall Thickness	0.0889 cm (.035 in)
Longitudinal Pitch-to-Diameter Ratio (S_L)	1.256
Transverse Pitch-to-Diameter Ratio (S_T)	1.45
Number of Liquid Manifolds	2
Number of Loops	2
Number of Tubes per Layer per Manifold	2
Number of Tube Layers per Sub-bundle	32
Number of Sub-bundle	16
Number of Tie Rod Gaps	0
Width of Tie Rod Gaps	N/A
Number of Tube Holders	12
Annulus Inner Radius	25.3 cm
Tube Slope	0.003
Heating Rods per Tube Layer	1/2

Table 4-7. THEEM Prediction for Test Loop CTAH

Effectiveness	0.9437
F-factor	1.00
Estimated Total Heat Transfer	363.6 kW
Flinak Salt Mean Outlet Temperature	520.3ºC
Flinak Salt Pressure Drop	0.0979 bar
Air Mean Outlet Temperature	529.7 ºC
Air Pressure Drop	0.000286 bar
Bundle Outer Diameter	0.761 m
Vessel Outer Diameter	0.918 m
Bundle Height	2.48 m

4.3.3 TMSR-SF1 CTGH Design

Similar to UCB, the Shanghai Institute of Applied Physics (SINAP) has been working on developing FHR technology for future commercialization. They specifically focused on developing the Thorium-based Molten Salt Reactor nuclear energy system (TMSR). One of their goals was to build the TMSR-SF1, a prototypical 10 MWt molten salt test reactor that uses solid pebble fuel like the FHR. The core is a pebble bed, which consists of graphite fuel pebbles containing TRISO particles, that is cooled by molten flibe salt. Unlike the FHR, the primary loop, which contains the flibe, is cooled by secondary loop filled with molten flinak salt to act as a barrier to fission product and tritium release. This secondary loop is then cooled by a salt-to-air heat exchanger. A diagram of the TMSR-SF1 is shown in Figure 4-21. [62]

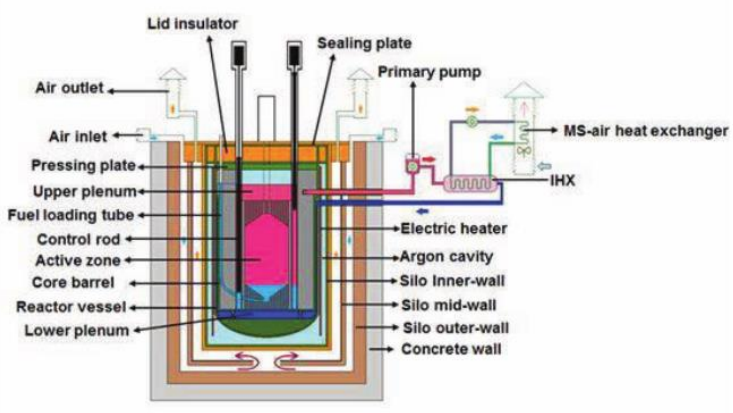

Figure 4-21. Diagram of SINAP's TMSR-SF1 [62]

Since this is a test reactor, it will not be used to produce electricity; the salt-to-air heat exchanger only needs to remove heat from the reactor. The original design has a basic heat exchanger that utilizes non-compressed air from the atmosphere to cool the secondary loop. There are no large pressure differences as in the FHR, the 10 MW heat transfer is relatively small, and since the air does not flow through a turbine, minimizing the air pressure loss is not a

major concern. There may not be much advantage to using the CTGH design for this application, but it can be used as another demonstration of the optimization tool and of the advantages of the CTGH design. Table 4-8 gives the nominal parameters for the TMSR-SF1 salt-to-air heat exchanger.

Table 4-8. TMSR-SF1 CTGH Fluid Parameters [63]

Inlet Parameter	Flinak Salt	Air
Temperature	630.0ºC	40.0ºC
Pressure	3.50 bar	1.01325 bar (1 atm)
Mass Flow Rate	260.0 kg/s	51.0 kg/s

Originally, the optimization tool could not find an optimal geometry for this application. This was partly attributed to the high effectiveness of the general CTGH design. Since the original heat exchanger was not designed to have a high effectiveness, the tool found designs that overcooled the salt, which would lead to freezing issues. Eventually, the original constraints were modified in order to obtain a less effective design. The minimum inner bundle radius constraint was decreased to 15 cm. With a high salt flow rate and a smaller bundle, the tube diameter was also increased to 3/8". Then, due to the small heat transfer, the diameter and height constraints were reduced to 2 meters each. With these new constraints, the optimization tool found the geometry in Table 4-9. The results for this geometry, shown in Table 4-10, demonstrate that given the inlet parameters, the heat exchanger needed a low effectiveness of 0.3405 in order to not cool more than 10 MW. This design still has a realistic flinak pressure loss of 1.89 bar. The air pressure loss was relatively high at 89.0%, but since it does not flow through a turbine, air pressure loss is not a major concern for this design. Overall, this example demonstrates that the CTGH design may be too effective or expensive for some applications, but it is still possible to develop a design for even smaller reactors or salt loops.

Table 4-9. TMSR-SF1 CTGH Geometry

Tube Outer Diameter	0.9525 cm (0.375 in)
Tube Wall Thickness	0.0889 cm (.035 in)
Longitudinal Pitch-to-Diameter Ratio (S_L)	1.256
Transverse Pitch-to-Diameter Ratio (S_T)	1.45
Number of Liquid Manifolds	2
Number of Loops	2
Number of Tubes per Layer per Manifold	2
Number of Tube Layers per Sub-bundle	12
Number of Sub-bundle	9
Number of Tie Rod Gaps	1
Width of Tie Rod Gaps	3.80 cm
Number of Tube Holders	6
Annulus Inner Radius	15.9 cm
Tube Slope	0.003
Heating Rods per Tube Layer	1/2

Table 4-10. THEEM Prediction for TMSR-SF1 CTGH

Effectiveness	0.3405
F-factor	0.9752
Estimated Total Heat Transfer	10.41 MW
Flinak Salt Mean Outlet Temperature	609.2ºC
Flinak Salt Pressure Drop	1.89 bar
Air Mean Outlet Temperature	240.6 ºC
Air Pressure Drop	0.9015 bar
Bundle Outer Diameter	0.777 m
Vessel Outer Diameter	0.8402 m
Bundle Height	0.8350 m

4.3.4 TMSR-SF0 CTGH Design

Before SINAP builds the TMSR-SF1, they plan to build the TMSR-SF0, a 1-MW electrically heated salt loop. The TMSR-SF0 will serve as a prototype for the TMSR-SF1 by testing key technologies and components that will be used in the SF1. It will be possible to simulate various accident conditions of the reactor to analyze safety procedures without the risk or cost of using nuclear fuel. It also will act as a training platform for the construction, operation, and maintenance of the SF1. Similar to the SF1, the SF0 will have a primary loop containing molten salt that transfers heat to a secondary salt loop that is then cooled by air. Unlike the SF1, since the neutronics of the primary coolant is not a concern, flinak will be used in the primary loop. However, the secondary loop and third loop will still use flinak salt and air, respectively, like the SF1. The air loop will also be at atmospheric pressure and have a relatively low flow rate since it is only used to cool the salt and not to produce electricity. The nominal parameters for the salt-to-air heat exchanger are given in Table 4-11. [64]

Table 4-11. TMSR-SF0 CTGH Fluid Parameters [64]

Inlet Parameter	**Flinak Salt**	**Air**
Temperature	694.7ºC	40ºC
Pressure	0.40 bar	1.01325 bar (1 atm)
Mass Flow Rate	112.5 kg/s	4.38 kg/s

Similar to the SF1, the optimization tool had difficulty finding a CTGH design that would not overcool the flinak salt. The minimum number of liquid manifolds was lowered to 1 manifold, the minimum inner bundle radius was lowered to 15 cm, and the maximum tube diameter was expanded to ¾". With the user constraints set to a maximum 1-meter bundle diameter and 1-meter bundle height, the optimization tool found the geometry shown in Table 4-12. The THEEM results for this geometry is given in Table 4-13. Like the SF1, this design has a very low effectiveness and small volume due to the low 1.0 MW heat transfer. This bundle design gives better pressure drops than the SF1 design. The flinak salt only has 0.160 bar head loss, and the air only has 0.326 % pressure loss. Even though the CTGH is not the optimal

choice for this application, this example still demonstrates that this optimization tool and the CTGH can be used for a variety of applications.

Table 4-12. TMSR-SF0 CTGH Geometry

Tube Outer Diameter	1.905 cm (0.75 in)
Tube Wall Thickness	0.1245 cm (.049 in)
Longitudinal Pitch-to-Diameter Ratio (S_L)	1.256
Transverse Pitch-to-Diameter Ratio (S_T)	1.45
Number of Liquid Manifolds	1
Number of Loops	2
Number of Tubes per Layer per Manifold	2
Number of Tube Layers per Sub-bundle	10
Number of Sub-bundle	5
Number of Tie Rod Gaps	0
Width of Tie Rod Gaps	N/A
Number of Tube Holders	6
Annulus Inner Radius	20.0 cm
Tube Slope	0.003
Heating Rods per Tube Layer	1/2

Table 4-13. THEEM Prediction for TMSR-SF0 CTGH

Effectiveness	0.3509
F-factor	0.9875
Estimated Total Heat Transfer	1.024 MW
Flinak Salt Mean Outlet Temperature	690.2ºC
Flinak Salt Pressure Drop	0.160 bar
Air Mean Outlet Temperature	269.5 ºC
Air Pressure Drop	0.00330 bar
Bundle Outer Diameter	0.783 m
Vessel Outer Diameter	0.880 m
Bundle Height	0.775 m

4.4 Concluding Remarks on Optimization Tool

As the examples in this chapter have shown, the optimization tool can be used for a variety of applications. Even if the CTGH design is not the most practical heat exchanger for a given application, it can be redesigned to be a somewhat practical option. The optimization tool may also require some future work. It may be necessary to improve the algorithm or use a different one, like a genetic algorithm, to make the tool more efficient. For now, this algorithm is still a relatively effective tool for developing new CTGH geometries.

Chapter 5.
Conclusions and Recommendations

With increasing population size and industrialization around the world, sources of clean, carbon-free energy will be essential to protecting the environment and ensuring a high quality of life globally. Nuclear power is a clean, carbon-free source of energy that can supplement intermittent renewable sources of electricity, like solar and wind, with baseload energy. Advances in nuclear reactor technology have decreased the cost of future nuclear power plants, produced safer and more robust designs, and created reactors designs that can be deployed in more areas due to smaller generating capacities. In particular, the Mk1 PB-FHR design operates at much lower pressures than conventional LWRs and incorporates passive safety systems to further reduce the risk of accidents. Due to its small size, these reactors can be constructed and shipped almost anywhere to meet both large and small demand for electricity. The development of this newer technology led to the development of new components for this design. Specifically, the FHR required a primary heat exchanger that was compact enough to fit on a rail car, could operate at high temperatures, could handle the large pressure differential between the two heat transfer fluids, and could sustain multiple thermal transients over the lifetime of the heat exchanger. For these reasons, CTAH was chosen as primary heat exchanger design for the FHR. With its high heat transfer surface area density, its relatively low pressure drops, and its high effectiveness, the CTAH proved to be an optimal choice for coupling the FHR with the RACC.

Since there was little experience in fabricating CTGHs, there needed to be a process to design the CTAH so that it delivered the desired heat transfer between the flibe and air. For the overall reactor design, it was also necessary to know what pressure drops to expect across the heat exchanger. Since the CTAH could not easily be modeled using CFD or a commercial modeling software due to its large geometry, the THEEM code was developed. This code used an unconventional approach involving the finite volume method to model the CTAH. Unlike other finite volume codes, the calculations were not based off governing differential equations for fluid flow and heat transfer, such as the continuity equation, Navier-Stokes, and the Heat Equation; the calculations were based on empirical correlations. Using empirical correlations not only simplified the calculations, it also reduced the number of calculations, creating a faster and more computationally efficient program. Since the empirical correlations were used for specific geometry, THEEM generated volumes that were large enough to encompass geometry that could be modeled by these empirical correlations. For example, it was shown in Chapter 2 that in order to model the shell-side using the Zukauskas correlation for a tube bundle in crossflow, the volumes needed to be large enough to encompass multiple tubes in cross-flow. Using larger volumes meant that fewer volumes were generated and that the code ran in a fraction of the time compared to a conventional CFD or modeling code. For the CTAH geometry, a conventional code could take multiple hours to a couple of days to run if it could even handle the geometry. On the other hand, the 2-D THEEM code could simulate the same conditions and perform all calculations in approximately 5 to 10 minutes, and the 3-D THEEM code could perform all calculations in a few hours. The 3-D code would give a more thorough model of the CTGH outlet conditions, but as Chapter 2 showed, the 2-D code was a reliable

approximation. Also, since the code was specifically made for the CTGH design, the input file required less information and was easier to modify to reflect changes in geometry. Since it was easy to modify the geometry and the program did not take long to run, THEEM could be used to test multiple designs with minimal time and effort, making it an excellent design tool for both the FHR and other nuclear applications.

In Chapter 2, an optimal CTAH design was found for the Mk1 PB-FHR. First, this design was small enough that it could be shipped by rail. Then, each heat exchanger would transfer approximately 116 MW of heat from the salt to the air. Finally, the salt pressure drop was small enough that the primary pump would not need to be oversized, and the air pressure drop would not greatly decrease the efficiency of the Brayton cycle. THEEM also had applications other than calculating the outlet conditions for the CTAH. For example, since THEEM found the distributions of temperature and convection coefficients for both fluids across the bundle, it was able to find the tube wall surface temperatures across the bundle. This was important to ensure that there was no localized coolant freezing in the heat exchanger. THEEM found that in the Mk1 FHR CTAH, the tube walls stayed well above the freezing point of flibe, so salt freezing would not be an issue under normal operation. Next, the temperature distributions calculated by THEEM could also be used for structural analysis. Chapter 1 discussed the need for a heat exchanger that could handle the thermal transients expected over the lifetime of the reactor. The temperature data from THEEM could be used to perform a thermal stress analysis for the tube bundle. This would then either confirm that the CTAH would work over the lifetime of the reactor or would show where the design needed to be improved. Another application of THEEM is tube mechanical vibration analysis. As with any shell-and-tube heat exchanger, flow induced tube vibration was a major concern since it could lead to tube damage and possible rupture. THEEM's calculations included calculating the flow velocity on the shell side, which could then be compared with the critical flow velocities for the tubes. Based on this data, the number of anti-vibration rods could be increased or the bundle could be redesigned to reduce risk of damage from flow-induced vibrations. Since THEEM performs many calculations to model the tube bundle, it is possible that there are more applications for this code to improve the heat exchanger's design. All of these different applications, its speed, and its ability to model different geometries makes THEEM a powerful tool to model and improve the CTGH designs for different nuclear Brayton cycles.

Using THEEM could make the CTGH design process quicker and cheaper, but, before it could be used as a design tool for large scale heat exchangers, it was necessary to compare the simulation results with physical measurements. Chapter 3 focused on performing experiments primarily to validate THEEM. Since THEEM's calculations were based chiefly on correlations that used dimensionless numbers, it was possible to use small scale experiments to validate the code. The first experiment was built as a proof of concept for the CTGH bundle, so it was not built to match the Mk1 PB-FHR CTAH dimensionless numbers, such as Reynolds and Nusselt numbers. However, the second experiment, CASET, was built specifically for THEEM validation and was designed so that it could match the Reynolds numbers expected on both the tube and shell side of the Mk1 PB-FHR CTAH. Due to the poor construction of the first experiment, it could not provide accurate data for validating THEEM. However, CASET was able to provide some data that helped validate THEEM. The initial validation efforts indicated

that THEEM could accurately predict temperature changes and, consequently, the effectiveness of the bundle, but the pressure drop calculations needed to be reexamined. Future work will need to address this error in pressure drop predictions. Given bypass flow was observed in the experiments, the CASET experiment needs to be modified so that the vessel and the tube bundle have a tighter seal to prevent bypass flow from occurring. This may affect the pressure drop measurements so that it matches more closely with THEEM's predictions.

CASET also offered the opportunity to perform other experiments to study the CTGH design, such as measuring flow maldistribution through the bundle, developing empirical correlations for the CTGH, and measuring the response of the bundle to power impulses. Measurements of the airflow distribution were taken to study the flow maldistribution through the tube bundle. With the construction of another tube bundle, it would be possible to study how different fabrication methods affect flow maldistribution through the CTGH bundle. These results could then be incorporated into THEEM to more accurately model how flow maldistribution affects the overall effectiveness of the heat exchanger. Next, using the Wilson plot method provided a new set of convection coefficient correlations for CTGHs. For the shell-side, the derived correlation could apply to a large range of gases with different Reynolds and Prandtl numbers. Since there appeared to be few resources on Nusselt number correlations for gases flowing through coiled tubes, this would be a useful correlation for future modeling efforts. For the tube-side, since the original correlation only applied to a relatively small range of Prandtl numbers and curvature ratios, more experiments would need to be performed with different fluids and with different curvatures to show that this correlation could apply to a larger range of geometries and Prandtl numbers. The correlations also varied from the predicted theoretical models, so further experiments will need to be performed for these correlations to be used reliably. Finally, the impulse response measurements did not provide much new data other than measuring the residence times of the water in the bundle and CASET loop. However, it did provide a foundation for performing future experiments to model how the heat exchanger responds to changes in power and flow. With relatively minor modifications to CASET's power supply and control system, the experiment could easily model accident scenarios in the FHR and measure how the heat exchanger behavior changes. These results could then be used in system modeling codes, such as RELAP, or they could be incorporated into integral effects tests modeling the FHR, such as CIET.

The primary takeaway from Chapter 4 was that the heat exchanger could be used in different nuclear reactor designs coupled with Brayton cycles. It also showed that the optimization tool made THEEM a more powerful design tool for CTGHs. The optimization algorithm can be improved so that it more efficiently finds new CTGH geometries based on more restrictive design constraints, but, for now, it reduces the time and effort for developing a new CTGH design. This tool and the examples in Chapter 4 show that not only does the CTGH design have a diverse range of applications; it shows that THEEM is an excellent tool that can be used to improve the CTGH design process.

5.1 Future Work

As discussed earlier in this chapter, there are possible improvements to the work already performed. For example, there will need to be more experiments to fully study the CTGH design. In order to use CASET for future experiments, it will need to be upgraded. First, the vessel around the bundle will need to be modified to eliminate air bypass flow in order to more accurately measure pressure drops and heat transfer across the bundle. The water loop also will need to be modified in order to eliminate bubbles in the line that may be distorting the pressure drop measurements. Finally, it would be possible to perform frequency response experiments and simulate accident scenarios on CASET with some further additions. These include adding an adjustable power supply for the water heater, installing digital flowmeters on both the water and air loops, and adding a control system for the heater power supply, fan VFD, and pump VFD. Another possibility for future experiments is to fabricate another tube bundle. This could involve either building a new experimental setup or modifying CASET to have interchangeable tube bundles. The new tube bundle could be used to collect more experimental data to validate THEEM. If another fabrication method is used, there can be a comparison of the different methods and their effects on flow maldistribution. This will also help determine which method should be used for large scale production of the heat exchanger. If the heat exchanger is fabricated with different radii of curvature, more experiments could be performed using the Wilson plot method. This would expand the range of applicability based on geometry for the empirical correlations found in Chapter 3. If a new experimental setup is used with different fluids, the range of applicability based on the Prandtl number could be expanded as well. With a larger range of applications, these empirical correlations can used to model the CTGH under any reactor conditions, especially in system modeling codes like RELAP.

Other improvements than can be made to the work already performed is to further develop THEEM and the optimization tool. First, it will be important to calculate the uncertainty from the simulation calculations. This can include the error and uncertainty from the materials data and the empirical correlations as well as the propagation of those errors through THEEM's calculations. Another source of error could be the mesh size generated by THEEM's algorithm. Future work should include a sensitivity analysis of how the mesh size affects the overall results. It should be note that the experiments already performed do indicate some error in the pressure drop calculations. If the new or modified experiments give pressure drop results that do not match THEEM's predictions, it may be necessary to modify either the friction factor correlations or the pressure drop equations. Next, based on the results of future airflow distribution measurements, it may be possible for THEEM to predict flow maldistribution through the bundles. The spacing in the tube bundle geometry is similar to a porous material, so the gas flow through the bundle could be modeled as fluid flow through anisotropic porous media. This would give a more accurate model of flow, pressure drop, and even heat transfer across the tube bundle. Finally, the optimization tool could be improved by using a different algorithm. The current Monte Carlo algorithm gave optimal designs within the given constraints, but it also gave many designs that would not work. Depending on the design, it required modifying the constraints to narrow the results for a design. In the future, the optimization tool could use a genetic algorithm to modify the design until it met the original requirements without input from

the user. All of this work would improve THEEM as a design tool and make it a more efficient and accurate program.

In order for the CTGH design to be used in reactors, like the FHR, there will need to be work performed outside the scope of this dissertation. Fortunately, the work described in this thesis can be used to complete some of this work. As discussed earlier, the temperature distribution in the CTGH from THEEM can be used to as an input for a stress analysis. This analysis will help improve the design and, if necessary, reduce the number of stress concentrations and the risk of damage to the CTGH bundle over its lifetime. THEEM can also be used to estimate the gas velocity at different locations around the tube bundle, so that it can be used to identify and model any flow-induced tube vibration. This will be necessary to reduce the risk of damage or failure from mechanical tube vibrations under normal operating conditions. Next, current work on developing the optimal method for joining the tubes to the manifolds will continue [23], [24]. These joints are one of the few possible points of stress concentration in the CTGH design. If they are not joined using the proper technique, these tube-to-tube sheet joints could fail at some point over the lifetime of the reactor. However, there is continuing research on the effects of stress and creep on sample tube-to-tube sheet joints for the CTGH, which is critical for deployment of this heat exchanger design.

The work discussed so far will be applicable for all applications of the CTGH, but some work will specifically benefit the Mk1 PB-FHR CTAH design. For example, since molten salt flibe has a relatively high freezing point and salt freezing could damage various components of the reactor, keeping the salt liquid during any shutdown will be critical. So, the FHR CTAH has electric heating rods replacing tubes in the tube bundle. Further research will find the minimal number of heater rods to keep the flibe liquid during a shutdown, which will reduce the cost and improve the heat exchanger effectiveness. As with many shell-and-tube heat exchangers, tube fouling is also a concern in the FHR CTAH. Since tube fouling from the air or the molten salt can decrease the effectiveness over time and increase the pressure drops, it will be necessary to find the rate of tube fouling over time. This will determine how well the heat exchanger will operate over the lifetime of the plant and if it may be more cost efficient to replace it before the end of the plant's life. The final step will be a cost analysis of the CTAH. Once a fabrication method has been chosen for the CTAH, the costs can be calculated for fabrication and installation. This will help determine if the CTAH should be replaced multiple times over the reactor lifetime or if it should be designed to last the entire lifetime. All of this work will help to create a safer, more robust, and more optimal CTAH design.

References

[1] International Energy Agency, “Key World Energy Statistics,” 2017.

[2] International Energy Agency, “World Energy Outlook,” 2017.

[3] T. Jasarevic, G. Thomas, and N. Osseiran, “7 million premature deaths annually linked to air pollution,” *World Health Organization*, 25-Mar-2014.

[4] “Nuclear Power in the USA,” *World Nuclear Association*, 2018. [Online]. Available: http://www.world-nuclear.org/information-library/country-profiles/countries-t-z/usa-nuclear-power.aspx. [Accessed: 28-Mar-2018].

[5] “Generation IV Nuclear Reactors,” *World Nuclear Association*, 2017. [Online]. Available: http://www.world-nuclear.org/information-library/nuclear-fuel-cycle/nuclear-power-reactors/generation-iv-nuclear-reactors.aspx. [Accessed: 28-Mar-2018].

[6] C. H. Gabbard, “Reactor Power Measurement and Heat Transfer Performance in the Molten Salt Reactor Experiment (ORNL-TM-3002),” Oak Ridge National Laboratory, 1970.

[7] P. N. Haubenreich and J. R. Engel, “Experience with the Molten-Salt Reactor Experiment,” *Nucl. Appl. Technol.*, vol. 8, no. 2, pp. 118–136, Feb. 1970.

[8] C. Andreades *et al.*, “Mark--1 PB--FHR Technical Description Technical Description of the ‘Mark 1’ Pebble-Bed Fluoride-Salt-Cooled High-Temperature Reactor (PB-FHR) Power Plant,” Berkeley, CA, 2014.

[9] C. Andreades *et al.*, “Design Summary of the Mark-I Pebble-Bed, Fluoride Salt–Cooled, High-Temperature Reactor Commercial Power Plant,” *Nucl. Technol.*, vol. 195, no. 3, pp. 223–238, 2016.

[10] C. Andreades, R. O. Scarlat, L. Dempsey, and P. Peterson, “Reheat-Air Brayton Combined Cycle Power Conversion Design and Performance Under Nominal Ambient Conditions,” *J. Eng. Gas Turbines Power*, vol. 136, no. 6, p. 62001, Feb. 2014.

[11] C. Andreades, L. Dempsey, and P. F. Peterson, “Reheat Air-Brayton Combined Cycle Power Conversion Off-Nominal and Transient Performance,” *J. Eng. Gas Turbines Power*, vol. 136, no. 7, p. 71703, Feb. 2014.

[12] “Small modular reactors (SMR),” *IAEA*. [Online]. Available: https://www.iaea.org/topics/small-modular-reactors. [Accessed: 03-Apr-2018].

[13] W. M. Kays and A. L. London, *Compact HEat Exchangers*, 3rd ed. New York: McGraw-Hill, 1998.

[14] R. K. Shah and D. P. Sekulić, *Fundamentals of heat exchanger design*. Hoboken, NJ, USA: John Wiley & Sons, Inc., 2003.

[15] V. Ariu, “Heat Exchanger Analysis for Innovative Molten Salt Fast Reactor,” Paul Scherrer Institute, 2014.

[16] S. J. Dewson and B. Thonon, “THE DEVELOPMENT OF HIGH EFFICIENCY HEAT EXCHANGERS FOR HELIUM GAS COOLED REACTORS. (PAPER NO. 3213),” in *International Congress on Advances in Nuclear Power Plants (ICAPP 2003)*, 2003.

[17] E. Urquiza, “Transient Thermal, Hydraulic, and Mechanical Analysis of a Counter Flow Offset Strip Fin Intermediate Heat Exchanger using an Effective Porous Media Approach,” University of California Berkeley , 2009.

[18] P. F. Peterson, H. Zhao, F. Niu, W. Huang, J. Schmidt, and J. Schulte-Fischedick, “Development of C-SiC ceramic compact plate heat exchangers for high temperature heat transfer applications,” in *American Institute of Chemical Engineering Annual Meeting*, 2006.

[19] P. Gilli, K. Fritz, J. Lippitsch, and G. Lurf, “Radial-flow heat exchanger,” US Patent No. US3712370A, 22-Sep-1970.

[20] A. N. Dravid, K. A. Smith, E. W. Merrill, and P. L. T. Brian, “Effect of secondary fluid motion on laminar flow heat transfer in helically coiled tubes,” *AIChE J.*, vol. 17, no. 5, pp. 1114–1122, Sep. 1971.

[21] “Heat Exchangers,” *Reaction Engines*. [Online]. Available: https://www.reactionengines.co.uk/sabre/technology/heat-exchangers/. [Accessed: 05-Apr-2018].

[22] D. K. Williams, D. P. Fassett, Brent J. Webb, W. J. Bees, and A. S. Kruskamp, “Helical coil steam generator,” US Patent No. US20160303694A1, 28-Jun-2016.

[23] N. Haneklaus, R. Reuven, C. Cionea, P. Hosemann, and P. F. Peterson, “Tube expansion and diffusion bonding of 316L stainless steel tube-to-tube sheet joints using a commercial roller tube expander,” *J. Mater. Process. Technol.*, vol. 234, pp. 27–32, Aug. 2016.

[24] N. Haneklaus, C. Cionea, R. Reuven, D. Frazer, P. Hosemann, and P. F. Peterson, “Hybrid friction diffusion bonding of 316L stainless steel tube-to-tube sheet joints for coil-wound heat exchangers,” *J. Mech. Sci. Technol.*, vol. 30, no. 11, pp. 4925–4930, Nov. 2016.

[25] F. Incropera, D. Dewitt, T. Bergman, and A. Lavine, *Introduction to Heat Transfer*, 5th ed. Hoboken, NJ: John Wiley & Sons, 2007.

[26] I. Di Piazza and M. Ciofalo, “Numerical prediction of turbulent flow and heat transfer in helically coiled pipes,” *Int. J. Therm. Sci.*, vol. 49, no. 4, pp. 653–663, Apr. 2010.

[27] R. L. Manlapaz and S. W. Churchill, “Fully Developed Laminar Convection from a Helical Coil,” *Chem. Eng. Commun. Chem. Eng. Commun. Sci. Publ. Inc*, vol. 950, no. 9, pp. 1–6, 1981.

[28] G. F. C. Rogers and Y. R. Mayhew, “Heat transfer and pressure loss in helically coiled tubes with turbulent flow,” *Int. J. Heat Mass Transf.*, vol. 7, no. 11, pp. 1207–1216, Nov. 1964.

[29] A. Žukauskas, “Heat Transfer from Tubes in Crossflow,” in *Advances in Heat Transfer*, vol. 8, Vilnius, USSR: Academy of Sciences of the Lithuanian SSR, 1972, pp. 93–160.

[30] R. L. Manlapaz and S. W. Churchill, “Fully Developed Laminar Flow in a Helically Coiled Tube of Finite Pitch,” *Chem. Eng. Commun.*, vol. 7, pp. 57–78, 1980.

[31] J. B. Haefner, L. B. Carasik, and Y. A. Hassan, “Development and Verification of MATLAB Functions for Pressure Drop Estimation in Crossflow Tube Bundles,” *Trans. Am. Nucl. Soc.*, vol. 115, no. 1, pp. 1535–1537, 2016.

[32] D. F. Williams, L. M. Toth, and K. T. Clarno, “Assessment of Candidate Molten Salt Coolants for the Advanced High-Temperature Reactor (AHTR),” Oak Ridge, TN, 2006.

[33] M. S. Sohal, M. A. Ebner, P. Sabharwall, and P. Sharpe, “Engineering Database of Liquid Salt Thermophysical and Thermochemical Properties,” Idaho Falls, 2010.

[34] R. Serrano-López, J. Fradera, and S. Cuesta-López, “Molten salts database for energy applications,” 2013.

[35] V. Sobolev, “Database of thermophysical properties of liquid metal coolants for GEN-IV,” 2010.

[36] P. M. Bardet, C. S. Debonnel, J. Freeman, G. Fukuda, B. Supiot, and P. F. Peterson, “Dynamics of Liquid-Protected Fusion Chambers,” *Fusion Sci. Technol.*, vol. 47, no. 3, pp. 626–632, 2005.

[37] E. W. Lemmon, M. O. McLinden, and D. G. Friend, “Thermophysical Properties of Fluid Systems,” in *NIST Chemistry WebBook, NIST Standard Reference Database Number 69*, P. J. Linstrom and W. G. Mallard, Eds. Gaithersburg MD: National Institute of Standards and Technology.

[38] J. Wang, “Theory of flow distribution in manifolds,” *Chem. Eng. J.*, vol. 168, no. 3, pp. 1331–1345, 2011.

[39] J. Wang, Z. Gao, G. Gan, and D. Wu, “Analytical solution of flow coefficients for a uniformly distributed porous channel,” *Chem. Eng. J.*, vol. 84, no. 1, pp. 1–6, Sep. 2001.

[40] M. P. Païdoussis, “Fluidelastic vibration of cylinder arrays in axial and cross flow: State of the art,” *J. Sound Vib.*, vol. 76, no. 3, pp. 329–360, Jun. 1981.

[41] H. J. Connors, “Fluidelastic Vibration of Tube Arrays Excited by Cross Flow,” in *Flow Induced Vibration in Heat Exchangers*, 1970, pp. 42–56.

[42] G. W. Hollenberg, E. P. Simonen, G. Kalinin, and A. Terlain, “Tritium/hydrogen barrier development,” *Fusion Eng. Des.*, vol. 28, pp. 190–208, 1995.

[43] J. F. Shackelford and W. Alexander, *CRC Materials Science and Engineering Handbook, Third Edition*, 3rd ed. Boca Raton: CRC Press LLC, 2001.

[44] R. Baker, *Flow Measurement Handbook: Industrial Designs, Operating Principles, Performance, and Applications*. Cambridge: Cambridge University Press, 2000.

[45] G. Cao *et al.*, “Fluoride-Salt-Cooled High Temperature Reactor (FHR) Materials, Fuels and Components White Paper,” Department of Nuclear Engineering, U.C. Berkeley, 2013.

[46] L. Huddar, P. F. Peterson, R. Scarlat, and Z. Guo, “Experimental Strategy for the

Determination of Heat Transfer Coefficients in Pebble-Beds Cooled By Fluoride Salts," in *NURETH-16*, 2015, pp. 1659–1675.

[47] L. R. Huddar, "Heat Transfer in Pebble-Bed Nuclear Reactor Cores Cooled by Fluoride Salts," University of California Berkeley, 2016.

[48] "ASTM D2846/D2846M-17b Standard Specification for Chlorinated Poly(Vinyl Chloride) (CPVC) Plastic Hot- and Cold-Water Distribution Systems, ASTM International, West Conshohocken, PA, 2017." .

[49] J. Fernández-Seara, F. J. Uhía, J. Sieres, and A. Campo, "A general review of the Wilson plot method and its modifications to determine convection coefficients in heat exchange devices," *Appl. Therm. Eng.*, vol. 27, no. 17–18, pp. 2745–2757, 2007.

[50] C. E. Kalb and J. D. Seader, "Fully developed viscous—flow heat transfer in curved circular tubes with uniform wall temperature," *AIChE J.*, vol. 20, no. 2, pp. 340–346, Mar. 1974.

[51] Q. Jin, K. Qiaoling, Z. Hongwu, H. Weiguang, and L. Wenhui, "Performance of a gas cooled molten salt heat exchanger," *Appl. Therm. Eng.*, vol. 108, pp. 1429–1435, Sep. 2016.

[52] T. W. Kerlin, E. M. Katz, A. T. Chen, J. G. Thakkar, and S. I. Chang, "Dynamic Testing in Nuclear Power Plants for Model Validation," *J. Dyn. Syst. Meas. Control*, vol. 98, no. 3, p. 340, Sep. 1976.

[53] C. Poresky, "Frequency Response Testing in the CIET Facility," Berkeley, CA, 2017.

[54] R. Plettke, P. H. Vatter, D. Vipavc, M. Cojutti, and H. Hagenah, "Investigation on the Process Parameters and Process Window of Three-Roll-Push-Bending," in *Proceedings of the 36th International MATADOR Conference*, 2010, pp. 25–28.

[55] B. Engel, S. Kersten, and D. Anders, "Spline-Interpolation and Calculation of Machine Parameters for the Three-Roll-Pushbending of Spline-Contours," *steel Res. Int.*, vol. 82, no. 10, pp. 1180–1186, Oct. 2011.

[56] D. P. Kroese, T. Brereton, T. Taimre, and Z. I. Botev, "Why the Monte Carlo method is so important today," *Wiley Interdiscip. Rev. Comput. Stat.*, vol. 6, no. 6, pp. 386–392, Nov. 2014.

[57] "ASME Boiler and Pressure Vessel Code Section VIII: Rules for Construction of Pressure Vessels Division 1." American Society of Mechanical Engineers, New York, 2013.

[58] "ASME Boiler and Pressure Vessel Code, Section II, Part D: Properties (Metric)." American Society of Mechanical Engineers, New York, 2013.

[59] F. Delage, J. Carmack, C. B. Lee, T. Mizuno, M. Pelletier, and J. Somers, "Status of advanced fuel candidates for Sodium Fast Reactor within the Generation IV International Forum," *J. Nucl. Mater.*, vol. 441, no. 1–3, pp. 515–519, Oct. 2013.

[60] J. J. Sienicki, A. Moisseytsev, and L. Krajtl, "A Supercritical CO_2 Brayton Cycle Power Converter for a Sodium-Cooled Fast Reactor Small Modular Reactor," in *ASME 2015*

Nuclear Forum, 2015, p. V001T01A004.

[61] C. Andreades, A. Greenop, S. Gallagher, J. K. Choi, and P. Peterson, "Coiled Tube Air Heater Test Loop Design," in *International Conference on Nuclear Engineering, Proceedings, ICONE*, 2017.

[62] M. Li, J. Zhang, Y. Zou, Y. Fu, and Y. Yang, "DISTURBED TRANSIENT ANALYSIS WITH STABLE OPERATION MODE OF TMSR-SF1."

[63] J. Ruan, Y. Zou, M. Li, and H. Xu, "Control Scheme Research of 10MW Fluoride Salt Cooled High Temperature Experiment Reactor," in *Volume 5: Advanced and Next Generation Reactors, Fusion Technology; Codes, Standards, Conformity Assessment, Licensing, and Regulatory Issues*, 2017, p. V005T05A009.

[64] "The Preliminary Design of 1MW Molten Salt Cooled Reactor Test Facility (TMSR-SF0)," TMSR center, SINAP, 2015.